Silencing corrugated pipes

Whistling mitigation by liquid addition to vertical corrugated pipe flow

van Eckeveld, Andries

DOI
10.4233/uuid:e61212f8-e879-4b9d-8d23-670e18fa173d

Publication date
2019

Document Version
Final published version

Citation (APA)
van Eckeveld, A. (2019). *Silencing corrugated pipes: Whistling mitigation by liquid addition to vertical corrugated pipe flow*. [Dissertation (TU Delft), Delft University of Technology]. https://doi.org/10.4233/uuid:e61212f8-e879-4b9d-8d23-670e18fa173d

Important note
To cite this publication, please use the final published version (if applicable).
Please check the document version above.

SILENCING CORRUGATED PIPES
Whistling mitigation by liquid addition to vertical corrugated pipe flow

PROEFSCHRIFT

ter verkrijging van de graad van doctor
aan de Technische Universiteit Delft,
op gezag van de Rector Magnificus prof. dr. ir. T.H.J.J. van der Hagen,
voorzitter van het College voor Promoties,
in het openbaar te verdedigen op 26 september 2019

door

Andries Cornelis VAN ECKEVELD
Ingenieur Werktuigbouwkunde
Technische Universiteit Delft
geboren te Voorst, Nederland.

Dit proefschrift is goedgekeurd door de promotoren:

Prof. dr. ir. C. Poelma
Prof. dr. ir. J. Westerweel

Samenstelling promotiecommissie:

Rector Magnificus,	Voorzitter
Prof. dr. ir. C. Poelma,	Technische Universiteit Delft
Prof. dr. ir. J. Westerweel,	Technische Universiteit Delft
Dr. B.I.M. ten Bosch,	Shell Global Solutions
Onafhankelijke leden:	
Prof. dr. A.M.K.P. Taylor,	Imperial College London
Prof. dr. ir. A. Hirschberg,	Technische Universiteit Eindhoven
Prof. dr. D. Casalino,	Technische Universiteit Delft
Prof. dr. ir. B.J. Boersma,	Technische Universiteit Delft

This research is supported by Shell Global Solutions.

Cover design by Lenny ten Brinke
Printed by GildePrint - Enschede

ISBN 978-94-6323-811-3

An electronic version of this dissertation is available at
`http://repository.tudelft.nl/`.

CONTENTS

SUMMARY

Flow-induced acoustics are a well-known phenomenon, occurring in a broad variety of applications, as well as in nature. In many applications, the produced acoustics are purposeful, e.g. for communication and in musical instruments. In other circumstances, however, the sound and vibrations are a nuisance, and even harmful to human beings and the environment. Pipes with internally grooved or corrugated walls can be such a source of sound production. These pipes find broad application due to the local stiffness that is combined with larger scale flexibility of the pipes. The main industrial use of corrugated pipes is as flexible connections, transporting a gas or liquid between e.g. ships and onshore storage facilities, or between subsea bore-wells and floating production facilities.

The internal corrugations can cause vibrations when a fluid is transported through the pipe. In the case of dry gas transport, flow-induced noise can be produced, and the accompanying vibrations cause a threat to flow assurance and safe operation. The mechanism of sound production in corrugated pipes received broad attention in the scientific community, and is rather well understood. Noise mitigation, however, is not achieved easily. Active noise mitigation methods are infeasible in larger industrial applications, and retrofitting pipes with passive noise mitigation methods is generally impossible, or very costly. One auspicious method for noise mitigation is the addition of a small liquid fraction to the gaseous internal pipe flow. Although the effectiveness of this method is proven for certain applications, the mechanism behind the reduction of the acoustic output is not fully unraveled. Liquid accumulation inside the cavities of the corrugated wall, augmented acoustic damping due to the presence of liquid inside the pipe, and disturbance of the source of sound production do all play a yet unknown role.

The present work aids in understanding whistling mitigation in corrugated pipes by liquid addition. Experiments are performed in vertical corrugated pipes, both in upward an downward flow direction. Liquid is added to the pipe flows and acoustic measurements are combined with fluorescence based measurement techniques and droplet sizing to assess the effect of liquid addition. From the experimental results it is shown that liquid accumulation inside the cavities determines the reduction of acoustic amplitude in whistling conditions. Acoustic damping due to droplets present in the core of the pipe is very limited. The presence of liquid itself is not a prerequisite for the prevention of whistling, as a pipe with a corrugation geometry based on the liquid cavity filling profiles remains silent when subject to a dry gas flow. The presence of liquid rather changes the cavity geometry, resulting in whistling mitigation.

The two-phase flow behavior does, in part, determine the amount of liquid being trapped inside the cavities. Little is known about two-phase flow regimes in corrugated pipes in the very low liquid loading range. Significant differences between smooth and corrugated pipes are found in this work. In corrugated pipes the amount of entrainment, for example, is significantly higher compared to smooth pipes. A scaling law for the amount of cavity filling in a corrugated pipe is found, relating to the liquid film Reynolds number and the Weber number. This scaling law shows that the filling resulting from the gas-liquid flow in the pipe is

mainly determined by interfacial tension, and is not related to the liquid viscosity. It provides a first step towards modeling the liquid cavity filling as a function of corrugation geometry and global flow parameters.

Numerical simulations are performed to further study the specific geometrical alterations to the cavities that determine the noise reduction. A method is developed in this work combining URANS simulations with Howe's energy corollary, to estimate the acoustic source power for specific cavity geometries. This method shows promising results when compared to experiments, and provides insight into the sound producing mechanism. Although the simulations overestimate the sound power and show limitations for shallow cavities, trends that are found are very similar to the experimental results. The simulations show that sound is mainly produced in the cavity mouth region. The deeper cavity part does not contribute significantly to the sound production. Liquid ending up in the cavity mouth therefore strongly influences the acoustic output, and determines the whistling mitigation by liquid addition.

SAMENVATTING

Door stroming veroorzaakte akoestiek is een bekend fenomeen dat in een breed scala aan toepassingen en in de natuur voorkomt. In veel toepassingen wordt nuttig gebruik gemaakt van de akoestiek, bijvoorbeeld voor communicatie of in muziekinstrumenten. De veroorzaakte trillingen en het geproduceerde geluid zijn echter in veel gevallen storend, of zelfs gevaarlijk voor mensen en de omgeving. Geluidsproductie kan ook voorkomen in inwendig geribbelde buizen. Deze buizen worden veelvuldig toegepast vanwege hun globale flexibiliteit in combinatie met lokale stijfheid. De belangrijkste industriële toepassing van geribbelde buizen is voor het transport van een gas of vloeistof tussen bijvoorbeeld een schip en een opslaglocatie aan de wal, of tussen onderzeese boorputten en drijvende productie faciliteiten.

Wanneer een gas of vloeistof door de intern geribbelde buis stroomt kunnen trillingen worden veroorzaakt. Bij het transport van droog gas kan geluidsproductie voorkomen, en de daarmee gepaard gaande vibraties kunnen een bedreiging zijn voor de productie en het veilig uitvoeren van het gas transport. Het mechanisme achter deze geluidsproductie is veel bestudeerd in de wetenschappelijke literatuur, en wordt vrij goed begrepen. Het voorkomen van geluidsproductie, daarentegen, is niet eenvoudig. Actieve methoden om geluidsproductie te voorkomen zijn in grotere industriële toepassingen veelal onbruikbaar, en het uitrusten van bestaande systemen met adequate passieve methoden om geluidsproductie te voorkomen is over het algemeen erg duur of niet uitvoerbaar. Het toevoegen van een kleine vloeistoffractie aan de droge gasstroom in een geribbelde buis is een veelbelovende manier van geluidsonderdrukking. De effectiviteit van deze methode is in bepaalde omstandigheden bewezen, maar het mechanisme erachter is nog niet volledig ontrafeld. Vloeistofophoping tussen de ribben, een toename van de akoestische demping door de aanwezigheid van vloeistof en een verstoring van de geluidsbron spelen allen een tot dusver onbekende rol.

Het voorliggende werk vergroot het begrip van het onderdrukken van geluidsproductie in geribbelde buizen door vloeistoftoevoeging. Een experimentele studie is uitgevoerd aan geribbelde buizen in een verticale opstelling, met zowel opwaartse als neerwaartse stroming. Het effect van het toevoegen van een vloeistof is onderzocht door een combinatie van akoestische metingen, meettechnieken gebaseerd op visualisatie door fluorescentie en metingen van de druppelgrootte. De experimentele resultaten tonen aan dat met name vloeistofophoping tussen de ribben de vermindering in akoestische amplitude bepaald. De additionele akoestische demping door de aanwezigheid van druppels levert hieraan een zeer beperkte bijdrage. De aanwezigheid van vloeistof in de geribbelde buis is geen vereiste om geluidsproductie voorkomen; een geribbelde buis met de geometrie van een vloeistofgevulde buis produceert geen geluid in droge condities. De aanwezigheid van een vloeistof zorgt met name voor een verandering van de ribgeometrie, waardoor het ‘zingen’ van de buis wordt voorkomen.

De hoeveelheid vloeistof die tussen de ribben ophoopt wordt onder andere bepaald door het gedrag van de twee-fase stroming in de buis. Er is weinig bekend over het stromingsregime van twee-fase stromingen met zeer lage vloeistofbeladingen. Er zijn echter belangrijke verschillen tussen de stroming door een gladde en een geribbelde buis. De hoeveelheid vloei-

stof die als druppels door het centrum van de buis wordt getransporteerd is voor geribbelde buizen bijvoorbeeld veel hoger dan voor gladde buizen. Een schaling voor de opvulling van de ribben met vloeistof is gevonden, gebaseerd op het Reynolds getal van de vloeistoffilm op de buiswand en het Weber getal. Daaruit blijkt dat de opvulling van de ribben vooral wordt bepaald door de oppervlaktespanning, en niet zozeer door de viskositeit van de ingebracht vloeistof. De gevonden schalingswet is een eerste stap naar het modeleren van vloeistofvulling van de ribben van een geribbelde buis, als functie van buisgeometrie en globale stromings parameters.

De invloed van geometrische veranderingen door de aanwezigheid van vloeistof op de geluidsproductie is verder onderzocht met numerieke simulaties. Hiervoor is een methode ontwikkeld, waarin URANS simulaties worden gekoppeld aan *Howe's energy corollary*. Op deze manier kan de sterkte van de geluidsbron voor verschillende ribgeometriën worden bepaald. De resultaten van deze relatief eenvoudige methode zijn veelbelovend wanneer ze vergeleken worden met experimentele resultaten, en geven inzicht in het mechanisme achter de geluidsproductie. De sterkte van de geluidsbron wordt overschat in de simulaties, en de methode kent beperkingen voor ondiepe ribben, maar desondanks worden in experimenten gevonden trends met betrekking tot de sterkte van de geluidsbron goed benaderd. De simulaties laten zien dat geluid vooral wordt geproduceerd in de mond van de caviteiten, en dat het diepere gedeelte tussen de ribben hierbij geen grote rol speelt. De ophoping van vloeistof in de opening tussen de ribben heeft daardoor een sterk effect of de geluidsproductie, en bepaald grotendeels de sterkte van de geluidsonderdrukkende werking van de vloestoftoevoeging in geribbelde buizen.

1

INTRODUCTION

1.1 BACKGROUND

Acoustics are an indispensable part of daily life. In most circumstances, sound is useful and even enjoyable. It can, however, occur that acoustics become a nuisance, and cause hazards to people and the environment. Noise is frequently produced by a flow interacting with a structure that is present in the flow field. In a flute, for example, this is put to good use to generate audible tones (Fletcher, 1979). The flow generated by the flutist interacts with the flute geometry to generate an instability, which is the source of sound. Famous is also the Aeolian harp (see Figure 1.1a), named after the Greek god of the wind Aeolus (Rayleigh, 1915). It consists of a set of strings that are played solely by the wind. A von Kármán vortex street is generated behind the strings, resulting in a time-dependent oscillating force that makes them vibrate. When driving a car, similar flow tones can arise from an *aeroacoustic* interaction between the passing air and the car geometry. In many more industrial applications, aeroacoustic interactions also occur. *Flow-induced noise* by wind turbines and airplanes has received significant attention in recent days, and can be of considerable discomfort to citizens living nearby these sound sources. *Flow-induced vibrations* (FIVs) can also occur in internal flows. There, they arise from the interaction of the flow with side-branches (Ingard and Singhal, 1976; Bruggeman et al., 1991), single cavities (Rockwell and Naudascher, 1978; Rockwell and Schachenmann, 1982), or corrugated pipe sections (Burstyn, 1922; Cermak, 1922). The latter of these structures, corrugated pipes, are utilized in situations where a flexible, yet locally rigid connection is required to transport a fluid. The most common domestic application of such pipes is as vacuum cleaner hoses. More industrial applications exist in the gas processing industry. Corrugated pipes are used to transport liquefied natural gas (LNG) from ships to the shore, and are used as flexible risers (Figure 1.1b), connecting sub-sea gas production stations with production units like *floating production, storage and offloading vessels* (FPSOs, Bai and Bai, 2012). Flexible risers find particular applications in deep waters (up to 3 kilometers) and in harsh sea conditions, since they can withstand both vertical and horizontal movement and, due to external layers, can cope with high static pressure differences. These corrugated risers can exhibit FIVs when subjected to a dry internal gas flow. Although the riser can withstand the structural movement caused by the FIVs, the fixed connection points at both ends of the riser cannot. This eventually leads to failure of the piping system due to fatigue, compromising safe gas production and flow assurance. Sub-sea riser failure will cause hazardous situations that

(a) (b)

Figure 1.1: (a) Aeolian harp near San Francisco, USA (source: www.kalw.org). (b) Schematic structure of a flexible riser (source: www.spe.org).

have to be avoided at all costs. Since natural gas is a major driver bridging the gap from a coal and oil based economy to a more sustainable energy future based on renewable sources, the consumption of natural gas is expected to increase in the coming decade. An annual increase in gas demands with 1.6% per year is expected over the coming five years (International Energy Agency, 2018). It is of great necessity to cope with problems that arise in the natural gas production industry, and to ensure safe and reliable operation of production sites. It is, therefore, essential to avert the menace of *flow-induced vibrations* in offshore risers.

In the remainder of this chapter a brief literature overview is provided, and some aeroacoustic theory is introduced. The chapter is concluded with the research objective and outline of this thesis.

1.2 CAVITY AND CORRUGATED PIPE FLOW

Cavity flows, and acoustics that arise in these flows, appear in many different circumstances. They range from transportation noise by aircraft and trains, and flow over perforated plates, to internal flows through bellow-type pipe geometries, and side-branches. It is of particular importance to understand the whistling mechanisms in these types of flows, to be able to mitigate sound production and lower the acoustic amplitude levels that are generated. Corrugated pipe flow closely resembles flow over an infinitely wide cavity in a flat wall. The source of sound production in both geometries is the unsteady shear-layer spanning the cavities. Differences between corrugated pipes and single cavities mainly arise from the nature of the feedback loop that enhances FIVs, and from possible hydrodynamic interaction of subsequent cavities in a corrugated pipe. General findings from cavity flows, however, also apply to corrugated pipe flow, and an brief overview of both fields is given in this section.

1.2.1 CLASSIFICATION OF CAVITY FLOWS

Cavity flows are generally classified based on geometrical, flow, and acoustic considerations. The behavior of a grazing flow over a general rectangular cavity of infinite spanwise width is characterized by its length-over-depth ratio. Cavities are divided into shallow (depth-over-length ratio smaller than unity) and deep cavities (ratio larger than unity), and in open and closed cavities (see Figure 1.2).

For all cases a shear layer is formed that separates the outer flow from the low velocity flow inside the cavity. This inner cavity flow consists of one or multiple recirculation cells. In deeper cavities, two or more cells co-exist over the depth of the cavities. Open shallow cavity flow typically consists of a single dominant recirculation cell. When the cavity length-over-depth ratio increases (typically beyond 8) the shear layer reattaches at the cavity bottom, generating an upstream and downstream recirculation cell in the respective cavity corners, resulting in a so-called closed cavity flow. Shallow open cavities are primarily studied in the present work. These cavity flows are most prone to high amplitude noise production.

The dynamic behavior of a shear layer spanning a cavity mouth in this geometry largely determines the flow-induced vibrations that occur. The ratio of the cavity mouth length over the momentum thickness of the incoming boundary layer (L_c/θ) is of particular importance (Gharib and Roshko, 1987). A minimum threshold exists for vortex shedding to appear in the shear layer. This threshold depends on other flow parameters, but is in the range of $L_c/\theta \approx 80$.

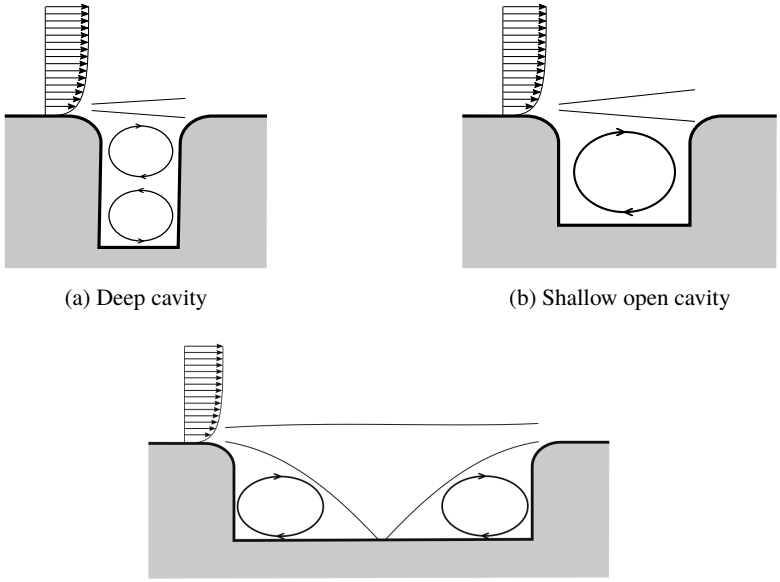

(a) Deep cavity

(b) Shallow open cavity

(c) Shallow closed cavity

Figure 1.2: Cavity geometry classification based on depth-over-length ratio

For lower values of L_c/θ, the shear layer is characterized by broadband noise. No distinct flow tones are observed, due to the absence of vortex shedding at a dominant frequency. This regime is named the *non-oscillating mode*. For larger values of L_c/θ, the shear layer becomes unstable and starts shedding discrete vortices (Michalke, 1965), which are associated with the tonal noise observed in cavity flows. This so-called *shear-layer mode* is a prerequisite for high-amplitude sound production to occur. An upper threshold of this region was also found ($L_c/\theta \approx 120$) above which the entire cavity is filled with a single recirculating flow. This *wake mode*, however, is rarely observed in experiments. The cavities studied in this work are shallow open cavities in the shear-layer mode, placed along the interior wall of a smooth pipe.

In this regime, the vorticity in the shear layers is concentrated in discrete vortices. These vortices originate from the intrinsic instability of the shear or mixing layer that separates from the upstream leading cavity edge. The velocity profile of this mixing layer exhibits an inflection point, which is a necessary condition for instability to occur (Rayleigh criterion, Rayleigh, 1880). Disturbances of a certain wavelength are amplified (Michalke, 1965). In the initial region these disturbances grow exponentially (Freymuth, 1966). Non-linear saturation occurs, where discrete Kelvin-Helmholtz type vortices are generated (Miksad, 1973). In corrugated pipes, it is the interaction of these vortices with the acoustic field inside the pipe that is the source of sound (Bruggeman et al., 1991). The whistling frequency is related to the residence time of a vortex inside the cavity mouth. A vortex is shed when the acoustic field changes sign from negative to positive streamwise direction (Nelson et al., 1983; Bruggeman et al., 1991). The whistling frequency typically scales with a characteristic Strouhal number, defined as:

$$Sr_c = \frac{f_w L}{U_c} = 0.13 + 0.40 n_h. \tag{1.1}$$

where f_w is the whistling frequency, and U_c the convection velocity of the vortices. n_h is related to the hydrodynamic mode (i.e. the number of vortices simultaneously present in the cavity mouth). For cavities with rounded edges the length scale L_c is extended with the upstream edge radius (Nakiboğlu et al., 2010). The downstream radius is less critical due to viscous spreading of the vortices over the length of the cavity mouth. The hydrodynamic interaction between subsequent cavities only occurs for closely spaced cavities. When the spacing between cavities is of the order of the cavity length, hydrodynamic interference is not expected to significantly alter the shear layer dynamics of the individual cavities (Nakiboğlu and Hirschberg, 2012). A preliminary study indicated that the effect of swirl on the acoustic output from corrugated pipes is limited, although no swirling strength measurements were performed in the experiments (Nakiboğlu et al., 2012). It is therefore anticipated that axisymmetrically corrugated pipes behave similarly to helically wound corrugated pipes with a small pitch length.

Under whistling conditions, when high amplitude tonal sound is produced in a corrugated pipe, a feedback loop exists that reinforces the sound production. Three different feedback mechanisms have been identified (Rockwell and Naudascher, 1978, 1979): *fluid-elastic* feedback, *fluid-dynamic* feedback, and *fluid-acoustic* feedback. The *fluid-elastic* feedback loop only appears when there is a structural vibration that triggers the unsteadiness in the flow. The *fluid-dynamic* resonance is of an incompressible nature and results from a directly induced velocity from the downstream vortices at the upstream cavity edge, triggering vortex shedding. In the case of a *fluid-acoustic* feedback, the vortex wall interaction feeds an acoustic resonance mode of the system, that synchronizes vortex shedding. This resonance mode can be local, inside the cavity, or global, when it concerns a resonance mode of the entire cavity system. For the acoustically compact cavities studied here (where $L_c \ll \lambda_{ac}$, with λ_{ac} the acoustic wavelength) no local resonance can occur. The feedback mechanism is then dominated by the axial standing wave in the corrugated pipe, that synchronizes vortex shedding in all cavities inside the pipe, significantly increasing the acoustic output of the pipe system. The feedback loop for this fluid-acoustic resonance is schematically depicted in Figure 1.3. Disturbances are introduced to the shear layer spanning a cavity or corrugation, and are amplified. The generated vortices feed acoustic energy to a resonance mode of the pipe system. The acoustic waves subsequently introduce new disturbances to the cavity shear layers, closing the loop. This fluid-acoustic feedback mechanism dominates the fluid-dynamic feedback that simultaneously exists in corrugated pipes (Ziada and Bühlmann, 1991).

1.2.2 MITIGATION OF WHISTLING IN CAVITY AND CORRUGATED PIPE FLOW

Noise control in cavity flows has been studied widely in literature. Both *active* and *passive* methods have been proposed. In the framework of this thesis, only passive methods are discussed. Active noise control strategies are generally not feasible in long corrugated pipes due to technical difficulties and/or high costs. Active methods typically involve pulsed jets or mass injection at the upstream edge, or make use of piezoelectric actuators or loudspeakers to reduce the noise production (see Cattafesta et al., 2003 and Rowley and Williams, 2006 for reviews of the existing methods). For passive control methods, changes are made to the cavity geometry itself in order to reduce the whistling amplitude. A porous leading edge fence or cylindrical rod in the boundary layer upstream of the cavity was shown to reduce the pressure fluctuations through a lifting of the boundary layer away from the cavity (Sarno and Franke,

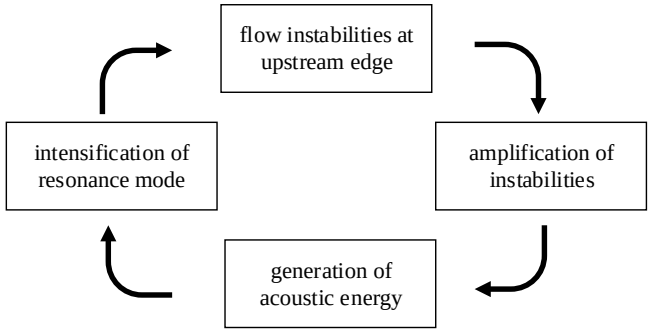

Figure 1.3: The *fluid-acoustic* feedback loop causing high-amplitude whistling in corrugated pipes.

1994; Ukeiley et al., 2004). The use of spoilers has been studied by several authors (Heller and Bliss, 1976; Bruggeman et al., 1991; Schmit and Raman, 2006), exploiting the same boundary layer lifting principle to achieve acoustic amplitude reduction. Whistling mitigation in corrugated pipes can be achieved by either reducing the acoustic source strength of the individual cavities or by increasing the acoustic damping in the pipe system. Petrie and Huntley (1980) found that a wrinkled pipe wall causes a significant reduction of the whistling amplitude. It is argued that the wrinkles act as obstructions for the flow in the separation region, thereby reducing the source strength. These authors also mentioned that increasing the upstream smooth pipe length leads to a decreased amplitude, through an effective increase of acoustic losses. This principle can be applied to manufacture non-whistling corrugated pipes that are composed of alternating smooth and corrugated sections (Elliott, 2005; Rudenko et al., 2013). The onset velocity for these *hybrid* pipes, i.e. the velocity at which whistling first appears, is significantly increased. Breaking the continuity of the corrugation in azumithal direction by cutting out a narrow band along the pipe length reduces the sound output considerably (Gharib, 1993). Since it is not reported if a gap was left open along the pipe length it remains unclear whether the acoustic resonance was broken or the source strength of the corrugations themselves was affected. Gharib (1993) also applied an active noise control method, triggered by 12 microphones placed around the circumference of the pipe, but this was not very successful in whistling mitigation. He also notes that a disturbance at the downstream edge of the corrugations is more effective in noise suppression, compared to an upstream disturbance. This is in contrast to what is found in other studies, where mainly the upstream edge geometry is important for whistling (Binnie, 1961; Bruggeman et al., 1991; Dequand et al., 2003; Nakiboğlu et al., 2010). Increasing the upstream edge rounding causes a reduction in acoustic absorption at this edge, thereby enhancing whistling. This is caused by a different interaction between the acoustic field and the shear layer vortices, and does not alter the shear layer dynamics directly. Cavities with a sharp upstream edge are therefore preferred for applications prone to FIVs. The downstream edge geometry is studied by several other authors, mainly focusing on higher subsonic or supersonic Mach number applications (Heller and Bliss, 1976; Perng and Dolling, 2001). Heller and Bliss (1976) showed that also for subsonic Mach numbers an inclined trailing edge results in strongly reduced acoustic amplitudes as a result of the ejection of vortices from the cavity mouth. Another passive noise control method is the

application of a non-constant spacing of subsequent cavities, breaking the synchrony of vortex shedding. This can lead to destructive hydrodynamic interference, limiting the acoustic amplitude (Nakiboğlu and Hirschberg, 2012). Attempts have also been made to construct corrugated risers with a flush inner surface to avoid whistling (Lyckegaard et al., 2016).

All mentioned passive sound suppression mechanisms are difficult to apply to long corrugated risers (technically and in a cost-effective manner), experiencing severe operating conditions. Furthermore, none of the methods can be applied easily to existing installations, without replacement of the entire pipe system. Belfroid et al. (2013) were the first to study liquid injection to corrugated pipe flow for whistling suppression. Very small fractions of liquid are sufficient to entirely mitigate sound production. The advantage of this method is that it can be applied to existing installations, without the need of re-installment of piping. The only adaption to the system would be a gas-liquid separator, to remove the liquid for later process stages. Three mechanisms causing whistling mitigation by liquid addition are proposed: additional acoustic damping due to the presence of liquid (either droplets in the gas flow or a film over the pipe wall); source strength reduction through filling up of the cavities with liquid; and an alteration of the shear layer dynamics by the creation of a thicker incoming boundary layer and the disruption of the shear layer by liquid fragments. Sanna et al. (2015) argue that for side-branch flows the main contribution to whistling mitigation is the additional acoustic damping, but this depends strongly on the flow regime, which can be entirely different in corrugated pipe flow. Furthermore, experiments were mainly conducted horizontally, whereas vertical flows are of great interest in several applications as well (in particular risers), and are expected to show different behavior. Liquid addition is a promising method to mitigate whistling in corrugated pipes, but the mechanisms behind this mitigation are not well understood.

1.3 AEROACOUSTIC ANALOGIES AND THE THEORY OF VORTEX SOUND

In this section, some theory on aeroacoustics is provided. This is required in later chapters of the thesis (Chapter 2 and 4). Different acoustic analogies are highlighted, with an emphasis on the theory of vortex sound. First, a more general introduction to aeroacoustics is provided. In this section, only a brief overview is provided. For more details the reader is referred to text books (for example Hirschberg and Rienstra, 2004).

1.3.1 MONOPOLES, DIPOLES AND QUADRUPOLES

Aeroacoustic sources of sound are usually divided into monopole, dipole and quadrupole sources (Russell et al., 1999). Monopole sources are associated with a fluctuating mass inflow and are regularly the most effective sound sources, producing the highest sound pressure levels. An acoustic monopole radiates unidirectional sound. A dipole source can for example originate from turbulent eddies deforming near surfaces. It can be modeled by two equal monopole sound sources in close proximity and opposite in phase. Four monopole sound sources model an acoustic quadrupole. Quadrupole sources are related to for example turbulent eddies in close proximity, deforming each other. Sound generation by free turbulence is of quadrupole nature.

For low Mach number flows, the ratio of the contributions of the quadrupole over the dipole sources of sound scales with the Mach number squared (Curle, 1955). The quadrupole contri-

butions to the sound production are therefore negligible compared to the dipole contributions in the low-subsonic Mach number applications studied in this thesis. Monopole sound sources are related to the movement of solid boundaries in the flow, which are negligible in case of the corrugated pipe flow. The acoustic sources in corrugated pipes are, therefore, considered to be of a dipole nature (Elliott, 2005; Popescu and Johansen, 2008). As the motion within the cavity may be regarded incompressible, the net volume flux through the cavity mouth vanishes, and the sound source behaves as a dipole rather than a monopole source (Howe, 1997).

1.3.2 AEROACOUSTIC ANALOGIES

Aeroacoustics is the field within acoustics that deals with noise originating from turbulent fluid flows or from fluid-structure interactions. The sound in these situations is typically a minute fraction of the total energy in the system. It is particularly difficult to predict the sound production. Especially at low Mach number, the typical time scales of the hydrodynamics and acoustics are far apart, requiring expensive numerical methods for compressible flows to solve both simultaneously. Aeroacoustic analogies have been developed to describe the sound generated by fluid flow. This approach treats the acoustic and hydrodynamic parts of the flow separately.

This field was pioneered by James Lighthill in 1952, with the derivation of his aeroacoustic analogy (Lighthill, 1952). All analogies are derived from the compressible Navier-Stokes equations, which are rearranged into different forms of the inhomogeneous wave equation:

$$\left(\frac{1}{c_0^2}\frac{\partial^2}{\partial t^2} - \nabla^2\right) p' = \boldsymbol{F}(\boldsymbol{x}, t), \tag{1.2}$$

where p' is the acoustic variable (the fluctuating acoustic pressure), c_0 the speed of sound, and **F** represents an external forcing. The most important analogies are briefly described here, with specific emphasis on Howe's theory of vortex sound.

Lighthill's analogy is derived for a small source region in a quiescent unbound fluid. The density perturbation (ρ') is used as the acoustic variable. It shows that in this case sound production can only originate from quadrupole sources, as there is no net volume injection or external force field. Ffowcs Williams and Hawkings (1969) generalized Lighthill's equation to deal with the presence of solid boundaries, in arbitrary motion. The perturbation density is maintained as acoustic variable. For stationary surfaces the Ffowcs Williams-Hawkings analogy reduces to Curle's formulation (Curle, 1955). Both analogies show the importance of dipole sound sources when solid boundaries are present. For low Mach number flows, the dipole term dominates over the quadrupole term. Powell (1964) derived a *theory of vortex sound*, similar to Lighthill's equation, but highlighting the role of vorticity in the sound production process. Howe (2003) later derived an energy corollary based on Powell's theory that has a more limited validity. It does, however, provide valuable insight in the energy transfer between the unsteady potential (acoustic) flow and a vortical flow. Only the derivations of Powell's and Howe's formulations are shown here. They are used since they provide intuitive physical understanding of sound production by vortical flows, as observed in corrugated pipes. Furthermore, the source region over which the vorticity is non-vanishing is usually smaller compared to the source region in Lighthill's formulation, reducing the required computational power.

1.3.2.1 *Theory of vortex sound*

Powell derived his aeroacoustic analogy to underline the interplay between the acoustic field and the vorticity in the flow. In order to arrive at Powell's theory of vortex sound (Powell, 1964), we start from the momentum equations. Rewriting them using the Lamb vector $\left(\boldsymbol{\omega} \times \boldsymbol{u} = \boldsymbol{u} \cdot \nabla \boldsymbol{u} - 1/2 \nabla |\boldsymbol{u}|^2\right)$ for incompressible flows at high Reynolds number (viscous forces can be neglected), yields:

$$\rho \frac{\partial \boldsymbol{u}}{\partial t} + \rho \nabla \left(\frac{1}{2} |\boldsymbol{u}|^2 \right) + \rho (\boldsymbol{\omega} \times \boldsymbol{u}) + \nabla p = 0. \tag{1.3}$$

In this formulation, $\boldsymbol{\omega}$ is the vorticity, $\mathbf{u}$ the flow velocity vector and p the pressure. Using density and pressure perturbations ($p' = p - p_0$ and $\rho' = \rho - \rho_0$) it holds that:

$$\frac{\partial^2 \rho}{\partial t^2} - \nabla^2 p = \frac{\partial^2 \rho'}{\partial t^2} - \nabla^2 p'. \tag{1.4}$$

From the definition of the speed of sound for homentropic conditions it follows that $p' = c_0^2 \rho'$. Combining this with Equation 1.4 gives:

$$\frac{\partial^2 \rho}{\partial t^2} - \nabla^2 p = \frac{1}{c_0^2} \frac{\partial^2 p'}{\partial t^2} - \nabla^2 p'. \tag{1.5}$$

A combination of the continuity equation and the momentum equations (Equation 1.3) with Equation 1.5 gives Powell's vortex sound theory:

$$\frac{1}{c_0^2} \frac{\partial^2 p'}{\partial t^2} - \nabla^2 p' = \nabla \cdot \left(\rho (\boldsymbol{\omega} \times \boldsymbol{u}) + \nabla \left(\frac{1}{2} \rho |\boldsymbol{u}|^2 \right) - \left(\boldsymbol{u} \frac{\partial \rho}{\partial t} \right) - \left(\frac{1}{2} |\boldsymbol{u}|^2 \nabla \rho \right) \right). \tag{1.6}$$

Powell showed that the right hand side terms between parentheses scale as $1 : 1 : SrMa^2 : Ma^2$. For low Mach number applications, the third and fourth right hand side terms can be neglected. For a compact source region (with respect to the acoustic wavelength) the second right hand side term can also be neglected. If the total or stagnation enthalpy (defined in the following) is used as acoustic variable, this term can be included in the left hand side of Equation 1.6. Only the first right hand side term remains $(\nabla \cdot \rho(\boldsymbol{\omega} \times \boldsymbol{u}))$, which is related to a dipole sound source. A Green's function can be used to obtain the far field sound resulting from the acoustic energy generated in the source region.

Howe's energy corollary builds on similar principles (Howe, 1980, 2003). The total enthalpy h_t is used as the acoustic variable, which is also possible for Powell's theory of vortex sound. It is defined as:

$$h_t = \int \frac{dp}{\rho} + \frac{1}{2} |\boldsymbol{u}|^2. \tag{1.7}$$

Howe exploits a Helmholtz decomposition of the flow field to define the acoustic velocity:

$$\boldsymbol{u} = \nabla \phi + \nabla \times \boldsymbol{\psi}, \tag{1.8}$$

where ϕ is a scalar potential, and ψ a stream function. The acoustic flow field $\boldsymbol{u}'_{ac}$ is then related to the gradient of the unsteady component of the potential flow ($\nabla\phi'$). Crocco's momentum equation, valid for homentropic flow without external forcing is used as a starting point:

$$\frac{\partial \boldsymbol{u}}{\partial t} + \nabla h_t = -(\boldsymbol{\omega} \times \boldsymbol{u}). \tag{1.9}$$

In the case of a potential flow ($\boldsymbol{\omega} = 0$), an acoustic flow superposed on a steady potential flow remains, illustrating that the vortical flow acts as an external forcing to the acoustic velocity. This vortical flow is the source of sound, related to a Coriolis force:

$$f_c = -\rho(\boldsymbol{\omega} \times \boldsymbol{u}). \tag{1.10}$$

The time averaged power, transferred from the vortical field to the acoustic field is then related to the time-averaged work done by this Coriolis force on the acoustic field, integrated over a region where the vorticity is non-vanishing:

$$\langle P_{source} \rangle = -\rho_0 \left\langle \int_V (\boldsymbol{\omega} \times \boldsymbol{u}) \cdot \boldsymbol{u}'_{ac} dV \right\rangle. \tag{1.11}$$

This is the original formulation by Howe (1980), which also stresses that vortices are associated with a sound source of dipolar nature, as was found by Curle (1955). An acoustic velocity is required in order to transfer energy to the acoustic field, which corresponds with the findings of Gharib (1993) that corrugations close to acoustic pressure nodes, where the acoustic velocity is large, contribute most to the sound production inside a pipe.

1.4 OBJECTIVES AND SCOPE OF THE RESEARCH

For safety and flow assurance it is important to understand flow-induced noise in corrugated pipes and to come up with mitigation measures that can retrofitted to existing systems. Liquid addition to corrugated pipes has a large potential to achieve whistling mitigation. The mechanisms behind this method are, however, rather complex and not well understood, complicating the practical applications. In this work, we aim to gain insight in the relevant mechanisms behind the reduction of the whistling amplitude, which will aid in prediction of the amount of liquid addition required to achieve full whistling mitigation. Because of practical considerations of performing experimental research, the current work is restricted to atmospheric conditions. General corrugation geometries are studied where whistling frequencies are below the cut-off frequency of the pipe system (only axial resonance modes exist; see Rienstra, 2015). Furthermore, only vertical (both upward and downward) pipe flow is considered, since this is the most relevant case in industrial applications.

1.5 OUTLINE OF THE THESIS

The thesis is organized as follows. In Chapter 2 the effect of liquid addition to corrugated pipe flow is considered. This is achieved combining acoustic measurements with flow visualization techniques. Whistling mitigation as a function of liquid addition is studied and different

whistling mitigation mechanisms are assessed. The results for upward and downward vertical corrugated pipe flow are compared for a single corrugation geometry. In Chapter 3 the two-phase flow behavior in smooth and corrugated pipes is studied. This is of utmost importance for whistling in corrugated pipes, to be able to relate whistling mitigation with global flow parameters. Liquid can occur as droplets in the gas flow, or as a film attached to the pipe wall. The droplet concentration and size, as well as the behavior of the liquid film has a large influence on the acoustics of the corrugated pipe. Two different corrugation geometries are used in this chapter. To evaluate the effect of the surface tension and viscosity of the added liquid, water and mono-ethylene glycol are added to the dry gas flow, and differences in flow behavior for smooth and corrugated pipes are studied. Chapter 4 provides a more detailed study on whistling in corrugated pipes, both in single phase and two-phase conditions. Several corrugation geometries are compared, and acoustic measurements are again combined with flow visualization. In this chapter, the initial work of Chapter 2 is extended to multiple geometries and with water and mono-ethylene glycol as injected liquids. The relevance of acoustic damping by droplets present in the gas flow is evaluated, and specific alterations to the corrugation geometries caused by the presence of liquid are studied. A numerical method is used to predict the acoustic source strength of these altered geometries, and to provide a tool to better understand whistling in corrugated pipes. The work is concluded in Chapter 5, where a summary of the conclusions presented in this thesis is given, as well as perspectives for future research.

2

MITIGATION OF WHISTLING IN VERTICAL CORRUGATED PIPES BY LIQUID ADDITION

When a corrugated pipe is subject to a dry gas flow, high amplitude sound can be produced (so-called 'whistling'). It was shown previously that liquid addition to corrugated pipe flow has the ability to reduce the sound production. Small amounts of liquid are sufficient to mitigate whistling entirely. One of the mitigation mechanisms, cavity filling, is studied experimentally. Acoustic measurements are combined with a planar laser-induced fluorescence (PLIF) technique to measure the liquid accumulation in the cavities of a corrugated pipe. Using this technique, it is shown that the amount of filling of the cavities with liquid increases with an increasing liquid injection rate and with a reducing gas flow rate. The reduction in whistling amplitude caused by the liquid injection is closely related to the cavity filling. This indicates that the geometric alteration of the pipe wall, caused by the accumulation of liquid inside the cavities, is an important factor in the reduction of the whistling amplitude.

This chapter is based on: A.C. van Eckeveld, J. Westerweel, C. Poelma, "Mitigation of whistling in vertical corrugated pipes by liquid addition", *Experiments in Fluids*, 58(9): 107, 2017.

2.1 INTRODUCTION

Corrugated pipes are used in many applications throughout industry. These pipes have the advantage of flexibility over the pipe length, while still being rigid locally. Typical applications are connections between hard to reach locations and connections that have to allow for movement of the attachment points. When these pipes are subject to an internal gas flow, so-called *flow-induced vibrations* (FIVs) can occur, caused by an interaction between an acoustic pipe resonance and the unsteady shear layers spanning the corrugations. Under certain conditions these FIVs result in the production of high amplitude tonal noise (also known as whistling). This is not only inconvenient, but can lead to damage of equipment, failure of piping systems, and hazardous situations. This chapter is focused on whistling attenuation by liquid addition to vertical corrugated pipe flow and the identification of the mechanisms behind this attenuation. For this purpose a new approach is developed to identify the liquid accumulation within the cavities of a corrugated pipe based on *planar laser-induced fluorescence* (PLIF) measurements. These measurements are combined with acoustic measurements to identify the sound production from the corrugated pipes.

Burstyn (1922) and Cermak (1922) were the first to study the sound production from single-phase corrugated pipe flow. Since then, many studies have been devoted to the phenomenon behind the whistling behavior, which are summarized in a review paper on corrugated pipe flow by Rajavel and Prasad (2013). Whistling in corrugated pipes originates from a fluid-acoustic feedback. The free shear layers spanning the cavities in this kind of flows are intrinsically unstable and can act as a source of sound. Under certain conditions, vortex shedding can occur. These discrete vortices exert an unsteady force on the walls, causing a reaction force, which is associated with the sound generation (Curle, 1955). This sound source is of a dipole nature due to the vortex-wall interactions (Howe, 2003), and feeds an axial acoustic mode of the pipe when the shedding frequency is below the cut-off frequency for non-axial pipe modes. The acoustic perturbation caused by this acoustic resonance is a source of instability in the shear layers over the corrugations, triggering vortex shedding and closing the feedback loop.

The onset velocity of whistling was initially thought to be related to a minimum required level of turbulence in the flow (Crawford, 1974; Cadwell, 1994). Later it was proposed, based on an energy balance model, that an increase of acoustic losses relative to the source strength is a more probable cause for the absence of whistling at low flow velocities (Nakiboğlu et al., 2012b). After onset, a typical discontinuous linear (or "step-wise") increase in whistling frequency is observed, caused by the finite number of possible axial wave modes. The acoustic plane waves, with a frequency below the cut-off frequency of the pipe, are determined by: $f_n = nc/2L_p$, with c the speed of sound, L_p the pipe length, and $n = 1, 2, 3, \ldots$. Binnie (1961) noticed that the speed of sound in corrugated pipes is slightly different from the speed of sound in free space, and later Elliott (2005) proposed an effective speed of sound in corrugated pipes:

$$c_{eff} = \frac{c_0}{\sqrt{1 + V_c/(A_p P_c)}}, \tag{2.1}$$

where c_0 is the speed of sound in free space, V_c is the cavity volume, A_p the inner cross-sectional area of the pipe, and P_c the pitch length (as defined in Figure 2.1). When the flow rate is increased some of the pipe modes are excited, while others remain silent. This is associated

with the acoustic boundary conditions, as shown by Goyder (2010). The linear increase in whistling frequency with flow speed U is associated with a whistling Strouhal number ($Sr = fL/U$). For corrugated pipes several length scales have been used for the definition of the Strouhal number. Nakiboğlu et al. (2010) showed that $L = L_c + r_{ed}$ (see Figure 2.1) gives the best collapse of whistling Strouhal numbers for different corrugated pipe geometries.

The effect of corrugation geometry and pitch length was first evaluated by Binnie (1961). He observed clear changes in whistling amplitude upon changing the radius of the rib edges. This was later confirmed by Bruggeman et al. (1991) for side-branch configurations and by Nakiboğlu et al. (2010) for corrugated pipes. Rounding the upstream edge of the cavities leads to an increase in whistling amplitude, due to reduced acoustic absorption near this edge. The authors also assessed at the effect of cavity depth on the acoustic source strength (Nakiboğlu et al., 2012a). They demonstrated that above a certain length-over-depth ratio ($L_c/H_c \geq 2$) the source strength significantly decreases when further decreasing the cavity depth. Below this threshold a very limited effect was noted.

2.1.1 MITIGATION OF WHISTLING

Several studies were dedicated to mitigation or attenuation of whistling in corrugated pipes. Petrie and Huntley (1980) were among the first to look into whistling mitigation. Their study focused on whistling in vacuum cleaner hoses. Several ways to reduce sound production from these corrugated pipes were proposed. They observed that obstructions in the flow separation region (for example by using a corrugated pipe with a wrinkled instead of a smooth wall) significantly reduce the whistling amplitude. They also found that the incoming boundary layer thickness is of major importance to the occurence of whistling, since it determines whether or not the shear layers spanning the corrugations become unstable. Attempts that made use of active noise control with small speakers at a single corrugation did not prove to be very succesful (Gharib, 1993) and are not feasible in many industrial applications. More recently, Rudenko et al. (2013) came up with a semi-empirical model for corrugated pipes with smooth segments. With the acoustic amplitude obtained from two-dimensional axisymmetric URANS simulations, the model determines the smooth pipe length required to damp the acoustic waves generated by the corrugated segment, essentially by increasing the onset velocity to higher values, compared to a fully corrugated pipe.

Addition of liquid to the gas flow through a corrugated pipe is shown to have the potential to mitigate whistling entirely (see Belfroid et al., 2013; Golliard et al., 2013a; Belfroid et al., 2014). These studies focused on sound mitigation in horizontal pipes, with some exper-

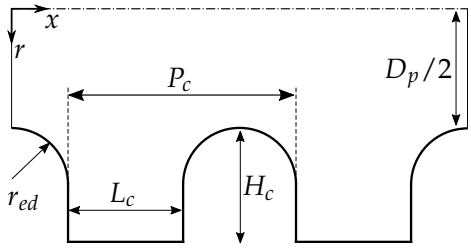

Figure 2.1: Schematic of the corrugation geometry and definition of frame of reference

iments in a vertical orientation, and a field case study. Small liquid fractions were sufficient to prevent whistling in most cases. The authors proposed several whistling mitigation mechanisms: filling of the cavities with liquid; additional acoustic damping; and a reduction of the acoustic source strength due to boundary layer thickening. As a follow-up, the authors conducted experiments in side-branch configurations with liquid addition (Sanna et al., 2015). They found that whistling mitigation in that case is mainly caused by the additional acoustic damping caused by the presence of water. Therefore the flow regime plays an important role, especially for the horizontal pipes they studied. The relevance of the different mechanisms behind the mitigation of whistling in corrugated pipes is still unclear.

2.1.2 DIMENSIONLESS PARAMETERS

Several dimensionless parameters are used in the current work and their definition is given in this section. Figure 2.1 provides an overview of the geometric parameters concerning the corrugated pipe. The displayed geometry is a simplified version of commonly used corrugated pipes.

For single phase whistling, two parameters are of particular importance; the Mach number and the Reynolds number. Normalization of the bulk velocity (U_b) with the speed of sound (c_0) gives the Mach number:

$$Ma = U_b / c_0. \tag{2.2}$$

The flow in this work is considered to be incompressible ($Ma^2 \ll 1$). The whistling frequency f_w is normalized using the Strouhal number, where the length scale proposed by Nakiboğlu et al. (2010) is applied:

$$Sr = f_w(L_c + r_{ed})/U_b. \tag{2.3}$$

Also the Reynolds number is important, which compares inertial and viscous forces in the gaseous bulk flow: Re$= \rho_g U_b D_p / \mu_g$, with ρ_g and μ_g being the mass density and the dynamic viscosity of the gas phase, respectively.

For the two-phase flow through corrugated pipes, a couple of additional dimensionless numbers are relevant. The Weber number compares the inertial forces (IN) and the surface tension (SF): $We = IN/SF$. The Bond number is used to compare the surface tension and gravitational forces (GR): $Bo = GR/SF$. For the specific situation studied in this work, these forces are defined as:

$$IN = \rho_g U_j^2 L_j L_r, \qquad GR = \Delta\rho g H_c L_c L_r \alpha, \qquad SF = \sigma L_r. \tag{2.4}$$

α is the fraction of the cavity volume occupied by liquid. The accompanying length scales and velocities are estimated based on experimental work on cavities in a flat-plate (Koschatzky et al., 2011) and are defined as

$$L_j = L_c^*/4, \qquad L_r = \pi D_p, \qquad U_j = U_b/4. \tag{2.5}$$

The jet-like flow directed into the cavity along the downstream cavity wall is the main source of inertial forces exerted at the liquid inside the cavity. The average velocity in this jet is

Table 2.1: Range of dimensionless parameters attained in the present experiments

Quantity	Range
Re_g	$10^4 - 10^5$
We	$10^0 - 10^1$
Bo	$10^0 - 10^1$

taken as 25% of the bulk velocity, which is a typical value found for flat plate cavities. The streamwise length scale for this jet is taken as one quarter of the free cavity length L_c^*, which is defined in Section 2.4.2. The curvature of the surface, used in the definition of the surface tension forces, is the cavity length. Table 2.1 gives the range for the Bond and Weber numbers attained in the current experiments.

2.1.3 OBJECTIVE AND OUTLINE

This chapter focuses on the effect of liquid addition to whistling in upward gas flow through vertical corrugated pipes. As stated in the previous section, the relevance of the different mechanisms behind whistling mitigation by liquid addition remains a subject of further study. This work intends to contribute to answering this question by investigating specifically the influence of filling of the corrugations to whistling mitigation. For that purpose, an experimental set-up is developed aimed at measuring the liquid accumulation within the corrugations, while simultaneously measuring the acoustic output of the corrugated pipe. In Section 2.2 an overview of the experimental setup is provided, followed by the measurement procedure and data processing in Section 2.3. The results are presented in Section 2.4, followed by a discussion in Section 2.5. Section 2.6 provides conclusions from this work and an outlook to future work.

2.2 EXPERIMENTAL SET-UP

The measurements are carried out in a dedicated experimental set-up with a vertical test section. A schematic representation of the set-up is depicted in Figure 2.2. Air flow through the pipe is provided by a blower (Esam Mediojet 2V, A in the figure). A long-radius ASME flow nozzle, having a zero β ratio (Leutheusser, 1964), is used for flow rate measurements. Comparison of the flow rate obtained using this nozzle with pitot tube measurements yields a maximum error in the volumetric flow rate smaller than 4% for all cases. The blower is connected to an expansion vessel, with a diameter of 0.5 *m* and a length of 1 *m* (B in Figure 2.2). The vessel is covered on the inside with a 10-*cm* thick layer of sound absorbing foam to reduce acoustic resonances in the interior of the vessel. The expansion vessel both serves as a damper for noise generated upstream by the blower, and it provides a high acoustic reflection coefficient boundary condition upstream of the corrugated pipe. Together with the high acoustic reflection at the open outflow of the pipe, it enhances whistling by strengthening the acoustic standing wave inside the corrugated pipe. The acoustic measurement section (C in Figure 2.2) consists of four microphones (PCB 106B) flush mounted in the pipe wall. The positions of the microphones are chosen to ensure a truthful reconstruction of the acoustic waves

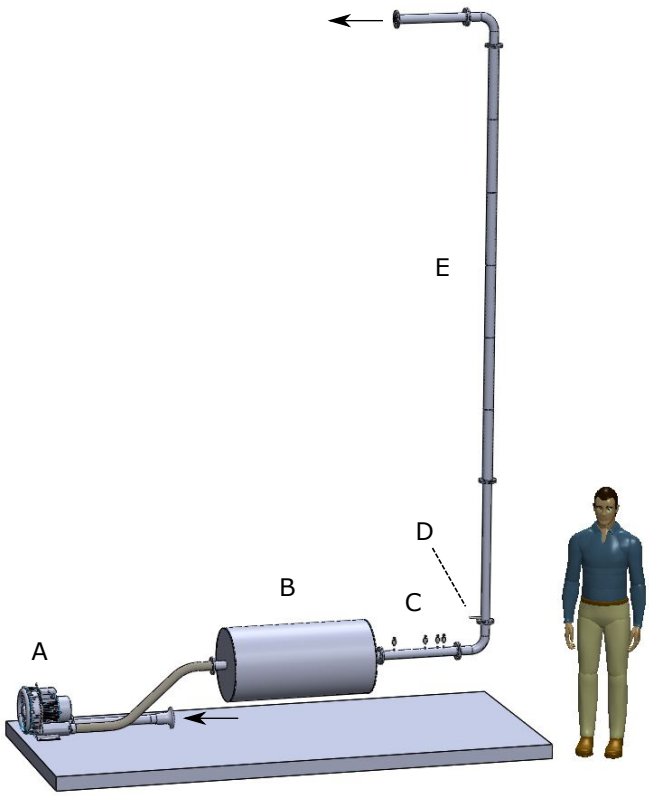

Figure 2.2: Schematic representation of the experimental set-up, with A = blower, B = expansion vessel, C = acoustic measurement section, D = liquid injection point and E = corrugated section. A more detailed description is found in the text.

in the frequency range of interest (0 - 3.5 *kHz*). Following the work by Jang and Ih (1998), the second, third and fourth microphones are placed at distances to the first microphone of 0.225 *m*, 0.315 *m* and 0.360 *m*, respectively. The microphones are connected to a data acquisition card (NI PCI-4472). Dynamic pressure signals obtained from the acoustic measurement section are used to reconstruct the traveling waves in the main pipe, from which the standing acoustic wave is obtained (as explained in Section 2.3.1). A pressure tap is placed just before the liquid injection point (D), to make sure that the presence of liquid does not interfere with the pressure measurements. The static pressure at this point is used to correct the flow rate for changes in density. Liquid is injected into the pipe between the pressure tap and the corrugated pipe section, using spray nozzles (Bete PJ8, PJ10, PJ15 and PJ24) connected to a rotary vane pump (Fluid-O-Tech PA111). The nozzles produce a dispersed spray of droplets with a nominal diameter less than 150 μm. The liquid flow rate is measured using a Coriolis mass flow meter (Bronkhorst M14 CORI-FLOW)[1]. For flow development purposes a 1-m long smooth pipe section ($L/D_p = 20$) is placed behind the liquid injection point, followed by the corrugated pipe section (E). The flow loop is terminated with an open outflow, blowing into a large room (5x10x4 m^3), without any acoustical treatment of the walls. Temperature measurements are performed at the outlet using a Pt100 temperature probe located at the pipe center-line. The temperature measurements are used to correct the mass density of the gas and the speed of sound (assuming an ideal gas: $c_0 = \sqrt{\gamma R T_{air}/M_{air}}$, where γ is the ratio of specific heats, R the ideal gas constant, T_{air} the temperature inside the pipe and M_{air} the molar mass of air). The speed of sound has not been corrected for the presence of droplets in the gas phase. At the very low volume fractions of liquid in suspension reported in this study, the effect on the speed of sound is rather limited (Kieffer, 1977).

The smooth piping is made of steel, with an inner diameter (D_p) of 49.25 *mm*, and a wall thickness of 5 *mm*. This high wall thickness is chosen to prevent structural vibrations that might influence the measurements. The corrugated section is machined from PVC and has a minimum wall thickness of 10 *mm*. One particular corrugation geometry is used in this study, schematically depicted in Figure 2.1. The depth (H_c) and length (L_c) of the corrugations is 4 *mm*, with rounded upstream and downstream edges, both having a radius (r_{ed}) of 2 mm. The edges were rounded because this was shown to enhance the whistling behavior of corrugated pipes (Nakiboğlu et al., 2010). The pitch length (P_c) is 8 *mm*, resulting in a zero plateau length between the ribs which reduces the onset velocity for whistling of the corrugated pipe. These dimensions are chosen to obtain whistling over a large Mach number range. The length of the corrugated pipe could be varied, but was maintained constant during the reported measurements, with a length of 3 *m* ($L_p/D_p \approx 61$), containing 375 corrugations. Increasing the corrugated pipe length further is not expected to add to the whistling amplitude (Nakiboğlu et al., 2011).

For optical access a transparent corrugated section was placed just before the end of the corrugated pipe, at $49 \leq L/D \leq 53$ from the corrugated pipe entrance. Although an improved refractive index matching could be achieved using a different material (e.g. FEP), the section is made from PMMA, for practical reasons. A *planar laser-induced fluorescence* (PLIF) tech-

1 An estimation of the evaporation rate is carried out based on the Sherwood number (Froessling, 1938), assuming all liquid is present as 100-μm size droplets being transported with the gas velocity. The evaporation will be in the order of 5% in the range of interest. The actual evaporation rate is expected to be lower, since the evaporation from liquid present in the film at the pipe wall is considerably lower compared to droplet evaporation. The liquid flow rate is therefore not corrected for evaporation.

nique is used to measure the liquid accumulation in the corrugations. The experimental layout of the PLIF measurement set-up is shown in Figure 2.3. The transparent section is contained in an optical box made from PMMA to reduce image distortion due to refraction of light at the curved outer pipe wall. The optical box is filled with water. To reduce the effect of total internal reflection at the liquid-gas interface inside the pipe and the effect of refraction at the water-PMMA interface at the pipe wall, the viewing angle of the camera is 25° with respect to the laser sheet. With a steady and perfectly axisymmetric gas-liquid interface within the corrugations, this yields a viewing angle well below the critical angle for air-water (= 48.6°). A digital camera (LaVision Imager Intense, 1*MP* sensor) was used, equipped with a 105 *mm* focal length (Nikkor) objective and a red filter (B+W 62 041) to capture only the fluorescent light from the fluorescent dye (rhodamine WT) that is added to the injected water. The dye concentration is optimized for the required light intensity of the emitted fluorescent light, resulting in a concentration 125 $\mu g/L$ water. Furthermore, the optical box was filled with a rhodamine solution of approximately 50 $\mu g/L$, and the fluorescent light emitted from this region is used to correct for non-uniformity in the laser sheet.

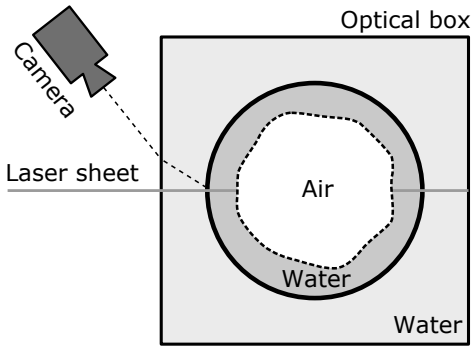

Figure 2.3: Schematic of the PLIF set-up used in the visualization measurements, as seen from the top. The water in the interior of the pipe is dyed with 125 $\mu g/L$ rhodamine, water in the optical box with 50 $\mu g/L$.

2.3 MEASUREMENT PROCEDURE AND DATA PROCESSING

2.3.1 ACOUSTIC MEASUREMENTS

Acoustic pressure measurements are acquired at a sampling frequency of 40 *kHz*, which is well above the cut-off frequency of the pipe to ensure that aliasing effects would not interfere with the sampling rate. Time series are collected with a duration of one second. For each set of parameters the measurements are repeated four times and checked for consistency. The dynamic pressure signals are acquired simultaneously with static pressure, temperature and flow rate measurements to compute the actual flow rate through the corrugated section.

The acoustic waves in the pipe are reconstructed using the multiple microphone method (Jang and Ih, 1998). Since the whistling frequencies are always below the cut-off frequency

of the pipe, the acoustic field is composed of plane waves traveling back and forth through the pipe. The acoustic field can then be described by

$$P(x) = P^+ \exp(-ik^+ x) + P^- \exp(ik^- x), \tag{2.6}$$

where P is the complex-valued amplitude of the dynamic pressure ($p(x,t) = P(x)e^{i\omega t}$) at position x, P^+ and P^- are the amplitudes of the upstream and downstream traveling acoustic waves, and k^+ and k^- the respective complex wavenumbers. Measuring the dynamic pressure at n positions along the pipe results in the following overdetermined linear system of equations that can be solved for P^+ and P^- using a least-squares approach:

$$\begin{bmatrix} \exp(-ik^+x_1) & \exp(ik^-x_1) \\ \exp(-ik^+x_2) & \exp(ik^-x_2) \\ \vdots & \vdots \\ \exp(-ik^+x_n) & \exp(ik^-x_n) \end{bmatrix} \begin{pmatrix} P^+ \\ P^- \end{pmatrix} = \begin{pmatrix} P_{x_1} \\ P_{x_2} \\ \vdots \\ P_{x_n} \end{pmatrix}. \tag{2.7}$$

Neglecting the acoustic attenuation by turbulent fluctuations in the bulk of the flow (since the ratio of acoustic boundary layer thickness to thickness of the viscous sublayer of the turbulent mean flow is in the order of one: $\delta_{ac}^+ = \delta_{ac}/\delta_l \approx 1$; see Weng 2015), the complex wavenumbers are obtained using the model proposed by Dokumaci (1995). Assuming a uniform mean velocity profile in the pipe, he derived the following expression for the wavenumber, valid for large shear numbers ($Sh = 0.5D_p\sqrt{\omega/\nu} \gg 1$):

$$k^\pm = k_0 \frac{\pm\Gamma_0}{1 \pm \Gamma_0 Ma}. \tag{2.8}$$

In this equation, k_0 is the wavenumber in free space ($k_0 = \omega/c_0$) and Γ_0 the dimensionless wavenumber for sound propagation through a quiescent fluid inside a pipe, taking into account the viscothermal damping only. At high shear numbers, Γ_0 can be approximated by (Ronneberger and Ahrens, 1977):

$$\Gamma_0 = 1 + \frac{1-i}{Sh\sqrt{2}}\left(1 + \frac{\gamma-1}{\sqrt{Pr}}\right) - \frac{i}{Sh^2}\left(1 + \frac{\gamma-1}{\sqrt{Pr}} - \gamma\frac{\gamma-1}{2Pr}\right), \tag{2.9}$$

where Pr is the Prandtl number, and γ the ratio of specific heats.

Considering a high acoustic reflection coefficient (R) at both pipe ends, a standing wave is present in the pipe, with a maximum amplitude of $P_{st} = P^+ + P^-$. The reflection coefficients at both pipe ends are determined in a dedicated set-up, using the multiple microphone method (similar to Peerlings 2015). The reflection coefficient is defined as the ratio of the incoming and reflected wave amplitude at the pipe end: $R_{x_0} = P_{x_0}^-/P_{x_0}^+$. It is found that the reflection coefficient for the upstream and downstream acoustic termination is not equal to one. Especially for higher values of kr_p (where the wavenumber k is non-dimensionalized with the pipe radius: $r_p = \frac{1}{2}D_p$) it tends to deviate (Figure 2.4a). This causes the acoustic waves traveling towards the expansion vessel to be significantly higher in amplitude compared to the reflected waves traveling in the opposite direction (Figure 2.4b). The main region of interest for the present study is located towards $kr_p = 1$, where $|R|$ attains values below 0.7.

The whistling amplitude of the corrugated pipe will be affected by this acoustic boundary condition. A standing wave is however still observed in the range of interest, and the amplitude of this standing wave is used as a representation of the strength of the acoustic field generated in the corrugated pipe (A^{st}_{max}). A typical frequency spectrum, obtained using the described method, is depicted in Figure 2.5.

Whistling is identified using the whistling criterium proposed by Nakiboğlu et al. (2010). For every data set, the frequency with the highest amplitude of whistling (f_w) is identified, and the energy (E_w) contained within $\pm$ 1 Hz of that frequency is compared to the energy (E_{sig}) in the entire discrete Fourier transform (DFT) of the time series. This bandwidth is used because it contains most of the energy of the peak in the frequency spectrum (Figure 2.5). The ratio between the energy contained in the peak and the energy of the entire signal is used as a criterium for whistling to occur, i.e. whistling occurs when $W > 0.1$, with:

$$W = \frac{E_w}{E_{sig}}. \tag{2.10}$$

Subsequently, a sine wave is fitted to the raw signal with the same whistling frequency (f_w). The whistling amplitude (A_w) is obtained by adapting the amplitude of the sine wave so that its energy content matches E_w. To evaluate this procedure, the repeatability of the whistling amplitude and frequency is tested and found to be within one percent, when keeping the flow settings constant.

2.3.2 PLIF MEASUREMENTS

PLIF measurements are used to quantify the amount of liquid accumulating inside the corrugations. Images are recorded at a frame rate of 2 Hz, with each series containing 200 images and repeated twice for every measurement point within the parameter space of interest. First, the required gas flow rate is set, and liquid injection is switched on, starting from the highest liquid flow rate achievable with the nozzle in place. After ensuring full wetting of the interior of the pipe, the liquid flow rate is adjusted to the desired value. Data acquisition is started when the acoustic output and the average filling has reached an equilibrium state. During all PLIF measurements, two series of acoustic measurements are acquired, following the procedure described in Section 2.3.1.

To get from the raw images to a measure of the liquid accumulation within the cavities, some image processing steps were applied. The different steps are illustrated in Figure 2.6, starting from the raw image on top (Figure 2.6a) and resulting in the detected liquid regions in the bottom image (Figure 2.6f). Eight cavities are in view in the images, where flow is from left to right. The raw image (Figure 2.6a) shows the large high-intensity region below the corrugations, which is caused by the liquid inside the optical box (as described in Section 2.2). The intensity distribution of the laser sheet is obtained from the captured light intensity from this region. It is subsequently used to correct the measured gray values in the images, in streamwise direction. The images are corrected for the distortion caused by the 25° viewing angle (Figure 2.6b). A moving average filter is applied (filter size 3x1 pixels) to reduce artefacts caused by wall imperfections (e.g. scratches on the surface). A 3x3 pixel median filter is applied to further reduce single-pixel noise in the images. The result is shown in Figure

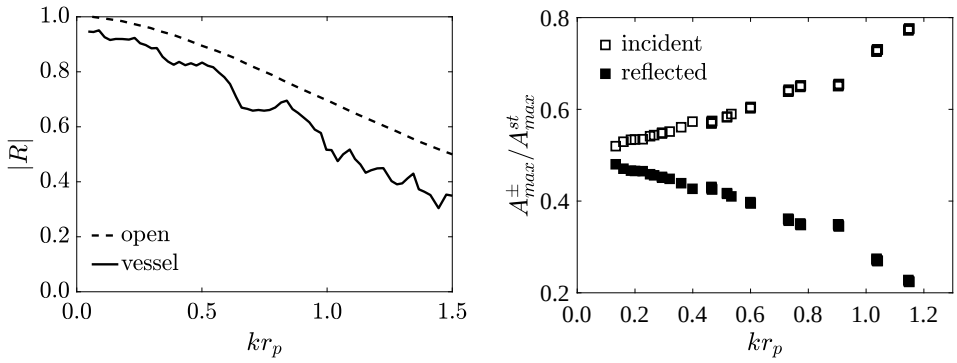

Figure 2.4: (a) Absolute value of the acoustic pressure reflection coefficient for the upstream expansion vessel as a function of kr_p (—), compared to the reflection coefficient for an unflanged open pipe end termination (- -), based on Levine and Schwinger (1948). $kr_p(=\frac{1}{2}kD_p)$, is the wavenumber, non-dimensionalized with the pipe radius. (b) Typical measured amplitude of the incident and reflected acoustic waves at the expansion vessel as a function of kr_p. The wave amplitude is made dimensionless with the maximum whistling amplitude observed in the respective standing wave. Stronger deviation at higher kr_p is due to the reduced reflection coefficient at higher frequencies.

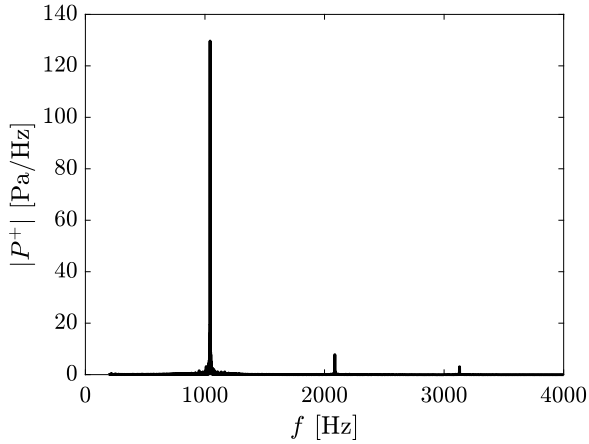

Figure 2.5: (b) Typical frequency spectrum obtained from the acoustic pressure measurements, at Ma = 0.058 ($U_b = 20m/s$).

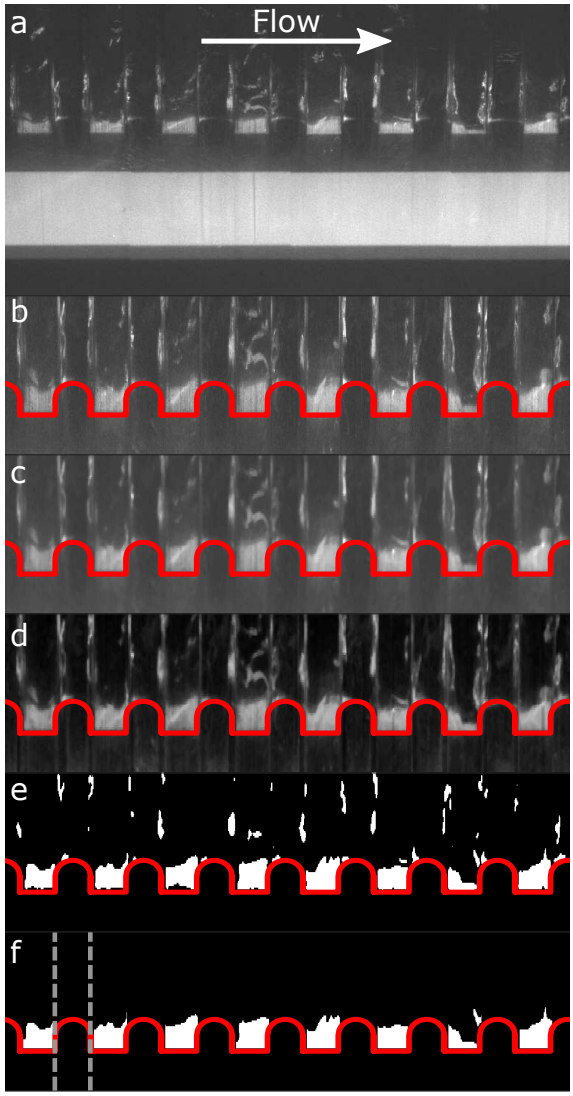

Figure 2.6: Steps taken in processing the recorded PLIF images, illustrated for the case with downward oriented flow ($U_b = 35m/s$ and $Q_l = 305mL/min$). Flow is from left to right. The internal corrugated pipe wall is drawn in red for the reconstructed images. The image processing steps are explained in the text.

2.6c. The contrast is enhanced using row-by-row stretching of the gray level (I) in the radial direction (Figure 2.6d), using:

$$I_s = \frac{I - min(I)}{max(I)}. \tag{2.11}$$

Subsequently a straightforward binarization step is applied (resulting in Figure 2.6e). Gaps between liquid filling and the rib interior are filled, and liquid regions that are entirely disconnected from the pipe wall are omitted. Furthermore only the liquid detected within the corrugations is preserved, because the regions above the curved ribs (e.g. between the dashed gray lines in Figure 2.6f) are distorted by the light refraction at the pipe wall-liquid interface. The image processing steps result in a binary filling image (Figure 2.6f), where liquid only occurs between the ribs.

Some of the shortcomings of using a PLIF-based technique for the detection of liquid accumulation in a pipe flow can be observed from Figure 2.6. The pipe wall is machined and polished afterwards. This however always leaves some surface defects, especially in the bottom corners of the cavities, that affect the transparency of the pipe locally. Apart from wall defects, total internal reflection at the gas-liquid interface also introduces errors in the amount of liquid detected. Although the viewing angle is well below the critical angle for a steady and flat interface, total reflection still occurs when the surface is inclined with respect to the pipe wall or when surface waves are induced by the gas flow over the interface. This results in an overestimation of the thickness of the liquid film close to the wall (up to a factor of two for steep surface angles in smooth walled annular pipe flow and a viewing angle of 90°; see Häber et al. 2015).

Nevertheless, the PLIF based technique is useful to observe trends in the filling behavior and to evaluate the liquid accumulation for different flow parameters.

2.4 RESULTS

2.4.1 SINGLE PHASE WHISTLING

Single phase experiments are carried out to characterize the experimental set-up and are used as a reference for the two-phase flow study presented in the subsequent section.

Figure 2.7 shows the whistling behavior of the corrugated pipe with upward directed gas flow. The whistling frequency linearly increases with increasing Mach number, indicating a fixed whistling Strouhal number (Sr). Using ($L_c + r_{ed}$) as the characteristic length scale (Nakiboğlu et al., 2010) gives a whistling Strouhal number of approximately 0.32, as shown in Figure 2.8a. The discontinuous linear increase in whistling frequency indicates a strong lock-in between axial acoustic pipe modes and the vortex shedding within the corrugations, manifested by plateaus of constant whistling frequency. This also causes the scatter in the whistling Strouhal number as observed in Figure 2.8a. The axial acoustic modes that are excited range up to a mode number ($n_a = 2L_p f / c_{eff}$) of 86, where L_p is the total pipe length. The dimensionless whistling amplitude strongly increases from the onset velocity up to a Mach number of 0.025, after which it stabilizes. For higher Mach numbers (Ma > 0.075) a gradual decrease in whistling amplitude is observed. This is caused by the reduced acoustic

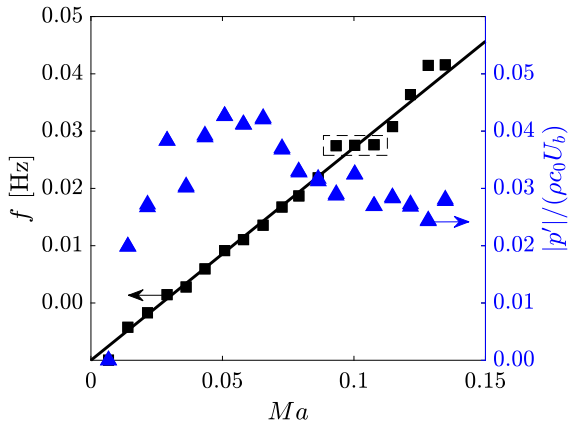

Figure 2.7: Dry whistling over the entire Mach number (*Ma*) range, with upward directed gas flow and the injection nozzle installed. Whistling frequency is displayed by ■, whistling amplitudes by ▲. The solid line indicates *Sr* = 0.32. The dashed box gives the position of the data presented in Figure 2.8b

reflection coefficient of the terminations at the upstream and downstream ends of the pipe, as discussed in Section 2.3.1.

Large variations in whistling amplitude occur in Figure 2.7. The whistling amplitude within a single plateau peaks in the middle and decreases towards the beginning and the end of the plateau (as shown in Figure 2.8b). Due to the coexistence of multiple acoustic modes at the edges of the plateaus, the total acoustic energy is divided over a larger frequency range, yielding a lower whistling amplitude at a single frequency. Since the Mach number in the dry whistling experiments is gradually increased, whistling was not always recorded at the maximum whistling amplitude occurring at a certain frequency. Dips in the whistling amplitude largely coincide with points close to jumps in whistling frequency, where both modes appear simultaneously in the frequency spectrum. For the evaluation of the attenuation of whistling by the presence of a liquid phase (described in the next section) this is not problematic, since the acoustic amplitude is always compared to the amplitude at dry whistling conditions at the same Mach number.

2.4.2 WHISTLING ATTENUATION BY A LIQUID PHASE

Upward gas flow

The injection of small amounts of liquid into the core of the gaseous corrugated pipe flow results in a clear decrease in whistling amplitude for upward oriented gas flows (Figure 2.9), similar to what was found by Belfroid et al. (2013). At the lowest gas flow rate, where *Ma* = 0.1 ($U_b = 35m/s$), the strongest effect is observed. A volume fraction is defined, based on the gas and liquid fluxes: $\Phi_l = \frac{Q_l}{Q_l+Q_g}$, where Q_l is the injected liquid flux and Q_g the gas flux. A fraction of 2×10^{-5} is sufficient to prevent the pipe from whistling at the lowest value of U_b. Higher gas flow rates require higher volume fractions of liquid to be added to the

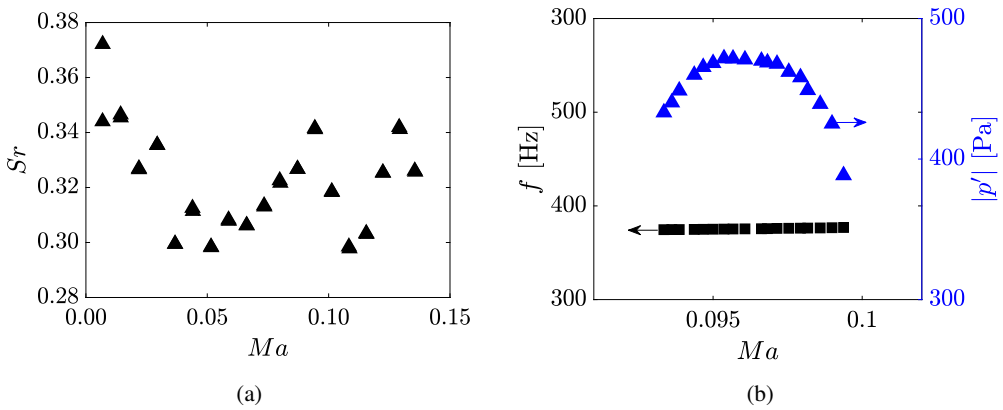

Figure 2.8: (a) Strouhal (Sr) versus Mach (Ma) number plot for dry whistling in the corrugated pipe. (b) Dry whistling amplitude as a function of Mach number at a single frequency plateau. Whistling frequency is displayed by ■, whistling amplitudes by ▲. The parameter range is indicated with a dashed rectangle in Figure 2.7.

gas flow, in order to mitigate whistling entirely. A near linear relation is found between the volume fraction of water added and the dimensionless acoustic amplitude of whistling.

Not only the whistling amplitude is affected by liquid injection, also the frequency changes. This change is however not as drastic. The whistling frequency increases by 12% to just over 25% when liquid is injected (Figure 2.10). Two effects could invoke this increased frequency. First, assuming a constant whistling Strouhal number, a decreased cavity length leads to an increase in whistling frequency. However, since the frequency does not change significantly upon increasing the liquid volume fraction in the flow further, the relation with the reduced cavity length does not seem to hold. Since the length of the cavity mouth ($L_c + r_{ed}$) is particularly important for the whistling frequency, only liquid accumulating in the cavity mouth influences this parameter. The filling of the corrugations, however, starts from the bottom corner and progresses upwards, causing the length of the cavity mouth to be fairly constant over a large range of liquid injection rates (see also Figure 2.14, which is to be discussed later). The second effect is the changed rib geometry as a consequence of the liquid flowing over the ribs. This occurs in all cases where liquid is added to the corrugated pipe flow. Since the geometry of the upstream and downstream edges are of major importance to the whistling characteristics, geometrical alterations of these rib edges are expected to affect the whistling process significantly (Nakiboğlu et al., 2010).

The sudden reduction of whistling frequency for higher liquid injection rates at $Ma = 0.109$ ($U_b = 37.5 m/s$) is caused by a jump between two acoustic pipe modes. At this flow speed, whistling is very close to the edge of a plateau, resulting in a double peaked frequency spectrum. The peaks represent two neighboring plateaus. Whistling is less stable here and switches between two plateaus at higher liquid volume fractions. This process is stimulated not only by the altered corrugation geometry, but also by an increase in the effective speed of sound due to a reduction of the cavity volume (Equation 2.1).

The PLIF images are used to obtain a measure for the cavity filling by the liquid phase. After the image processing steps (described in section 2.3.2) the filling of the individual corrugations is averaged over all images in a measurement series and over all ribs in the field of view, yielding a spatially averaged and time-averaged filling of a cavity. Figure 2.11 shows a typical

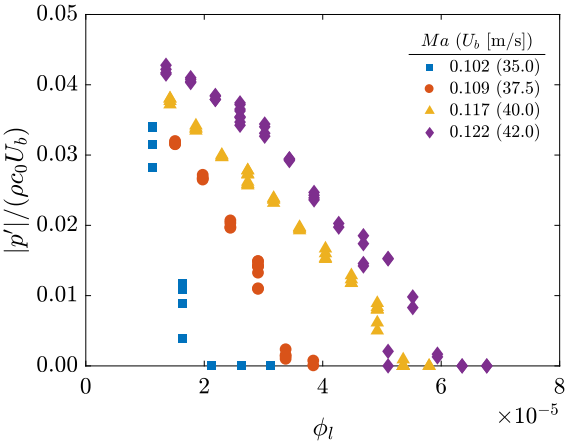

Figure 2.9: Dimensionless whistling amplitude plotted against the volume fraction of liquid injected into the corrugated pipe flow at different Mach numbers.

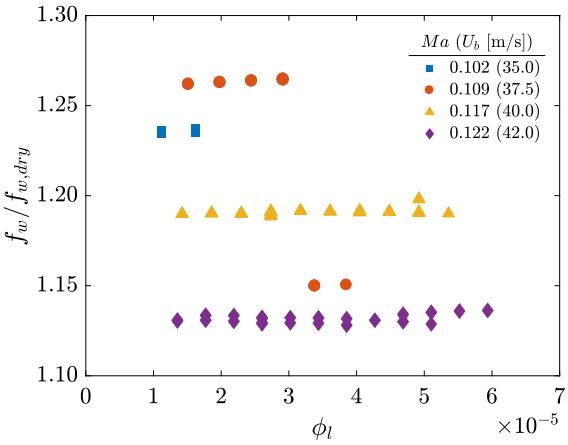

Figure 2.10: The change in whistling frequency relative to the dry whistling case as a result of liquid injection. Largest jump is observed for Ma = 0.109 ($U_b = 37.5 m/s$). The symbols are as defined in Figure 2.9

measured averaged filling profile, here for Ma = 0.117 ($U_b = 40m/s$) and $\phi_l = 1.85 \times 10^{-5}$ ($Q_l = 85mL/min$). The flow is from left to right and gravity points in opposite direction. Liquid is blown away from the downstream cavity edge due to the inertial force exerted by the incoming gas flow and due to gravity, dragging the heavier liquid towards the upstream cavity edge. The recirculating gas flow inside the cavity pushes liquid back towards the shear layer origin, where it is re-entrained in the gaseous core of the pipe flow. A more detailed analysis of these forces is given in Section 2.5. Small amounts of liquid are also found at the bottom downstream corner of the cavities, kept there by surface tension. Although the liquid that is topping the ribs is not reconstructed in the image processing, there is liquid flowing over the ribs along the pipe wall, as can be seen in Figure 2.6.

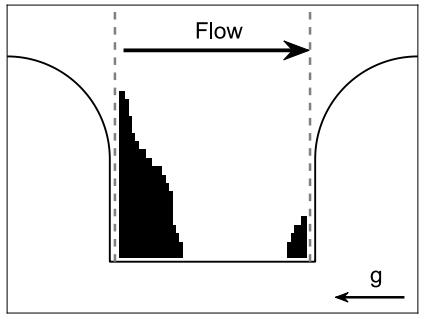

Figure 2.11: Averaged cavity filling obtained from PLIF imaging. Flow is from left to right, Ma = 0.117 ($U_b = 40m/s$) and $\phi_l = 1.85 \times 10^{-5}$ ($Q_l = 85mL/min$). Dark regions are regions of liquid accumulation and the area outside dashed lines has been masked.

The fill fraction (α, representing the amount of the cavity volume in view filled with liquid) of the averaged images is calculated, and the results are plotted against Φ_l in Figure 2.12. A clear increase in filling with increasing liquid flow rate is found, which has not been observed before. This indicates that there is a dynamic equilibrium where the liquid content of the boundary layer approaching the corrugations, plays an important role. There is a continuous refreshment of liquid inside the cavities. When switching back to the injection of fresh water, it took several minutes before the rhodamine solution is entirely replaced. Below a mean cavity filling of 30%, a linear increase with Φ_l is observed. At higher filling rates the trend departs from this linear behavior, and a slower increase in filling is obtained when further increasing the liquid volume fraction, especially at higher gas flow speeds. The gas flow rate has a large effect on α. A decrease in flow rate of 16% results in more than a doubling in α.

The open markers in the Figure 2.12 represent non-whistling cases. From the figure it follows that above a fixed filling threshold ($\alpha \approx 0.38$) no whistling is observed, independent of the gas flow rate. In all cases the whistling stops (W drops below 0.1, see Equation 2.10) when corrugations are filled above this threshold. This indicates that there is a critical filling above which whistling entirely disappears. A more detailed evaluation of this trend is found by plotting the whistling amplitude as a function of the average rib filling (Figure 2.13). All data then closely collapses onto a single curve, showing the decreasing acoustic amplitude for increasing liquid accumulation within the corrugations. The whistling amplitude steadily decreases from 10 to 30% filling, after which a stronger decline in sound production is observed upon further increasing the filling. The strong correlation between liquid accumulation in the

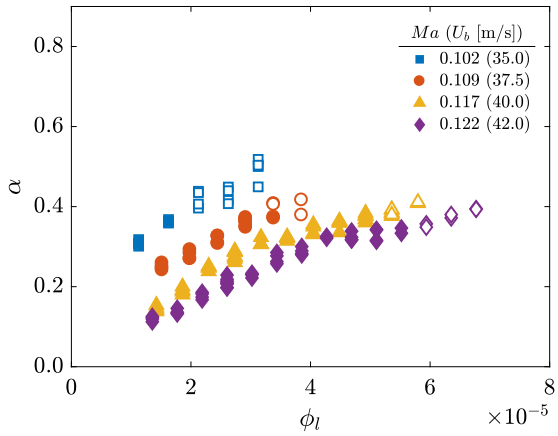

Figure 2.12: Time- and space-averaged filling of the corrugations as a function of the liquid flow rate. Closed symbols represent the whistling cases, whereas open symbols are the non-whistling cases.

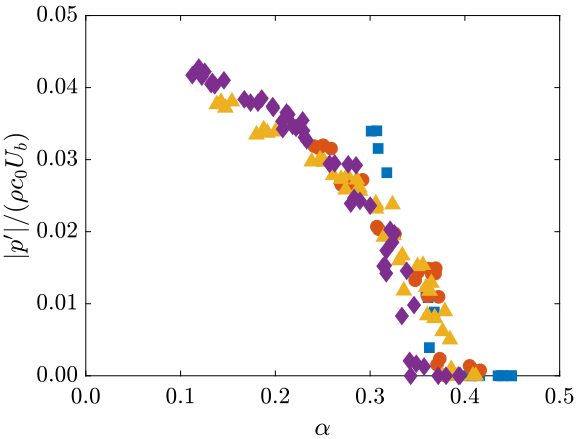

Figure 2.13: Dimensionless acoustic whistling amplitude ($|p'|/(\rho c_0 U_b)$) as a function of rib fill fraction α. Symbols are as defined in Figure 2.12

corrugations and the acoustic output shows that the filling behavior is of great importance for whistling mitigation in corrugated pipe flow with liquid addition.

A drawback of using the filling parameter is that it is related to the corrugation geometry, and therefore a geometry-dependent parameter. Furthermore, it does not provide any insight in the distribution of liquid within the corrugations and in the way corrugations are filled. To obtain further insight in the filling behavior, the depth-wise filling of the corrugations along the streamwise coordinate is plotted in Figure 2.14. It reveals that liquid mainly accumulates at the upstream side of the cavities. It also shows the strong growth in filling at the lower Φ_l range, which stabilizes at higher liquid injection rates. The filling at the downstream bottom corner of the ribs is very stable and less sensitive to changes in the incoming liquid content of the flow. A further increase of the filling there is limited by the impinging gas jet that is directed towards the cavity bottom from the stagnation point at the aft corrugation edge.

A corrected cavity length is used to further generalize the results and to make a comparison between the different cases. This length is found by identifying the space that is not occupied by liquid within the cavity for at least 50% of the time. The streamwise length of this space at $0.5H_c$ is plotted against α in Figure 2.15a. The overlap between the plotted data indicates a close resemblance of the filling profiles at different gas flow speeds. The region between $0.6 \leq L_c^*/L \leq 0.7$ seems to be critical since the whistling amplitude strongly decreases in this region (see Figure 2.15b). This critical behavior could be related to the effective length of the cavity, dropping below the whistling threshold governed by the cavity length over the momentum thickness of the incoming boundary layer (L_c^*/θ; see Gharib and Roshko 1987). Also the changed upstream rib geometry might be causing the reduction in noise production. The alteration of the rib geometry by liquid flowing over the rib can directly change the shear layer dynamics and, hence, the acoustics. Nakiboğlu et al. (2010) showed that an alteration of the upstream rib can have a significant effect on the whistling amplitude. As the rib edge becomes sharper (r_{ed} goes down), an increased sound absorption takes place due to a local increase of the tangential acoustic velocity, yielding a reduction in acoustic source strength.

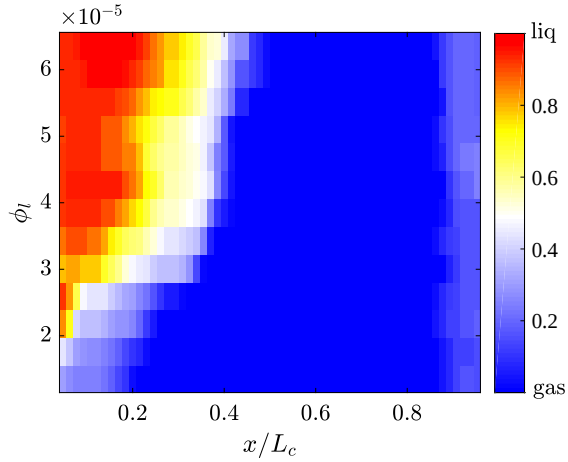

Figure 2.14: Development of filling plotted over the cavity length for different liquid injection rates at $Ma = 0.122$ ($U_b = 42m/s$). The color indicates the part of the corrugation depth filled up by liquid at a certain streamwise position along the cavity. Gas flow is from left to right.

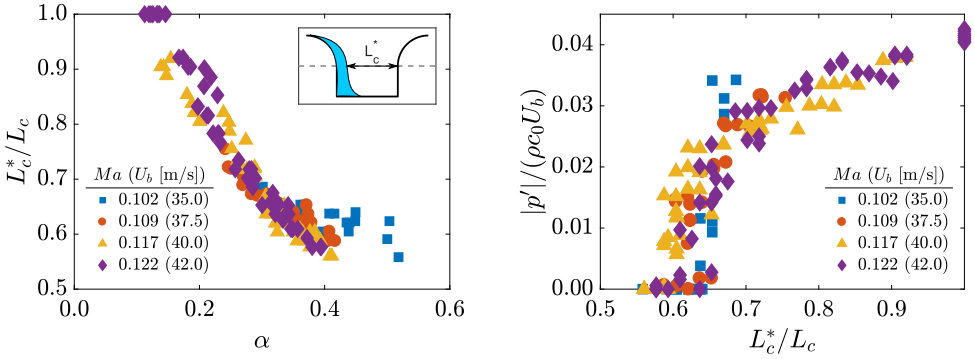

(a) (b)

Figure 2.15: (a) Corrected cavity length L_c^*, sampled at half cavity depth versus rib fill fraction α. The insert shows the definition of L_c^*. (b) Dimensionless acoustic whistling amplitude $|p'|/(\rho c_0 U_b)$ relative to the corrected cavity length L_c^*.

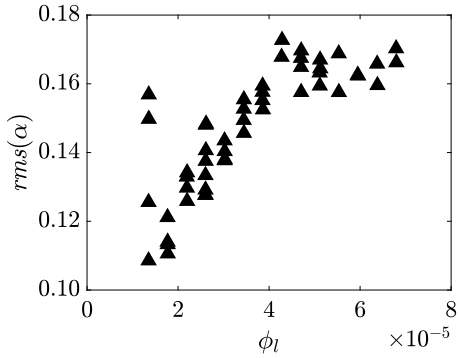

Figure 2.16: Root-mean-square values of the spatial variation in filling ratio α over the ribs in the field of view as a function of the liquid addition rate and for Ma = 0.122 ($U_b = 42m/s$)

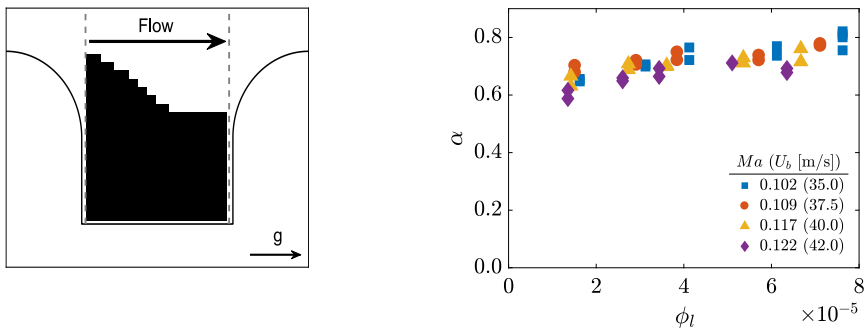

(a) (b)

Figure 2.17: (a) Averaged rib filling for downward oriented gas flow. Flow is from left to right, Ma = 0.117 ($U_b = 40m/s$) and $\phi_l = 1.85 \times 10^{-5}$ ($Q_l = 85mL/min$). Dark regions are regions of liquid accumulation and the area outside dashed line has been masked. (b) Fill fraction in the downward experiments for different liquid volume fractions in the incoming flow. Compare with Figure 2.12 for upward gas flow.

Apart from the filling itself, temporal and spatial variations of the liquid accumulation in the individual ribs might be relevant for the whistling amplitude reduction in these pipes, effectively breaking the axial periodicity of the corrugations. Figure 2.16 shows the root-mean-square (rms) values of the filling variations in space as a function of liquid injection rate. A slight increase of variations in α with increasing ϕ_l is observed, but it is rather limited when compared to the accompanying increase in α from 0.1 to 0.4. The fill fraction itself therefore seems to be more important for the whistling behavior of the corrugated pipe than the variability in the filling.

Downward gas flow

The filling pattern of the corrugations along the pipe is demonstrated to be essential for upward directed flow. To modify the typical filling behavior the set-up is turned upside-down, effectively changing the direction of the gravity vector and thereby changing the filling profile of the corrugations. The gas flow is now in the downward direction and has the same orientation as the gravity vector.

The whistling behavior of the corrugated pipe *without* liquid injection was very similar to the upward oriented gas flow results. Small differences in whistling amplitudes could be explained from differences in piping length between the two cases.

When liquid is injected to the incoming gas flow, whistling is eliminated completely, even for the lowest liquid fractions. The onset velocity increases to a value above $U_b = 42m/s$ (Ma = 0.122), which is the maximum that could be reached with the current set-up. PLIF imaging of the individual rib filling showed a substantial increase in filling compared to the upward oriented gas flow case, for the same incoming liquid fraction. A typical filling profile for a cavity in the downward experiments is shown in Figure 2.17a. As for the upward directed case, liquid tends to accumulate close to the upstream cavity wall. However, in this case almost the entire cavity is filled with liquid. For all cases, filling increases to values above 60% of the corrugation volume (Figure 2.17b). The cavities therefore experience a filling that is always higher than the whistling threshold, found in the upward directed gas flow experiments. Furthermore, an increase in the liquid volume fraction causes only a slight increase in liquid accumulating in the corrugations, and the trend is comparable for different gas flow speeds. This reveals that the liquid filling in these flow conditions is more stable, reaching an equilibrium that is almost insensitive to Φ_l.

2.5 DISCUSSION

Several mechanisms behind the whistling mitigation by liquid addition were proposed by Belfroid et al. (2013). Here we recapitulate these proposed mechanisms: (1) filling of corrugations with liquid, reducing the depth of the cavities; (2) additional acoustic damping due to the (dispersed and annular) two-phase flow; and (3) a reduced acoustic source strength due to an increased boundary layer thickness. Based on the findings in the present work it appears that mitigation of whistling is related predominantly to the filling of the cavities. There is a strong correlation between the filled geometry and the acoustic output, for different free stream velocities. The first mechanism therefore, seems to be dominant. Reduction of the whistling amplitude can then be related to a reduction of cavity size, a changed geometry of the upstream cavity edge, or a reduction of the cavity length, resulting in a sub-critical L_c/θ ratio where no whistling occurs.

Although in many applications corrugated pipes are applied in upward flow direction, downward experiments are carried out to confirm the importance of cavity filling when it comes to a reduction of sound production. The differences between upward and downward experiments can be interpreted from the forces influencing the liquid accumulation within the corrugations. These forces are described in Section 2.1.2. The main difference between *downward* and *upward* flow is the direction of the gravity vector with respect to the flow direction. The Bond and Weber number range, presented in Table 2.1, show the significance of gravity in the studied experimental conditions. In downward orientation gravity is aligned with the flow direction, whereas in upward orientation it is against the flow direction. This would cause the gravitational force to prevent emptying of the corrugations in the *downward* flow case, whereas it would promote emptying of the corrugations in the *upward* flow case, leading to the different filling behavior observed in the experiments.

2.6 CONCLUSIONS AND OUTLOOK

The present study provides more insight in the mechanisms behind the mitigation of whistling in corrugated pipes by means of liquid addition. This is achieved by an experimental investigation into whistling in upward oriented flow through corrugated pipes, using a combination of acoustic measurements to reconstruct the acoustic waves in the pipe and PLIF imaging of the liquid accumulating in the cavities.

The acoustic measurements show that the amplitude of whistling decreases linearly with increasing liquid volume fraction in the incoming flow. The reduction in sound amplitude is strongest for lower gas velocities, resulting in an increase of the onset velocity of whistling to values above 30 *m/s* for the lowest liquid volume fractions possible in the current set-up. The PLIF images are used to identify the amount of liquid accumulating in the corrugations. A filling threshold is found above which no whistling occurred, within the observed range of gas flow velocities. Furthermore, there exists a strong correlation between the attained reduction in whistling amplitude and the fill fraction of the corrugations. This indicates that the amount of liquid filling is a very important factor in reducing the sound production from corrugated pipes.

To confirm these findings the flow direction is reversed (to downward oriented flow). The resulting filling behavior is entirely different when the flow was from top to bottom. A significantly higher filling of the corrugations is exhibited over the entire range of gas flow speeds and liquid fractions added, explaining the absence of whistling in experiments with downward oriented gas flow. The effect of the gas flow speed and liquid volume fraction on the filling is considerably smaller compared to upward oriented flow, indicating a more stable filling behavior. This is caused by the change in direction of the gravity, which in downward flow experiments counteracts the inertial forces whereas in upward flow experiments it works together with the inertial forces to empty the corrugations. The higher filling ratio in downward oriented gas flow results in an absence of whistling, irrespective of the gas flow rates and liquid injection rates.

Geometrical alterations are likely the main source of whistling mitigation in two-phase flows in corrugated pipes. Rib-to-rib fluctuations do not increase significantly upon increasing the liquid fraction in the inflow and are not expected to be essential for noise reduction. The effective shortening of the cavity length could eventually lead to reduced values of L/θ of the incoming boundary layers, eventually below the whistling threshold. Furthermore, a geomet-

ric alteration of the upstream cavity edge could also reduce whistling. These two mechanisms are expected to play an important role in noise reduction in corrugated pipe flow by liquid addition. Future work should encompass parametric studies to investigate the effect of the corrugation geometry and liquid properties on whistling mitigation by a liquid phase. Also the effect of other possible noise mitigation mechanisms (acoustic damping due to droplets, shear layer disruption) should be studied in more detail. This would give a broader insight in the individual effects of the different mechanisms.

3

ANNULAR TWO-PHASE FLOW IN VERTICAL SMOOTH AND CORRUGATED PIPES

Two-phase flow in ribbed or corrugated pipes is of interest in many industrial applications. Experiments are performed to assess the flow regime characteristics in upward annular flow through vertical smooth and corrugated pipes. From high speed recordings, the flow regime and temporal film characteristics are obtained. A novel implementation of a planar laser-induced fluorescence (PLIF) method is used to measure the film thickness, preventing strong reflections from deteriorating the measurements. Liquid accumulation between the ribs of the corrugated pipe is also measured using a PLIF technique. Furthermore, droplet sizing is performed combining shadowgraphic and interferometric techniques to capture a large droplet size range. The measurements show that the presence of pronounced corrugations at the pipe wall causes a strong increase in entrainment of liquid into the gas flow. The entrainment is correlated to the filling of the corrugations with liquid; it is significantly reduced (from 90% entrainment to 50%) when the corrugations are entirely filled with liquid. The amount of liquid filling of the corrugations is related to the superficial liquid film flow velocity. The liquid filling fraction (α) scales with the Weber and liquid Reynolds number, and the obtained scaling also holds when the experiments are repeated with a different liquid (mono-ethylene glycol) and with a larger corrugation geometry. Droplets occurring in corrugated pipe flow are 30-50% larger compared to the smooth pipe, as a consequence of the locally (at the locations of the cavities) increased film thickness.

This chapter is based on: A.C. van Eckeveld, E. Gotfredsen, J. Westerweel, C. Poelma, “Annular two-phase flow in vertical smooth and corrugated pipes”, *International Journal of Multiphase Flow*, 109: 150-163, 2018.

3.1 INTRODUCTION

Ribbed or corrugated pipes are used in many industrial applications. They are for example applied as flexible flowlines and risers in the oil and gas industry. Other applications are primarily found in processing units in production plants (e.g. food and chemical industry), where heat and mass transfer are important. Axisymmetric or helical inserts have been shown to increase heat and mass transfer coefficients drastically under certain conditions. In many of these applications two-phase flows occur, having a low liquid loading. There is, however, limited understanding of the effect of ribs and corrugations on the flow regimes occurring in two-phase flows through these pipes. Experiments are carried out to investigate the two-phase flow behavior in smooth and corrugated vertical pipes, operating in the annular flow regime. In this regime, a thin film transports a part of the liquid along the pipe wall. Liquid entrainment from the film into the gas core results in a fraction of the total liquid flow rate being transported as droplets.

Co-current two-phase flow in smooth vertical pipes has been subject of many studies. Azzopardi (1997) provides a thorough summary of this work. More recent contributions are provided by e.g. Belt et al. (2010), van 't Westende et al. (2007), and Sawant et al. (2008, 2009). In literature, the occurence of upward annular flow is related to either the ability to suspend the dispersed phase (Turner et al., 1969) or the stability of the film at the wall (Zabaras et al., 1986). Either way, there exists a critical gas flow velocity below which the film is not sustained and a transition to churn flow is observed. For pipes with a 50 *mm* inner diameter subject to an air-water flow under atmospheric conditions, this critical gas flow velocity is approximately 14 *m/s* (Taitel et al., 1980). Pressure drop, entrainment ratio, void fraction and wave characteristics in vertical annular flow are reasonably well understood. For very low liquid flow rates, a full film is not sustained: the film breaks up and liquid is transported in rivulets along the pipe wall (Hewitt, 1965). For higher liquid flow rates, the full film is mainly characterized by two types of waves: capillary ripples and disturbance or roll waves (Azzopardi, 1997). Disturbance waves are the main source of liquid entrainment into the gas core (Arnold and Hewitt, 1967; Cousins and Hewitt, 1968; Azzopardi and Whalley, 1980). The inception of disturbance waves is therefore an important parameter when studying liquid entrainment in annular pipe flow. Azzopardi (1997) is one of various other authors proposing a criterion for the inception of disturbance waves, below which no significant entrainment is expected. According to Ishii and Grolmes (1975), entrainment is suppressed if the film Reynolds number[1] is smaller than 160, due to the absence of disturbance waves. Sawant et al. (2009) showed that the presence of disturbance waves is a necessary condition for the onset of entrainment, but not sufficient in itself. Especially at lower gas flow rates disturbance waves can occur without significant entrainment.

Two mechanisms for droplet formation from disturbance waves have been identified (Azzopardi, 1997). Figure 3.1 gives a schematic representation of these two mechanisms. At lower gas and liquid flow rates, the bag break-up mechanism is dominant. Part of the wave is undercut by the gas flow, resulting in the formation of droplets. The second mechanism, occurring at higher gas flow speeds, is the ligament break-up mechanism, where a ligament is sheared from the waves by the high speed gas phase. This mechanism occurs over a large range of operating parameters. Several studies aimed to model the entrainment rate in annular pipe flow. Ishii and Mishima (1989) used the onset of entrainment criterion developed by Ishii and Grolmes

1 $Re_f = 4\rho_l u_f \delta / \mu_l$, with u_f the average film velocity and δ the film thickness

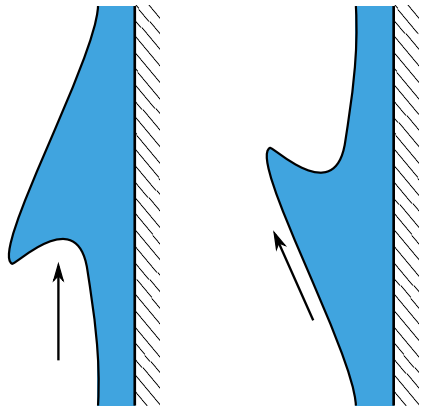

Figure 3.1: Schematic representation of the two main droplet formation mechanisms in upward annular smooth pipe flow: bag break-up (left) and ligament break-up (right).

(1975), to come up with an entrainment correlation. The correlation is based on the assumption that the excess liquid, above the entrainment onset limit, is entrained into the gas flow. They found a liquid Reynolds number dependency in the transition regime ($160<Re_f<1635$), and also introduced a viscosity dependency. This viscosity dependency is not warranted according to Wallis (1968). Pan and Hanratty (2002) developed a similar correlation, without the liquid Reynolds number and viscosity dependency.

The influence of non-smooth pipe walls on the two-phase flow is less well understood, but very relevant in applications such as corrugated risers (Belfroid et al., 2013), ribbed wall heat exchangers for boiling and condensation (Agarwal and Rao, 1996), and mass transfer applications (Kukreja et al., 1993). Two-phase flow in corrugated pipes is mainly studied in the context of internal helical wires or other types of inserts in smooth pipes. Heat transfer coefficients can be significantly increased when these type of inserts are used. This behavior, however, is strongly dependent on the appearing two-phase flow regime. Several studies are devoted to the flow regime boundaries in two-phase flows through pipes with inserts. Agarwal and Rao (1996) found a significant increase of the heat transfer coefficients, related to the existence of the annular flow regime over a larger range of flow parameters, accompanied by an increased film thickness. Kim et al. (2001) showed that, for counter-current two-phase flow in a coiled pipe, the flow pattern transition lines moved to lower gas flow velocities. This was confirmed by e.g. Ansari and Arzandi (2012) for horizontal channels with ribs. Recently, new attention was given to two-phase flows in corrugated pipes in the framework of the mitigation of flow-induced vibrations in these pipes (Belfroid et al., 2013; van Eckeveld et al., 2017). The presence of liquid was found to reduce, and eventually mitigate, flow-induced noise. In this application, it is important to determine the minimum liquid loading required to prevent vibrations to occur, which is strongly influenced by the flow regime.

There is very limited knowledge about the effect of wall roughness on two-phase flow behavior in the annular regime. The present work aims at understanding the effect of axisymmetric ribs along a pipe wall on the flow pattern in vertical co-current two phase flow. In dry gas flow through these pipes, the quasi-stagnant flow inside the corrugations is separated from the flow through the core of the pipe. A recirculation cell is formed inside the cavities, which scales with the cavity size. There is a large variety of cavities, classified based on their geometry

and internal flow structure. The geometries studied in this work are so-called shallow open cavities, where the shear layer extends to the downstream end of the cavity, and a single recirculation zone is formed inside the cavity. This regime occurs when the length over depth ratio of the cavity is $\lesssim 8$. The specific threshold value for this regime is case and flow dependent. A schematic representation of this type of flow is provided in Figure 3.2.

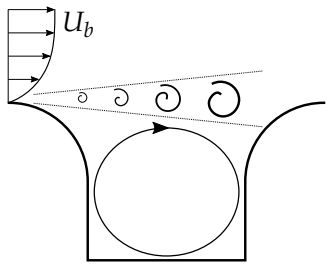

Figure 3.2: Typical cavity flow in a corrugated pipe, subject to dry gas flow. The incoming gas flow separates at the upstream cavity edge, forming a shear layer where vortical structures can appear. The shear layer separates the bulk flow inside the main pipe from the recirculating flow in the cavities.

The work described in this chapter adds to understanding the effect of a corrugated pipe wall on the flow behavior in the annular regime. The behavior of liquid at the pipe walls, the entrainment ratio and the resulting droplet sizes are assessed, both for smooth and corrugated pipes. Two different corrugation geometries are studied, and water and mono-ethylene glycol (MEG) are used as working liquids, with air as the gas phase. The measurements are carried out in an open flow loop, described in Section 3.2, together with the experimental methods. Different measurement techniques are used to investigate the flow behavior. The film thickness in smooth pipes is measured using a *planar laser-induced fluorescence* (PLIF) technique, adapted to remove the effect of total internal reflections at the gas-liquid interface. Droplet sizing is carried out using shadowgraphy and interferometry, alongside entrainment measurements. Liquid accumulation inside the cavities is also assessed using a PLIF based technique. Measurement results for the smooth and corrugated pipes are provided in Section 3.3 and 3.4, respectively. The results are discussed in Section 3.5. Section 3.6 provides the conclusions from the present study.

3.2 EXPERIMENTAL

3.2.1 EXPERIMENTAL SET-UP

The measurements are carried out in an open flow loop with a vertical test section (depicted in Figure 3.3). The air flow through the pipe is provided by a blower (Esam Mediojet 2V). Gas flow rates are measured with a zero β-ratio, long-radius ASME flow nozzle (Leutheusser, 1964). The superficial gas and liquid velocities are used to characterize these flow rates ($u_{sg} = Q_l / A_p$ and $u_{sl} = Q_g / A_p$, with Q being the volume flow rate of the respective phase and A_p the pipe cross sectional area). After passing through the expansion vessel, the flow is directed upward and liquid is injected with spray nozzles located at the pipe center line (Bete PJ8, PJ10, PJ15, PJ24 and PJ32). Various nozzles are used for different liquid flow rates. Although they produce slightly different sprays, the effect on the results is found to be negligible. A

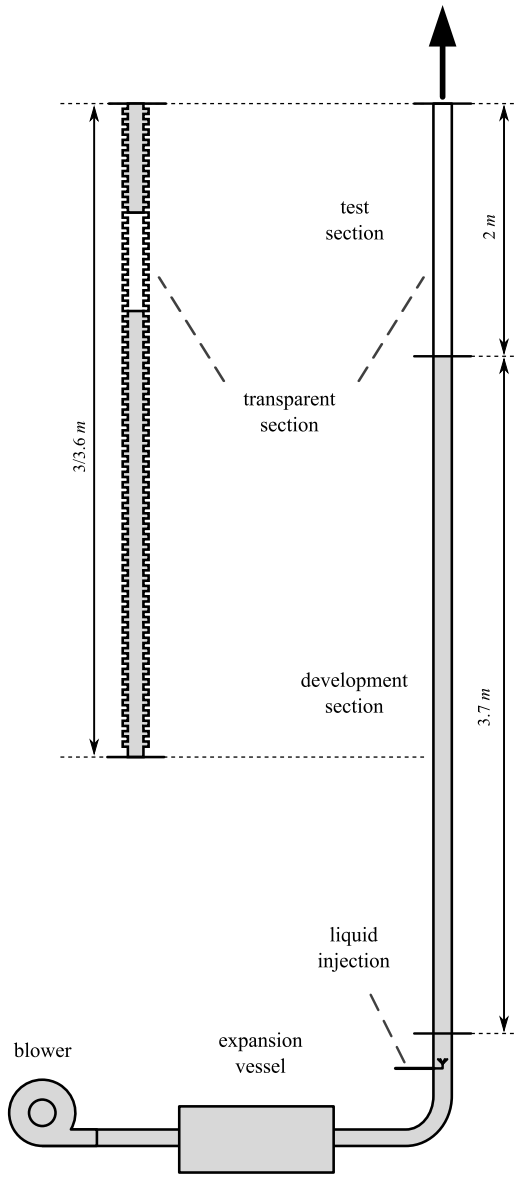

Figure 3.3: Schematic representation of the experimental set-up. The gas flow is created using a blower, followed by an expansion vessel which reduces the noise amplitude from the blower. Liquid is injected with a spray nozzle at the pipe center. The test section is transparent and can be replaced by a corrugated pipe section.

rotary vane pump (Fluid-O-Tech PA111) drives the liquid flow. The nozzles produce a dispersed spray of droplets with a nominal diameter less than 150 μm. The liquid flow rate is measured with a Coriolis mass flow meter (Bronkhorst M14 CORI-FLOW). For flow development purposes, a 3.7-*m* long smooth pipe section ($L_p/D_p \approx 75$, with D_p being the inner pipe diameter, which is 50 *mm*) is placed behind the liquid injection point. It is made of steel, with a wall thickness of 5 *mm*. It is followed by a transparent plexiglas measurement section, which also has a wall thickness of 5 *mm*. The measurements are taken at approximately 84 pipe diameters downstream of the liquid injection point. The flow loop is terminated with an open outflow. Temperature measurements are performed at the outlet using a Pt100 temperature probe located at the pipe center-line. The temperature measurements, together with pressure measurements upstream of the liquid injection point, are used to correct the mass density of the gas. For the experiments with corrugated pipes, the last three meters ($L_p/D_p \approx 61$) of the flow loop are replaced with a PVC corrugated section. Due to the wide range of applications (from different heat-exchangers to industrial risers), there is a large variety in geometrical characteristics that are of interest for corrugated pipe flow. For the present study, we limit ourselves to two different general corrugation geometries. Both pipes have rectangular corrugations with a cavity height over over length ratio of 1 ($H_c/L_c = 1$).

The upper rib edges are rounded (with the edge rounding radius r_{ed}) as is found in many applications (e.g. tape-wire inserts in heat and mass transfer enhancement applications). The pitch (P_c) is limited, to fit a sufficient number of corrugations in the vertical distance in order to ensure full flow development. A schematic representation of the used geometries is depicted in Figure 3.4. The dimensions are given in Table 3.1. For optical access a transparent corrugated section is placed just before the end of the corrugated pipe, at $49 \leq L_p/D_p \leq 53$ from the corrugated pipe entrance.

3.2.2 HIGH SPEED IMAGING

To characterize the annular liquid film at the pipe wall, a combination of high speed imaging and *planar laser-induced fluorescence* (PLIF) is used. From the high speed images, the flow regime and temporal film statistics are obtained. A Photron Fastcam APX 1*MP* camera is used, equipped with a 105 *mm* Micro-Nikkor objective. The transparent section is illuminated from the back using an LED panel. A grid with alternating black and white lines is placed between the light source and the pipe to increase contrast of the gas-liquid interface in the visualization images. Images are recorded at 700 *Hz*, which is sufficient to capture the dynamic behavior of the film.

3.2.3 FILM THICKNESS MEASUREMENTS

The film thickness is obtained from the PLIF measurements. The method used before by e.g. Schubring et al. (2010) is adapted for this purpose, with the aim to remove large reflections at the gas-liquid interface. The set-up is schematically depicted in Figure 3.5a. A laser sheet (from an Nd:YAG LitronLasers Nano L 50-50) illuminates the liquid film. The liquid contains a fluorescent dye (150 $\mu g/L$ rhodamine WT). The fluorescent light is recorded using a CCD camera (LaVision Imager LX 16M), equipped with a 105 *mm* Micro-Nikkor objective with a red filter (B+W 62 041) in front of it. The viewing angle is optimized in terms of wall-normal

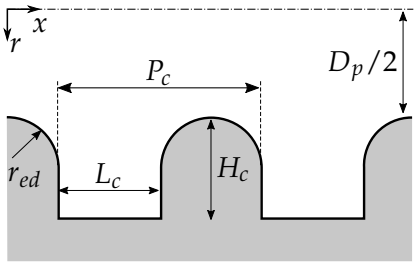

Figure 3.4: Cross-section of the corrugation geometry. The symbols are explained in text and numerical values for the used geometries are given in Table 3.1.

		geom A	geom B
D_p	[mm]	49.25	49.25
L_c	[mm]	4	6
H_c	[mm]	4	6
P_c	[mm]	6	10
r_{ed}	[mm]	2	2
L_p	[m]	3	3.6

Table 3.1: Dimensions of the different geometries used. Symbols are explained in the text, and a schematic of the corrugation layout is provided in Figure 3.4.

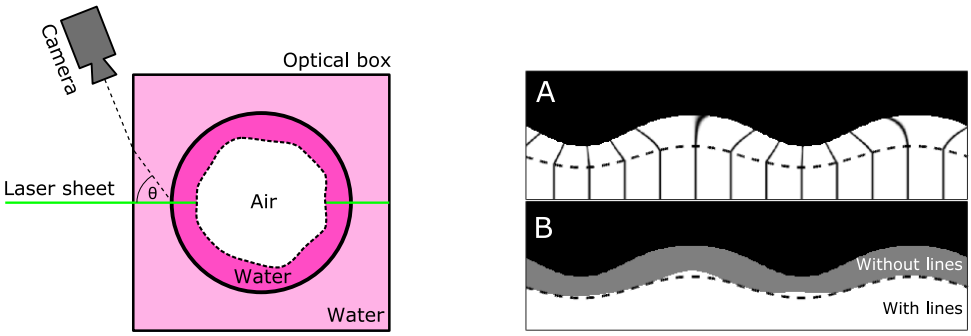

(a) (b)

Figure 3.5: (a) Schematic of the PLIF set-up used for the film thickness measurements, seen from the top. The water at the interior of the pipe is dyed with 150 $\mu g/L$ rhodamine WT, water in the optical box with 50 $\mu g/L$. (b) Example images obtained using an inverse ray-tracing technique for θ of 75°, with (A) the image obtained by the sensor (the dashed line indicates the actual gas-liquid interface), and (B) the results obtained with and without using the line detection method.

spatial resolution of the film and the amount of reflections observed, resulting in an angle w.r.t. the laser sheet (θ in Figure 3.5a) of 75°.

A drawback of the described optical technique is the overestimation of the film thickness due to total internal reflections at the air-water interface. Häber et al. (2015) showed that the overestimation of the film thickness could reach a factor of two for steep waves. In order to reduce this error, the regular light sheet used by Schubring et al. (2010) is replaced by a *lined* light sheet. A comparable method is presented by Charogiannis et al. (2017), for downward annular pipe flow. The light sheet consists of alternating light and (smaller) dark regions, as is visible in Figure 3.6. The dark lines are generated by passing the light sheet through a grid, thereby creating shadows behind the grid lines. A reflection of the light sheet at the wavy air-water interface will cause the lines to deviate from their straight path, enabling a distinction between the actual film and the reflections. A drawback of this method is the reduced spatial resolution of the film thickness measurement in axial direction. The spatial resolution in the streamwise direction is now associated with the number of grid lines in the light sheet, instead of the number of pixels in that direction. No prism is used in the experiments. Since the camera is relatively far away (paraxial approximation is allowed), knowing the pipe wall thickness and the spacing of the dark lines in the light sheet is sufficient to spatially calibrate the system.

An inverse ray-tracing technique is used to validate the method. Figure 3.5b shows an example image obtained with this technique for a simple sine wave. The initial position of the lines is obtained using a peak-find algorithm, with the average image as input. Deviation of the lines is detected using a run-length encoding script, determining the first wall-normal location where the lines show a 2 pixel deviation from the initial position over at least 5 pixels in wall-normal direction. For this artificial wave the improvement in film thickness measurement is evident. Only where the light rays have a (near-)perpendicular angle of incidence with respect to the gas-liquid interface, the wave height is overestimated.

This technique is applied to the film thickness measurements in a smooth pipe. Line spacing was chosen to be 1 *mm*, which is deemed sufficient to capture most waves, keeping in mind the capillary length scale (2.7 *mm* in the air-water case). Decreasing the line spacing further would complicate the line detection method. Figure 3.6 shows a part of a typical image obtained from these measurements, visualizing the improvement when the line detection method is implemented.

3.2.4 CAVITY FILLING MEASUREMENTS

The liquid accumulation inside the cavities of the corrugated pipe is also measured using a PLIF-based method, similar to the film thickness measurements. In this case, the reflections at

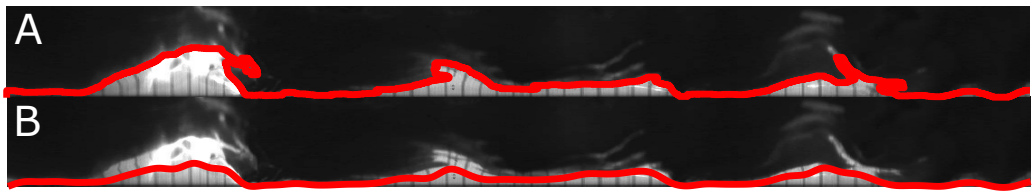

Figure 3.6: Comparison of film thickness from binarization (A) and using the novel line detection method (B). Large reflections can be detected in B because of the deviation of the lines.

the air-water interface are reduced by reducing the viewing angle with respect to the laser sheet. The line detection method is not used here, as the resolution in axial direction is important.

An angle of approximately 25° is used between the laser sheet and the camera. With a steady and perfectly axisymmetric gas-liquid interface within the corrugations, this yields a viewing angle well below the critical angle for air-water (= 48.6°) and air-mono-ethylene glycol (= 44.0°). The dye concentration is optimized for the required intensity of the emitted fluorescent light, resulting in a concentration of 125 $\mu g/L$. Furthermore, the optical box is filled with a rhodamine solution of approximately 50 $\mu g/L$, and the fluorescent light emitted from this region is used to correct for non-uniformity in the laser sheet. A typical image obtained with water injection in a corrugated pipe with geometry B is depicted in Figure 3.7. Regions of high intensity corresponds to liquid accumulation. The white boundaries are obtained after processing, and indicate the filling area. More details about the different processing steps can be found in Chapter 2 and in van Eckeveld et al. (2017).

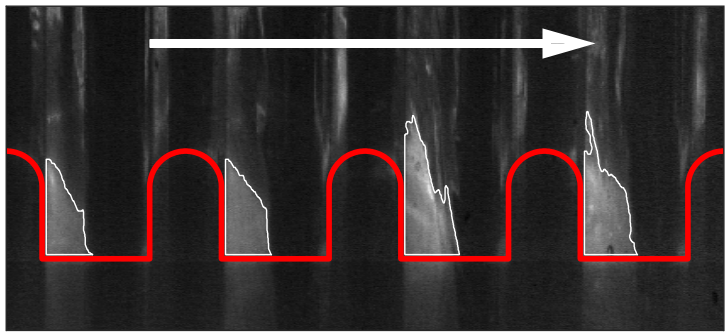

Figure 3.7: Typical image of liquid accumulation in cavities for a corrugated pipe with geometry B (see Table 3.1). Flow is from left to right. The corrugated wall is marked with the red line, the white boundaries are obtained from image processing and indicate the filling regions.

3.2.5 FILM FLOW RATE AND DROPLET SIZES

Droplet sizes are measured at the pipe end, after removal of the liquid film attached to the wall. The film is removed using a slit (as was applied by e.g. Hay et al., 1996). The slit is circular, with a wedge shaped edge. The internal diameter of the slit is 4 *mm* less than the internal pipe diameter. The film is collected between the slit and the inner pipe wall, and is directed to a separate container (see Figure 3.8). The mass of the container is recorded over a period of at least eight minutes, to obtain the film flow rate.

Droplet size distributions are measured after film removal, with a combination of *shadowgraphic particle imaging* (SPI) and *interferometric particle imaging* (IPI, Glover et al. 1995). The techniques are combined to capture a large range of droplet sizes. A schematic overview of the SPI set-up is provided in Figure 3.9. Images are acquired using a CCD camera (LaVision Imager LX 16M) equipped with a 200 *mm* focal length Micro-Nikkor objective. Behind the pipe, a diffuse white background is lit by a pulsed Nd:YAG laser (LitronLasers Nano L 50-50). The droplet shadows are subsequently recorded. Several image processing steps are applied. First, a background correction is applied, followed by a median filter (3x3 pixels) to reduce noise. The droplet edges are found using a canny filter and the contours are filled with a convex hull technique (Gonzalez and Woods, 2012). From the resulting binary image, the

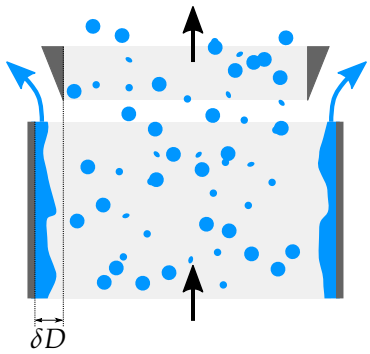

Figure 3.8: Schematic representation of the slit used to remove the film from the pipe wall. δD indicates the gap width between the inner pipe wall and the slit edge, which is 2 *mm* at each side.

droplet sizes are obtained, assuming spherical droplets. A typical example of an SPI image obtained after background subtraction and the application of a spatial median filter is depicted in Figure 3.9. The droplet size range that can be measured using this technique is limited by the spatial resolution of the images and by the optics. The spatial resolution in the reported experiments is approximately 12.5 $\mu m/pixel$. Furthermore, the diffraction limit of the imaging system is around 25 μm. It is therefore difficult to obtain reliable drop sizes for droplets with $d_p < 50\ \mu m$ using shadowgraphy.

An interferometric technique is used to measure droplets with smaller diameters. The droplets are illuminated with a 1 *mm* thick laser sheet, as is schematically depicted in Figure 3.10. The same camera is used for the SPI and IPI measurements. It is placed at an angle of 70° with the laser sheet, and the Scheimpflug condition is fulfilled to obtain equal focusing over the entire field of view (Adrian and Westerweel, 2011). The 70° angle results in a high signal-to-noise ratio of the interference fringes, especially when laser light with a parallel polarization is used (Damaschke et al., 2005). A separate circular aperture is placed in front of the camera lens. Illumination of a spherical droplet with a light sheet results in two glare-points at both sides of the droplet. A defocused image of these glare points yields a disk with an interference pattern due to the monochromatic laser light that is used. A typical raw IPI image is depicted in Figure 3.10. There is a direct relation between the spacing of the fringes and the droplet size. When the ratio of refractive indices of the droplets and the surrounding fluid is larger than unity ($m = \frac{n_l}{n_g} > 1$) this relation is (Damaschke et al., 2005):

$$d_p = \frac{2\lambda}{\Delta\psi}\left(\cos(\theta/2) + \frac{m\sin(\theta/2)}{\sqrt{m^2 - 2m\cos(\theta/2) + 1}}\right), \tag{3.1}$$

with d_p being the droplet size, λ the wavelength of the used light, $\Delta\psi$ the angular fringe spacing, and θ the viewing angle. The advantage of using an interferometric technique is that the size of the interference disks is not related to the droplet size, but rather to the optical choices made in designing the set-up. Small droplets yield a large $\Delta\psi$, and the lower bound of the droplet size that can be measured is solely determined by the aperture size and the working distance. The detection of large droplets is limited by the spatial resolution of the camera image as it corresponds to the smallest fringe spacing that can still be detected accurately. A correlation method is used to locate the droplets in the images. The entire image is correlated

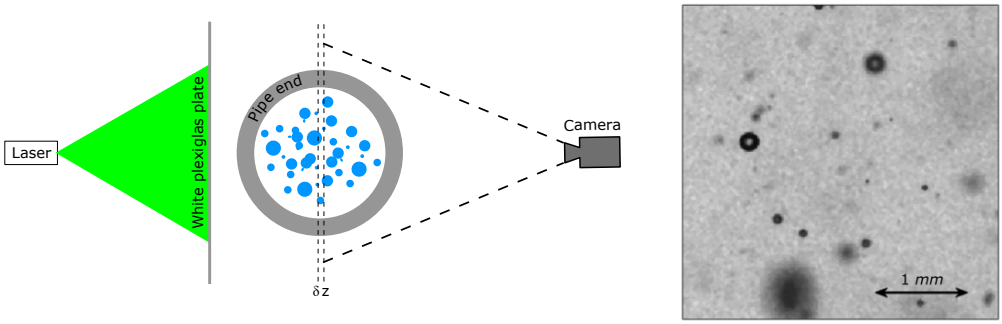

Figure 3.9: Schematic representation of the shadowgraphy set-up (left), where δz depicts the depth of focus of the imaging system. A cut-out of a typical image obtained using the shadowgraphic measurement technique (right), after background subtraction and the application of a median filter. Dark spots are the shadows of droplets, used to find the droplet size.

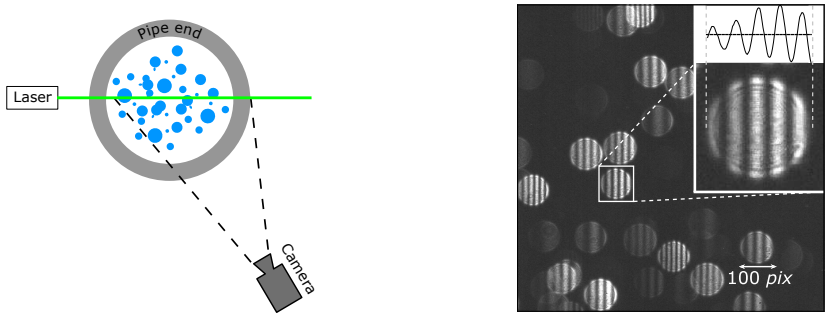

Figure 3.10: Schematic representation of the IPI set-up (left) and a cut-out of a typical image obtained with this method (right). The insert shows the normalized interference pattern obtained from the enlarged droplet image after normalization and the application of a moving average filter.

with a circular mask, having the size of the interference disks. Peaks in the resulting correlation plane are associated with the locations of the droplets. Overlapping parts of the droplet images are removed and the fringe spacing is found from a simple periodogram, obtained using a Fast Fourier Transform of the vertically-averaged disk images. The fringe spacing is subsequently used to calculate the droplet size.

Combination of IPI and SPI

SPI and IPI recordings are carried out subsequently, assuming stationary and reproducible conditions at specific flow settings. The validity of this assumption is verified by repeating experiments on different measurement days. Figure 3.11 shows droplet size distributions obtained from SPI and IPI at the same flow conditions. The overlapping region in droplet diameter, indicated by the dotted lines, is used to combine the two distributions into a single distribution covering the entire droplet size range observed in the experiment. The probability of a droplet ending up in the overlapping range (i.e. $a \leq d_p \leq b$) for the two techniques is:

$$P_{ipi}^{ab} = \frac{N_{ipi}[a \leq d_p \leq b]}{N_{ipi}}, \qquad \text{and} \qquad P_{spi}^{ab} = \frac{N_{spi}[a \leq d_p \leq b]}{N_{spi}}, \tag{3.2}$$

where N_{ipi} and N_{spi} are the number of droplets obtained from IPI and SPI, respectively. Since the distributions from IPI and SPI are subsets of the full droplet size distribution, it holds that $C_1 \cdot N_{ipi} = C_2 \cdot N_{spi} = N_{com}$, where $C_{1/2}$ are constants. Knowing that the probability that a droplet has a diameter between a and b in the combined distribution (P_{com}^{ab}) should match for IPI and SPI, the following conversion is obtained:

$$P_{com}^{ab} = \frac{\frac{1}{C_1} N_{ipi}[a \leq d_p \leq b]}{N_{com}} = \frac{\frac{1}{C_2} N_{spi}[a \leq d_p \leq b]}{N_{com}}. \tag{3.3}$$

The combined drop size distribution then becomes:

$$P_{com} N_{com} = \begin{cases} N_{ipi} & \text{if } d_p \leq b \\ \frac{C_1}{C_2} N_{spi} & \text{if } d_p > b, \end{cases} \qquad \text{with } \frac{C_1}{C_2} = \frac{N_{ipi}[a \leq d_p \leq b]}{N_{spi}[a \leq d_p \leq b]}. \tag{3.4}$$

The result of this operation for one particular case is shown in Figure 3.11. The figure also shows the fitted upper limit log normal (ULLN) distribution, as was also used by e.g. Azzopardi (1997) to describe the droplet size distribution in annular smooth pipe flow. This distribution is fitted to the combined volumetric droplet size distribution and statistical measures regarding the droplets are obtained from the fit.

3.3 TWO-PHASE FLOW IN SMOOTH PIPES

As a reference for the corrugated pipe flow, two-phase flow in a smooth pipe is first assessed. To the knowledge of the authors there is no literature data available for the very low liquid loading used in the presented experiments, and which is relevant in various applications. The liquid volume fraction attained in the experiments is $\phi_l < 2 \times 10^{-4}$. This operating range is particularly relevant for corrugated risers (Belfroid et al., 2013). Furthermore, at the onset

of condensation in heat exchangers or in dry-out conditions, mass fractions in this range will also occur. The present results are compared to data obtained by Belt et al. (2010) and to the data presented in the review paper by Azzopardi (1997), which are both for a higher liquid loading.

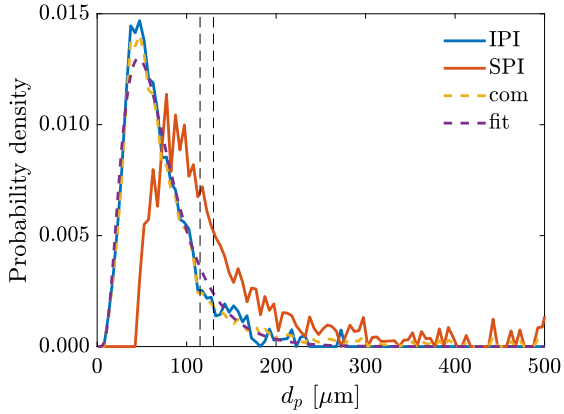

Figure 3.11: Volumetric droplet size distributions obtained from IPI and SPI, and the resulting combined and fitted distribution. The vertical dashed lines indicate the combination region for this particular case.

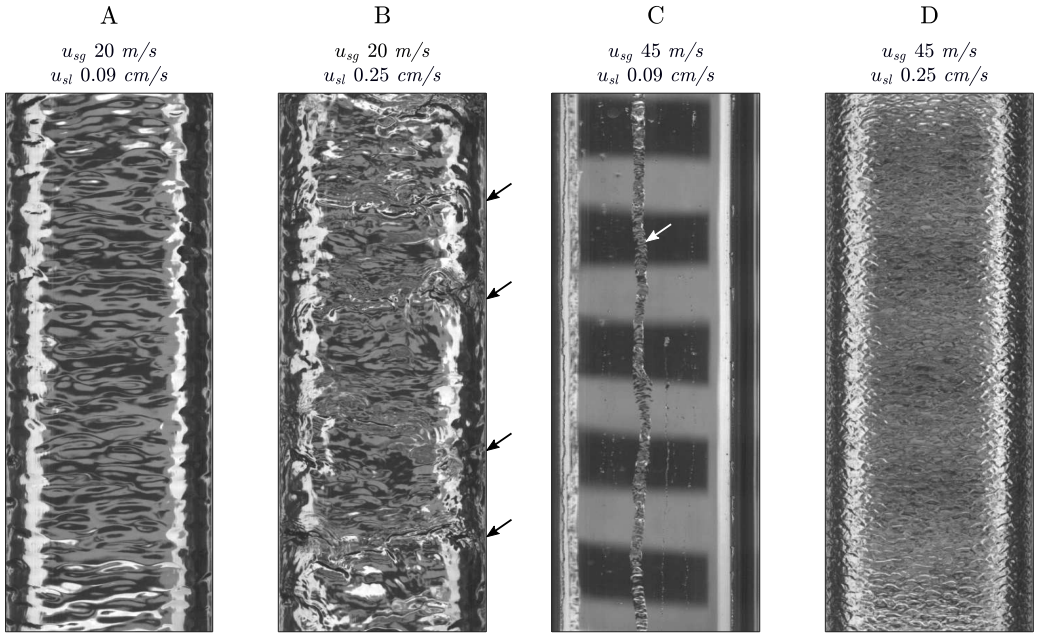

Figure 3.12: Different film flow regimes observed from the high speed video recordings. (A/D) ripples, (B) ripples and disturbance waves, (C) rivulets. The superficial gas and liquid velocities are indicated on top, in *m/s* and *cm/s*, respectively. The black and white bands in the background are used to increase the contrast in the film shadowgraphs. The black arrows indicate the position of disturbance waves in B, whereas the white arrow shows the rivulet observed in C.

The high speed video recordings of the liquid film reveal three different flow patterns: rivulets, regular ripples and disturbance waves. Figure 3.12 shows snapshots of the different flow regimes. For low liquid loading at high gas flow rates the film is not sustained and dry spots appear. This results in the formation of rivulets, transporting all the liquid that is attached to the wall (C in Figure 3.12). The width of the rivulets varies from approximately 0.5 to 5.0 *mm*. The region where rivulets are observed in the data is depicted in Figure 3.13. For most of the parameter space in this study, the film is only covered with ripple waves (A and D in Figure 3.12) which are smaller regular waves, with a limited azimuthal coherence. For high liquid loading at low gas flow velocity, disturbance waves start to appear (B in Figure 3.12). These waves have a significantly larger amplitude than the ripples and travel at a higher velocity. They also show a strong coherence along the circumference of the pipe.

The occurrence of disturbance waves becomes very clear from the time-space diagrams, obtained using the high speed images. These diagrams are obtained from the centerline of the pipe images, in streamwise direction. Figures 3.14a and 3.14c show cases where only ripples are present. Increasing the liquid loading for the same gas flow rate results in the onset of disturbance waves on top of the ripples (Figure 3.14b). They are observed as steep bands with smaller waves. From the slope of these bands the wave speed can be obtained. For the disturbance waves in Figure 3.14b this is approximately 0.45 *m/s*, whereas the ripples in Figure 3.14a travel at a significantly lower velocity (around 0.06 *m/s*). The difference in wave speed is caused by the increased penetration depth of the disturbance waves into the interfacial gas boundary layer. The wave speed is compared to the correlation proposed by Kumar et al. (2002) and more recently revisited by Sawant et al. (2008). This correlation results in an overprediction of the wave speed by a factor 1.7. It is, however, not validated below the onset limit of disturbance waves. Furthermore, Sawant et al. (2008) report that the wave speed is dependent on the pipe diameter, which is smaller than in the current experiments.

From literature it is expected that disturbance waves would not occur in the reported experiments, although a large scatter of the experimental data around the onset boundary of disturbance waves has been observed (Azzopardi, 1997; Sawant et al., 2009). The axial distribution

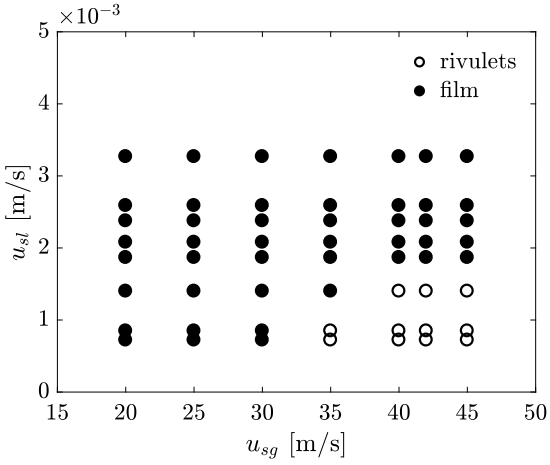

Figure 3.13: Flow map for the experimental parameter space, indicating the regions where a full film and rivulets occur in the smooth pipe.

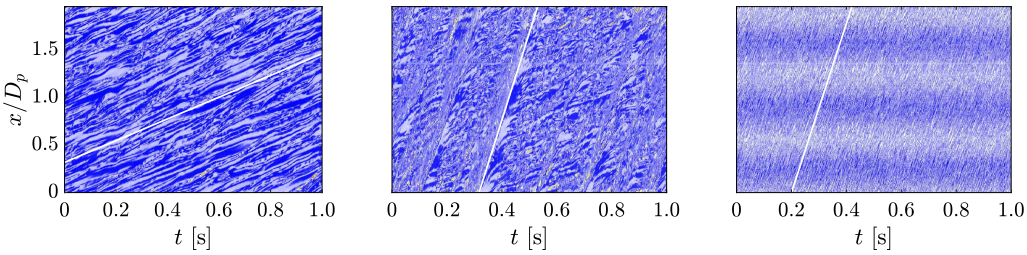

Figure 3.14: Time-space diagrams of the image intensity along the pipe centerline for u_{sg} = 20 (a,b) and 45 *m/s* (c), and u_{sl} = 0.09 (a) and 0.25 *cm/s* (b,c). The white lines indicate the wave speed of the ripple (a,c) and disturbance (b) waves. The letters in the top left corners correspond to the letters used in Figure 3.12.

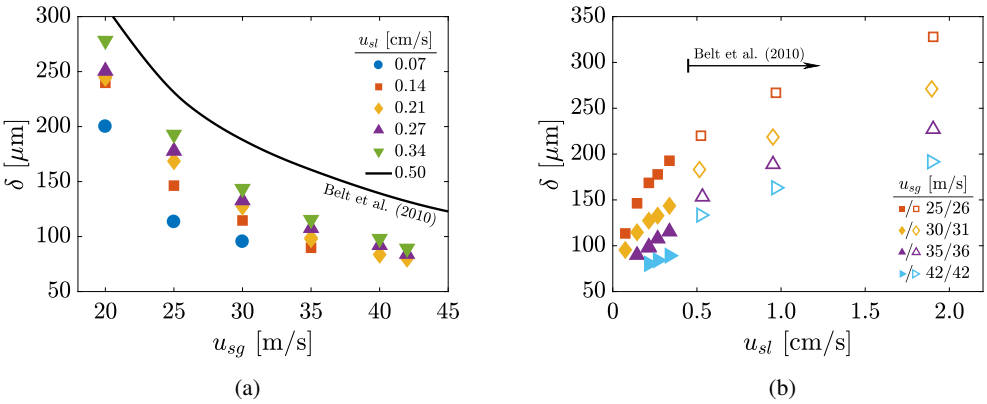

Figure 3.15: Film thickness (δ) as a function of (a) superficial gas velocity and (b) superficial liquid velocity. The solid line in (a) and open symbols in (b) are experimental data by Belt et al. (2010).

of the disturbance waves observed in the high-speed video recordings is highly irregular, indicating operation close to the onset of the waves. Decreasing the liquid loading results in their disappearance, in accordance with the onset boundary found by e.g Sawant et al. (2009). They report that an increase in the superficial gas velocity results in a higher liquid loading required for disturbance waves to occur, which is also observed in our experiments. From the PLIF data it is difficult to distinguish disturbance waves from other waves. Temporal information (wave speed) is required to separate these waves from other high-amplitude bursts (Belt, 2007).

The instantaneous film thickness (δ) can be obtained from the PLIF measurements. Figures 3.15a and 3.15b show the average film thickness with respect to the superficial gas velocity and superficial liquid velocity, respectively. A strong reduction in δ with an increasing gas velocity is observed, which is related to the increased film flow velocity. Although no experimental data is available for the low liquid loading used in the present measurements, the results obtained by e.g. Belt et al. (2010), which are also included in Figure 3.15a, show the same trend. The effect of the liquid loading on δ is also significant, but considerably lower than that of the gas velocity (see Figure 3.15b). The standard deviation of the film thickness, which is a measure

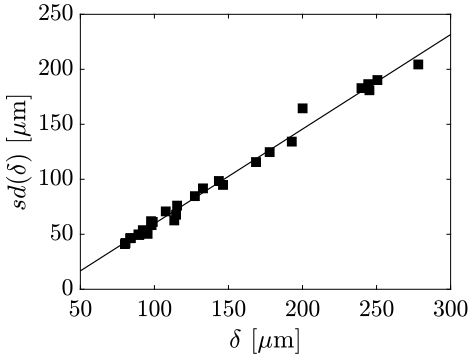

Figure 3.16: Standard deviation of film thickness as a function of the film thickness. The solid line corresponds to a linear fit of all data (with a slope of 0.86)

for the interfacial wave height, shows similar trends with u_{sg} and u_{sl} as the film thickness. Plotting it as a function of the film thickness itself makes all data collapse onto a single straight line, indicating the linear dependence of the wave height on the film thickness, as is also found in literature (Belt et al. 2010, see Figure 3.16).

At the current operating conditions, low liquid entrainment is expected. The absence of disturbance waves in the largest part of the measurement domain corroborates this expectation. Quantitative measures for the amount of entrainment are obtained from film flow rate measurements, as described in Section 3.2.5. The entrainment ratio is defined as $E = \frac{Q_{tot} - Q_{film}}{Q_{tot}}$, in which Q denotes the respective liquid flow rate. The entrainment ratio as a function of the gas flow rate is depicted in Figure 3.17a. An expected increase with the superficial gas flow velocity is observed, originating from the increase of entraining shear forces at the gas-liquid interface. The entrained liquid fraction seems to decrease with increasing liquid loading; the entrainment measurements are, however, somewhat compromised by the evaporation of liquid into the gas flow, effectively changing the total liquid flow rate through the smooth pipe. The actual liquid loading in the measurement section is therefore lower than the liquid loading at the injection point. The evaporation rate is estimated using the corresponding Sherwood number for mass transport in internal pipe flow: $Sh = 0.023 Re_g^{0.83} Sc^{0.44}$ (Gilliland and Sherwood, 1934), where $Sc = \mu_g / \rho_g D_p$ is the Schmidt number. The mass transfer rate is subsequently calculated according to: $\dot{n}_w = k_c A_f \frac{(p_w - p_w^{sat})}{RT}$, where k_c is the mass transfer coefficient ($k_c = ShD_v / L_p$), A_f the interfacial area, p_w the partial pressure of water and R and T the ideal gas constant and the temperature, respectively. Depending on the atmospheric humidity, the liquid flow rate could be corrected using this expression. Unfortunately, no humidity measurements are carried out during the measurements, hence an accurate estimation of the evaporation rate could not be obtained. Using daily meteorological humidity data, an estimate of the evaporation rate is obtained, and is found to be in the same order as the entrainment rate observed in Figure 3.17a. As expected, the actual entrainment will therefore be close to zero. The exact entrainment ratio is, however, not the main purpose of the present study. A qualitative analysis of the effect of corrugations on the entrainment ratio can be performed based on the reported measurements.

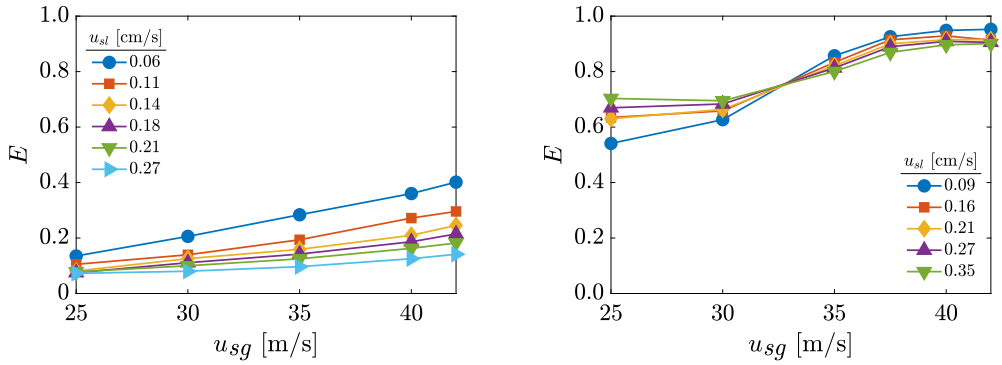

Figure 3.17: Liquid entrainment ratio as a function of the superficial gas velocity u_{sg} for different values of the superficial liquid velocity u_{sl}, in smooth (a) and corrugated pipes (b, geom A).

3.4 TWO-PHASE FLOW IN CORRUGATED PIPES

With the smooth pipe case as a reference, the flow behavior in corrugated pipes is now described. This is done for the corrugation geometries presented in Section 3.2, and for superficial gas and liquid velocities as used in the smooth pipe experiments. As a consequence of the presence of corrugations, the flow regime changes significantly. It is impossible to make the same distinction between a full film and rivulets, as is done for the smooth pipe. Measurements of the liquid entrainment, droplet sizes and the liquid accumulation inside the cavities, however, can provide physical insight into the two-phase flow behavior in corrugated pipes.

Entrainment

The entrainment ratio measured for the corrugated pipe with geometry A is depicted in Figure 3.17b. For higher gas flow rates, almost all liquid is transported as droplets in the gas core of the flow. Evaporation in this pipe is expected to be limited: the large entrainment ratio results in a very short residence time of liquid in the pipe, compared to the smooth pipe. Reducing the superficial gas flow velocity from 42 to 25 *m/s* causes a strong reduction in the amount of liquid entrainment. The entrainment ratio decreases from around 0.95 to 0.60. A critical point occurs for a gas velocity between 30 and 35 *m/s*, where a step in the entrainment is observed. The effect of the liquid flow rate is relatively limited compared to the effect of the gas flow rate. However, the trend in the liquid entrainment before and after the 'step' is opposite. At lower gas flow rates, the lowest entrainment is observed for the lowest liquid flow rate. For $u_{sg} \geq 35\ m/s$, this trend is reversed. Liquid entrainment into the gas core is in all cases considerably higher in the corrugated pipe as compared to the smooth pipe (compare Figures 3.17a and 3.17b).

Droplets in the core

For most of the parameter range, the majority of liquid is transported as droplets in the gas core of the pipe flow. The droplet size distributions obtained from SPI and IPI are combined by matching them around $d_d = 80\ \mu m$, to obtain a single distribution (see Section 3.2.5 for details on the combination of SPI and IPI). Droplet sizing is carried out for a subset of the

parameter range, to observe general trends. Figure 3.18a gives a typical volumetric droplet size distribution (at $u_{sg} = 35\ m/s$ and $u_{sl} = 0.07\ cm/s$). The dashed line shows the fitted ULLN distribution for this case. The Sauter mean diameter ($d_{32} = 6\ V_d/A_d$, with V_d and A_d being the droplet volume and its surface area, respectively) is obtained from the fit, to quantitatively compare the distributions for different flow settings (see Figure 3.18b). The superficial liquid velocity does not affect the droplet size significantly. There is however a strong decrease in droplet size with increasing gas flow rate. Similar trends have been observed for droplets in smooth pipe flow caused by the increased shearing forces exerted on the generated droplets. Droplets observed in the corrugated pipe are significantly larger than expected for a smooth pipe (approximately 30%). Entrainment from corrugations results in larger fragments of liquid being introduced to the gas core, due to the locally increased film thickness inside the cavities. The small pitch length of the investigated geometries results in the presence of larger fragments throughout the entire gas core.

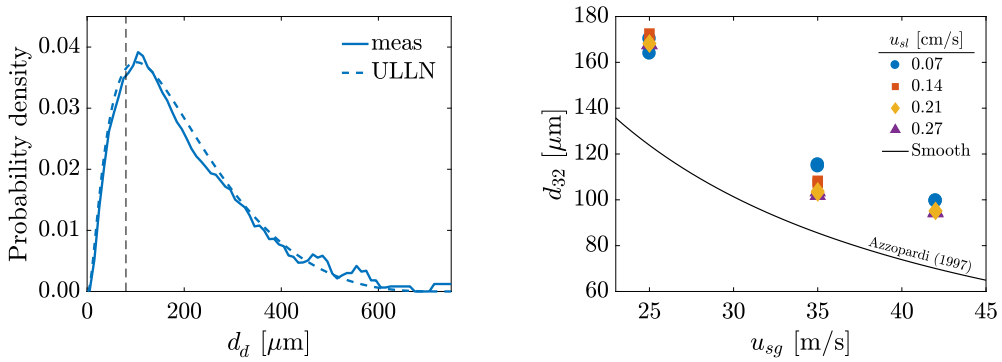

Figure 3.18: (a) Example of a combined droplet size distribution in the corrugated pipe (geometry A) for $u_{sg} = 35\ m/s$ and $u_{sl} = 0.07\ cm/s$, the dashed vertical line indicates the center of the SPI-IPI merging region. (b) Sauter mean diameter of the combined droplet size distributions in a corrugated pipe (geometry A) as a function of the superficial gas flow speed. The solid line indicates a correlation for the droplet size in smooth pipes (Azzopardi, 1997)

Cavity filling

Due to the corrugations and the short pitch length, a continuous liquid film is not formed for most of the parameter space. Liquid accumulates inside the cavities between the corrugations. This liquid accumulation is measured using a PLIF technique (as explained in Section 3.2). The fraction of the cavity volume occupied by liquid (indicated with α) has been used to quantify the amount of liquid in the cavities. α is obtained from the temporally- and spatially-averaged data over all cavities in the field of view. The resulting filling is strongly dependent on the gas flow rate, as is depicted in Figure 3.19a. For $u_{sg} < 30\ m/s$, the cavities are entirely filled up. There exists a liquid film at the wall, skipping over the cavities, essentially reducing the wall roughness experienced by the gas flow. For higher values of u_{sg}, a linear reduction in α is observed. This reduction is mainly manifested at the downstream cavity side. Liquid is removed from the downstream side by the augmented shearing forces exerted by the gas flow. The remaining liquid inside the cavities is dragged towards the upstream cavity edge

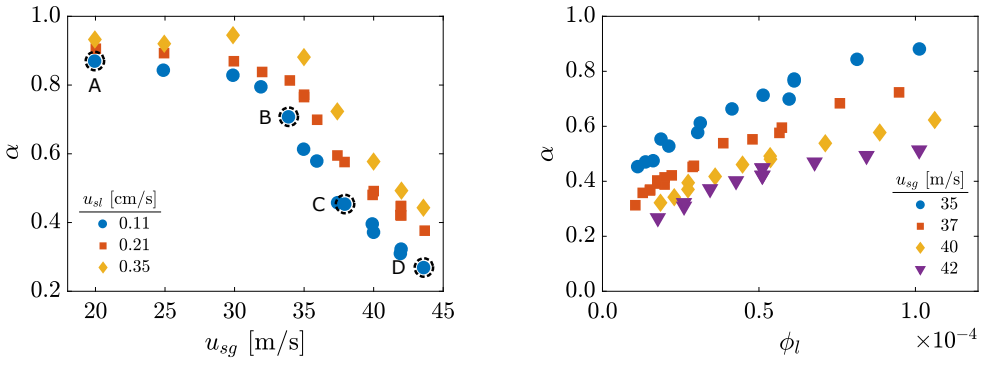

Figure 3.19: Cavity filling as a function of the superficial gas speed u_{sg} (a) and the liquid volume fraction ϕ_l (b). A-D in (a) correspond to the respective filling contours displayed in Figure 3.20.

by the mutual action of gravity and the internal cavity flow. Liquid is re-entrained into the gas core of the flow by the shearing recirculating gas flow above the interface. The effect of the liquid loading is depicted in Figure 3.19b. The filling is plotted against the liquid volume fraction ($\phi_l = Q_l/Q_{l+g}$) to facilitate the comparison for different superficial gas velocities. Filling of the cavities increases with the liquid flow rate, due to the larger liquid influx into the cavities. Typical filling profiles, illustrating the different stages of the liquid filling, are depicted in Figure 3.20.

As shown in Figure 3.17b, there is significant entrainment in the corrugated pipe. Entrained liquid in the core of the pipe is expected to be spatially isolated from the cavities at the outer radius of the pipe. Mainly liquid transported close to the pipe wall interacts with the internal

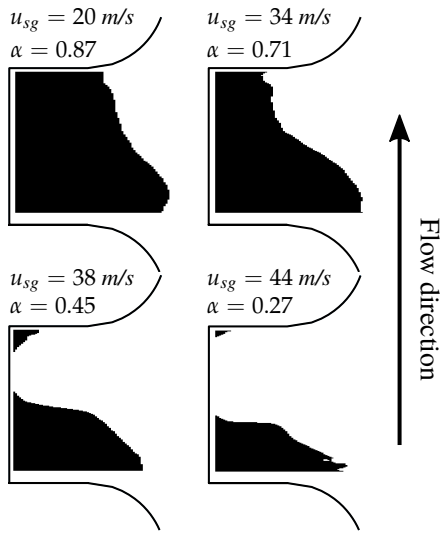

Figure 3.20: Liquid cavity filling profile, measured with the PLIF method described in Section 3.2, for the four different cases indicated in Figure 3.19a. Flow is from bottom to top and dark regions are regions of liquid accumulation. $u_{sl} = 0.11$ *cm/s* for all cases.

cavity flow, affecting the liquid cavity filling. Therefore, the liquid entrainment ratio, averaged for different liquid flow rates, is used to correct the superficial liquid velocity. This results in a superficial liquid film velocity (defined as $u_{sf} = (1 - E)u_{sl}$). Plotting the filling α as a function of this u_{sf} causes the data for the various gas flow rates to collapse onto a single line (see Figure 3.21). This indicates that the effect of the gas flow rate on the filling is mainly caused by an increase in entrainment for increasing u_{sg}. It, therefore, implies that the entrained liquid does not interact with the internal cavity flow and hence, does not result in additional liquid being trapped in the cavities.

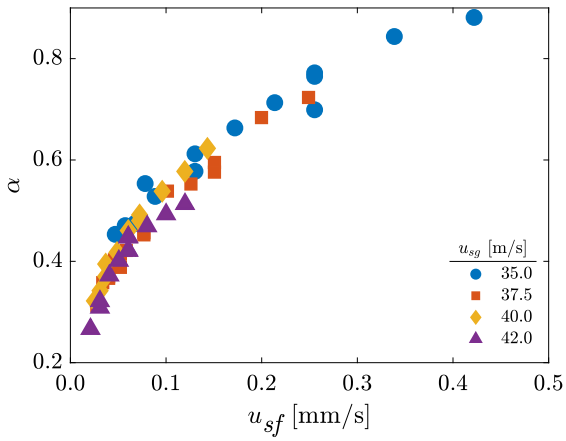

Figure 3.21: Liquid filling fraction α as a function of the superficial liquid film velocity (u_{sf}) for different values of superficial gas velocity (u_{sg}).

Cavity geometry and liquid properties

To assess the effect of cavity size and properties of the injected liquid on the two-phase flow behavior, additional experiments are carried out using a corrugated pipe with geometry B (see Table 3.1) and/or with mono-ethylene glycol (MEG) instead of water. Geometry B is similar to geometry A, but the cavity depth and length are enlarged by 50%. MEG is approximately 19 times more viscous than water at atmospheric conditions, whereas the surface tension is significantly reduced (from 72 *mN/m* for water to 48 *mN/m* for MEG, see Lide 1994). Attempts were made to use aqueous glycerol solutions to keep the surface tension change limited. However, water evaporation from the solution might cause the liquid properties to change over the length of the pipe, troubling the results.

3.5 DISCUSSION

For the corrugated pipe with geometry B, the entrainment ratio approaches one, irrespective of the gas flow rate and liquid loading (Figure 3.22b). The step in the entrainment ratio, observed for geometry A, does not occur for geometry B, within the current parameter space. This is related to the filling fraction α, which never attains values above 0.6 for this geometry, even for lower gas flow rates (as is depicted in Figure 3.23b). The filling shows the same steady increase with increasing liquid loading, but the upper limit is never reached, and it probably occurs at

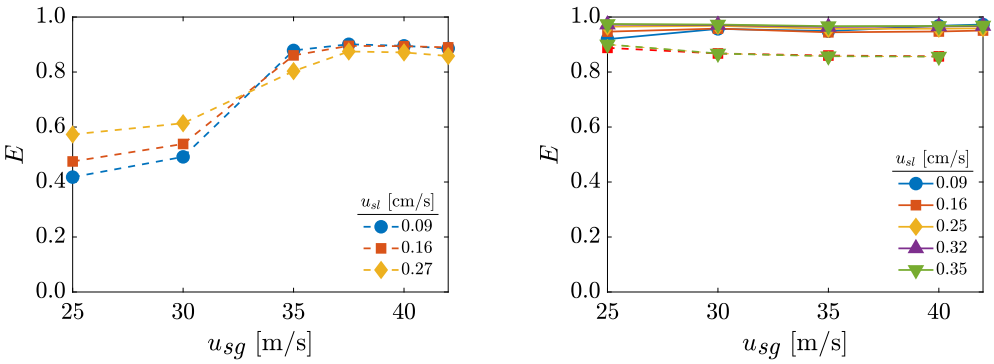

(a) (b)

Figure 3.22: Liquid entrainment as a function of the superficial gas velocity in a corrugated pipe, for different liquid loadings. Pipe with geometry A (a) and geometry B (b). Solid lines are for water, dashed lines for MEG. Results for water injection in geometry A are depicted in Figure 3.17b.

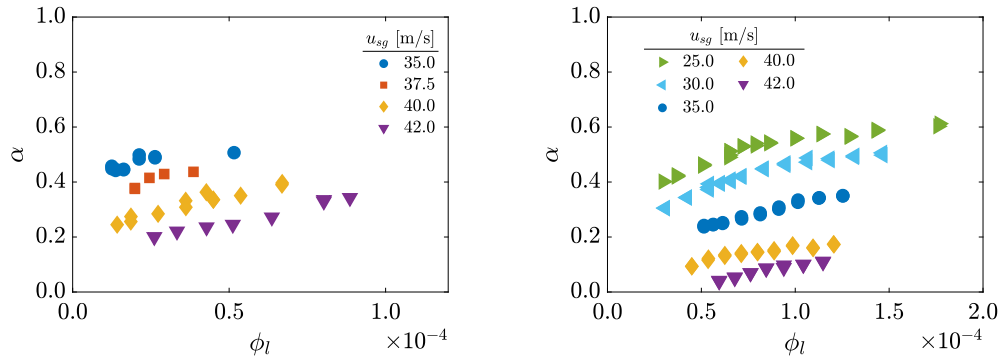

(a) (b)

Figure 3.23: Cavity filling as a function of liquid volume fraction ϕ_l, for different superficial gas flow speeds. (a) Filling for MEG injection in geometry A, and (b) for water injection in geometry B.

a higher liquid loading. It was shown for geometry A, that at total cavity filling ($\alpha \rightarrow 1$) the entrainment significantly reduces. For lower filling ratios, nearly full entrainment is exhibited ($E \rightarrow 1$). Similar principles hold when injecting MEG instead of water (Figures 3.22a and 3.23a). The absolute values of the entrainment ratio for MEG are slightly lower compared to water, for both corrugation geometries. Also the filling ratio is lower. The trends in both filling and entrainment are similar for water and MEG. The large increase in viscosity when switching from water to MEG does not have a strong effect on either filling or entrainment.

The entrainment of liquid in two-phase corrugated pipe flow is strongly related to the cavity filling. The liquid entrainment ratio E sharply increases when liquid is removed from the individual corrugations. The recirculating gas flow inside the cavities drags liquid back into the gas core (as depicted in Figure 3.24). It is assumed that this process is governed by shearing-off of waves at the gas liquid interface inside the cavities. Due to the relatively high gas flow velocity and the locally increased film thickness as a consequence of the presence of the cavities, it is safe to assume that indeed the ligament break-up mechanism (see Figure 3.1) is dominant. There is a balance between drag force, exerted by the shearing gas flow, and the retaining force due to surface tension. Whenever the drag force on the interfacial wave crests exceeds the retaining force ($F_d \geq F_\sigma$), liquid packets are removed from the interface and entrained in the gas flow. The drag force is given by: $F_d = C_d \lambda_w h_w \rho_g u_w^2/2$, with the drag coefficient C_d, the wavelength λ_w, the wave height h_w and the relative velocity difference between the liquid and gas flow u_w. The retaining surface tension force is given by $F_\sigma = C_s \lambda_w \sigma$, with C_s depending on the wave shape. Using this force balance as a starting point, Ishii and Grolmes (1975) derived the following entrainment criterion:

$$\frac{\mu_l u_g}{\sigma}\sqrt{\frac{\rho_g}{\rho_l}} \geq 11.78 N_\mu^{0.8} Re_l^{-1.3}, \tag{3.5}$$

where N_μ is the viscosity number, which will be defined in Equation 3.6. In a later study, Ishii and Mishima (1989) derived a correlation for the entrained fraction of liquid, based on the previously postulated onset criterion. Assuming that all excess liquid (above the critical entrainment limit from Eq. 3.5) is actually entrained, they found that the entrainment ratio E is a function of the liquid Reynolds number and the Weber number $\left(E = f(We^{1.25} Re_l^{0.25})\right)$.

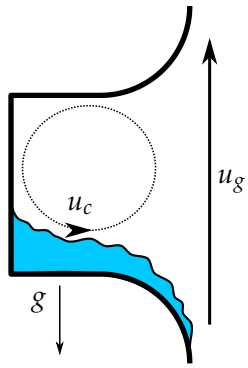

Figure 3.24: Schematic of the internal cavity flow, removing liquid from within the corrugation.

The Weber number $\left(We = \frac{\rho_g u_c^2 L}{\sigma}\right)$ indicates the balance between the retaining forces (surface tension) and disturbing forces (shear at the gas/liquid interface). The cavity recirculation velocity is defines as $u_c = u_{sg}/4$, which is representative for a cavity flow (Koschatzky et al., 2011). The liquid Reynolds number $\left(Re_l = \frac{\rho_l u_{sl} L}{\mu_l}\right)$ is a measure for the effect of the viscous forces inside the liquid. The critical Re_l for annular gas-liquid flow is not reached in most of the current experiments, due to the very low liquid loading. Therefore, the entrainment in the smooth pipe flow is very low (see Figure 3.17a). This is caused by the thin liquid film, entirely submerged in the interfacial gas boundary layer (Ishii and Grolmes, 1975). The cavities in the corrugated pipe, however, cause local liquid accumulation, resulting in a significantly increased film thickness from which entrainment will occur. The dependency on Re_l is therefore different in corrugated pipe flow. In smooth pipes, the entrainment is positively correlated to the liquid Reynolds number; thicker films result in more entrainment. In corrugated pipes, however, entrainment is related to liquid accumulation in the cavities. A larger liquid Reynolds number (indicating more liquid being transported) leads to an increase in cavity filling, which reduces the entrainment. To arrive at Equation 3.5, it was assumed that $N_\mu^{0.8} \approx 3N_\mu$. The assumption holds for low viscosity liquids, typically when $N_\mu < 0.01$. For MEG, used in the present study, it is not valid, and $N_\mu^{0.8}$ is used instead of $3N_\mu$. The viscosity number N_μ is a fluid property, and is defined as:

$$N_\mu = \frac{\mu_l}{\left(\rho_l \sigma \sqrt{\frac{\sigma}{g(\rho_l - \rho_g)}}\right)^{1/2}}. \tag{3.6}$$

Assuming that the gas-filled part of the cavity volume $(1-\alpha)$ is related to the amount of liquid entrainment (E) from the cavity, it can be approximated by:

$$(1-\alpha) = f(We^{1.25} Re_l^n). \tag{3.7}$$

The relevant length scales for the Weber and Reynolds number are associated with the cavity filling. The length scale in the definition of We is taken as half the empty cavity size $(L = 1/2(1-\alpha)L_c)$, whereas for Re_l, it is taken as $L = \alpha L_c$. Applying these definitions to the data acquired in the reported experiments, $n = -0.25$ gives the best collapse of all data points (as presented in Figure 3.25a). There is still some scatter of the data observed in the figure. As was mentioned before, instead of scaling with the total liquid flow rate, a better agreement is found by using the superficial film velocity u_{sf}. Figure 3.25b shows the filling as a function of We and Re_f $(= \frac{\rho_l u_{sf} L}{\mu_l})$. A close collapse of all the data is obtained. It should be noted that the liquid viscosity has no effect on the filling, when this scaling is applied. This is also found in the present work. The behavior of the liquid film is completely dominated by surface tension and the shearing gas force. According to Ishii and Grolmes (1975), this holds in the low viscosity number regime (where $N_\mu \leq \frac{1}{15}$).

In the low liquid filling regime, entrainment from within the corrugations augments the total entrainment ratio. Apart from liquid entrainment originating from within the cavities, a second entrainment mechanism seems to occur simultaneously. From the entrainment measurements for geometry A (depicted in Figure 3.17b) it appears that even for entirely liquid-filled cavities (at the lower u_{sg} range), around 60% of the total liquid flow rate is entrained. This can not be

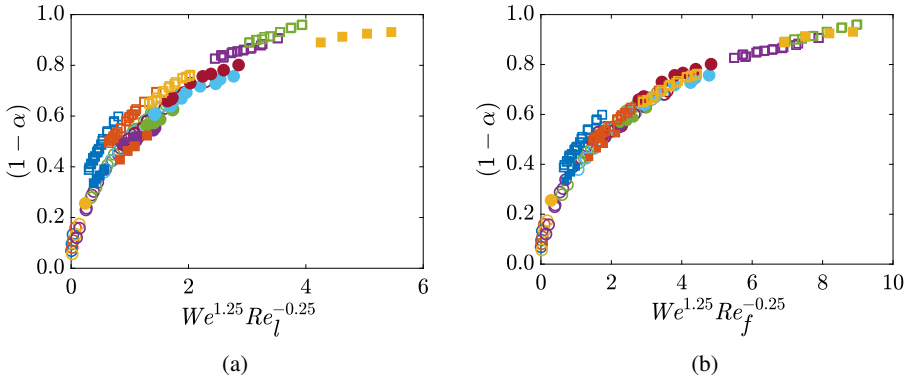

Figure 3.25: Gas-filled part of the cavity $(1-\alpha)$ as a function of the Weber number and the Reynolds number based on the total liquid flow rate (a) and the film flow rate (b).

caused by the previously described entrainment from within the cavity. It is expected that the corrugations decrease the stability of the film and increase its wavy structure. The standard entrainment mechanisms start to dominate , where entrainment is again a function of the liquid Reynolds number and the Weber number ($E = f\left(We^{1.25}Re_l^{0.25}\right)$), as was found by Ishii and Mishima (1989). The typical entrainment ratio for water exceeds that for MEG under the same conditions. Due to the significantly higher viscosity for MEG, compared to water, the liquid Reynolds number decreases and hence, the entrainment is expected to decrease. The lower liquid Reynolds number indicates a lower film thickness at the same flow conditions, penetrating less far into the interfacial gas boundary layer. The shearing gas velocity at the interface is lower, hence the entraining forces decrease, leading to a lower entrainment ratio. For the lower filling cases, entrainment from within the cavities and from the separating ribs will co-exist. However, the interplay of these two entrainment mechanisms is still unclear.

All reported experiments are conducted in upward vertical flow direction. It is anticipated that the direction of gravity will have a strong effect on the obtained results. In Chapter 2 it is shown that the flow direction with respect to the gravity has significant consequences for the liquid cavity filling behavior (van Eckeveld et al., 2017). The liquid filling ratio is considerably higher for downward directed flow. Assuming a similar relation between cavity filling and entrainment to hold in downward flows, the liquid entrainment is expected to be reduced (see Figures 3.17b and 3.19a).

3.6 CONCLUSIONS

Two-phase flow experiments are carried out in a smooth pipe and in corrugated pipes to assess the effect of the presence of corrugations on the liquid distribution in vertical pipe flow. Film thickness measurements are performed using a novel implementation of *planar laser-induced fluorescence* (PLIF). Shadows are added to the incoming laser sheet, where they appear as dark lines. The deviation of these lines at the gas-liquid interface is used to identify and remove large reflections in the PLIF measurements. Gas and liquid phase Reynolds numbers (based on the pipe diameter) are $Re_g = O(10^5)$ and $Re_l < 250$ for the presented experiments. At these conditions, liquid entrainment is not expected to be significant in smooth pipes. The

entrainment ratio (corrected for evaporation) is close to zero. Only for a very limited range of flow parameters, the onset of disturbance waves is observed, which are widely accepted as the main source of liquid entrainment. The film thickness is in the order of 100 μm, and the observed trends with the changing superficial gas and liquid velocities are confirmed by other experiments (with higher liquid loading), reported in literature. For very low superficial liquid velocities at high superficial gas velocities the annular film breaks up and liquid is transported as rivulets along the pipe wall.

Two-phase flow in corrugated pipes shows a very different behavior compared to smooth pipes, at the same flow conditions. Droplet sizing in the corrugated pipe reveals that considerably larger liquid fragments are transported in the gas core of the pipe, compared to the expected droplet distribution in smooth pipes. This is most likely caused by the locally (at the location of the cavities) increased film thickness, resulting in larger entrained fragments. The liquid entrainment ratio is significantly higher in corrugated pipes than in smooth pipes. Liquid is found to accumulate in the axisymmetric cavities along the pipe wall, and the entrainment strongly correlates with the liquid-filling ratio (α). A sharp increase in the liquid entrainment ratio is observed when the filling is decreased; for totally liquid-filled cavities the entrainment is significantly lower than for partially filled cavities. This shows that the internal gas flow inside the cavity causes additional entrainment. The cavity filling α is therefore an important parameter when it comes to entrainment in these corrugated pipes. It is found to scale with the Weber and liquid Reynolds number, based on the film flow rate: the gas filled cavity volume $(1-\alpha)$ scales with $(We^{1.25}Re_f^{-0.25})$. The scaling with the Weber number is similar to the scaling for entrainment in smooth pipes. The liquid Reynolds number scaling, however, is opposite. An increase in Re_f in smooth pipes leads to an increased entrainment. For partially filled cavities in corrugated pipes the filling ratio and, hence, the entrainment decreases with increasing Re_f.

It is shown in this work that the liquid entrainment ratio in corrugated pipes is strongly dependent on the amount of liquid accumulating in the cavities of a corrugated pipe. Future work should assess this relation for a broader range of corrugation geometries and further investigate the influence of the direction of gravity on the obtained results.

4

SILENCING CORRUGATED PIPES BY LIQUID ADDITION - IDENTIFICATION OF THE MECHANISMS BEHIND WHISTLING MITIGATION

Severe vibrations and sound production can occur in dry gas flow through corrugated pipes. The addition of very small amounts of liquid to the dry gas flow potentially mitigates these flow-induced vibrations (FIVs) and noise. The different mechanisms behind this whistling mitigation are studied in this chapter, where acoustic measurements are combined with flow visualization and droplet sizing. Different corrugation geometries are studied. It is shown that noise mitigation mainly occurs through a geometric alteration of the cavity mouth, resulting in a reduced acoustic source strength. Additional acoustic damping as a consequence of the presence of droplets has a very limited contribution to the mitigation of FIVs. A non-axisymmetric filling of the cavities of a corrugated pipe with liquid is more effective in reducing the acoustic output, compared to an axisymmetric filling. The liquid viscosity has a very limited effect on the achieved noise mitigation. To predict the acoustic source strength of a particular cavity geometry a numerical method is developed, based on URANS simulations combined with Howe's energy corollary. An energy balance method is applied to obtain the acoustic source strength from experiments. The whistling frequencies are accurately predicted with the simulations, but the acoustic source strength is over-predicted by a factor 2. Trends in the source strength obtained from simulations, however, closely resemble the experimentally obtained results. Only for very shallow cavities clear differences are found.

This chapter is submitted to the *Journal of Sound and Vibration*.

4.1 INTRODUCTION

Flow-induced vibrations occur in various applications, ranging from wind-turbine noise to building acoustics. One case extensively studied is the aerodynamic noise production from flow over a cavity or a range of cavities. An application that is of particular interest in many fields, and closely related to cavity flow noise, is whistling in corrugated pipes. Corrugated pipes are widely used when a flexible connection is required to transport a gas or liquid from one place to another. The corrugations provide the required flexibility and prevent the pipe from collapsing. The interaction of the internal gas flow with the corrugated pipe wall, which is essentially a sequence of individual axisymmetric cavities, causes the formation of shear layers over the cavities. These shear layers separate the internal cavity flow from the bulk flow through the pipe. Under certain conditions, they can act as a source of sound. High amplitude acoustic noise is generated, which causes vibrations that can seriously damage system. It is therefore of cardinal importance to understand the whistling phenomenon in corrugated pipe flow and to find ways to mitigate the vibrations that occur. In this study, the mitigation of whistling by liquid addition is assessed. Previous studies show that the addition of liquid to a corrugated pipe flow potentially mitigates whistling entirely (Belfroid et al., 2013; van Eckeveld et al., 2017). The effect of filling the cavities with liquid and the effect of the presence of droplets in the pipe are investigated experimentally using a combination of acoustic measurements, droplet sizing, and two-phase visualization techniques. Dry whistling experiments are carried out with several corrugation geometries, inspired by the experimental results. Whistling mitigation by liquid addition is assessed in different geometries and with two different types of liquid (water and mono-ethylene glycol). The acoustic output is subsequently modeled using a combination of 2D-axisymmetric URANS simulations with Howe's theory of vortex sound, to get more insight in the spatial and temporal distribution of the acoustic production and absorption regions in the cavities. This provides an increased understanding of the specific geometrical properties that are important for whistling in corrugated pipes.

4.1.1 WHISTLING IN CORRUGATED PIPES

Noise production in cavity flows is studied widely in literature. A good review was prodived by Rockwell and Naudascher already in the 1970s (Rockwell and Naudascher, 1978), and more recent contributions are found in the work by Gloerfelt (2009). The acoustics observed in cavity flows originate from the unsteady shear layer, separating the low speed inner cavity flow from the higher speed flow over the cavity. In some conditions, the shear layer can become unstable, resulting in the formation of discrete vortices (Michalke, 1965). The acoustic amplitude is greatly enhanced if it is strengthened by a feedback mechanism. This can be of acoustic and/or hydrodynamic nature. Hydrodynamic feedback originates from a Biot-Savart type of interaction, caused by the vortices in the shear layer. The induced velocity influences the undisturbed shear layer at the upstream separation point, initiating vortex shedding. For high Mach number flows, the pressure waves generated at the downstream cavity edge can also interact with the upstream shear layer, and cause the formation of new vortices. This interaction, which is of an acoustic nature, takes place within the cavity. It only exists for acoustically non-compact cavities, where the cavity length is at least of the order of the acoustic wavelength. For low Mach number applications this is generally not the case. An acoustic feedback can, however, still exist on a larger scale. When an acoustic resonance is excited by

the shear-layer vortices, the acoustics perturbation can synchronize vortex shedding. Examples of these interactions are Helmholtz resonators, where the cavity opening is smaller than the cavity length, and corrugated pipes, where a resonance in the pipe system can occur.

The interaction of vortical structures with the acoustic field in a corrugated pipe is the source of sound (Howe, 2003), which is of dipole nature. Binnie (1961) found that the corrugations slightly alter the effective speed of sound (c_{eff}) in the pipe. They provide an additional reactance to the acoustic field, reducing the speed of sound. Elliott (2005) derived an expression for this modified speed of sound:

$$c_{eff} = \frac{c_0}{\sqrt{1 + V_c/(A_p P_c)}}, \tag{4.1}$$

where V_c is the cavity volume, A_p the inner cross-sectional area of the pipe and P_c the pitch length of the corrugations (see Figure 4.4 for a definition sketch). c_0 is the sonic velocity at standard conditions. The effective speed of sound, together with the pipe length, determines the resonance frequencies of the entire pipe system, according to:

$$f_r = \frac{n_{ac} c_{eff}}{2L_p}, \tag{4.2}$$

where L_p is the pipe length and $n_{ac} = 1, 2, 3, ...$ the mode number. This only holds for axial pipe modes, where the frequency is below the cut-off frequency of the pipe (Rienstra, 2015). All transverse pipe modes are evanescent below the cut-off frequency. When whistling occurs, the shedding frequency of the vortices in the cavity mouth locks with one of the acoustic resonance modes of the pipe system.

Whistling in cavity flows is associated with a Strouhal number, defined as (Bruggeman et al., 1991)

$$Sr_c = \frac{f_w L}{U_b} = 0.13 + 0.40 n_h. \tag{4.3}$$

In this equation, f_w is the whistling frequency, L a typical cavity length scale, and U_b the bulk velocity through the pipe. n_h is the hydrodynamic mode number, indicating the number of vortices simultaneously present in the cavity mouth. It is shown that the first hydrodynamic mode ($n_h = 0$) is rather weak (Martínez-Lera et al., 2009) and that the second hydrodynamic mode is dominant ($n_h = 1$). In practice, instead of the generally unknown vortex convection velocity, the whistling Strouhal number is expressed in terms of the bulk velocity through the pipe: $Sr = \frac{f_w L}{U_b}$. Nakiboğlu et al. (2010) found that for corrugations with rounded edges, a modified cavity length ($L = L_c + r_{up}$, with L_c being the cavity length and r_{up} the upstream cavity edge radius) is the best choice as characteristic length scale. The typical whistling Strouhal number range obtained by Nakiboğlu et al. (2010) using this definition is $0.32 \leq Sr \leq 0.42$. Since the bulk gas flow velocity is used in the definition of the Strouhal number, it is expected that its value is significantly lower than unity, as a consequence of the difference between the bulk velocity and the vortex convection velocity in the cavity mouth.

The onset velocity, i.e. the lowest velocity at which whistling occurs, has been subject of many studies. Initially it was thought to be related to a minimum required turbulence level in the pipe (Crawford, 1974; Cadwell, 1994). This was later contradicted, when it was found that

the relative increase of acoustic losses at lower flow speeds caused the absence of whistling below the onset velocity. The acoustic production is in this case lower than the acoustic losses in the pipe, preventing whistling to occur (Rudenko et al., 2013). After onset, the whistling frequency shows a global characteristic linear increase with flow velocity, corresponding to a fixed Strouhal number. The whistling frequency locks with successive acoustic resonance modes of the pipe, resulting in a step-wise increase of the frequency. Upon increasing the flow velocity the frequency jumps to the next frequency plateau. In a long pipe, there is a very large number of possible acoustic modes below the cut-off frequency of the pipe. Which of these modes are excited depends on the combination of pipe length and the acoustic boundary conditions of the pipe system (Goyder, 2010).

In this work we limit ourselves to acoustically compact cavities, excluding cavities in which an internal acoustic feedback mechanism prevails. For cavities with a depth over length ratio larger than one half ($H_c/L_c > \frac{1}{2}$) the effect of the depth is rather limited (Nakiboğlu et al., 2012a). There is a slight influence on the whistling frequency, but the amplitude is largely unaffected. Below this threshold, the whistling amplitude decreases significantly due to the increased interaction between the shear layer and the cavity bottom. The effect of the cavity length relative to the incoming boundary layer thickness is studied widely for flat plate cavities (e.g. by Gharib and Roshko, 1987). They showed that the ratio of shear layer length (or cavity length) over incoming boundary layer momentum thickness (L_c/θ) is a crucial parameter, determining whether or not a shear layer becomes unstable and exhibits discrete vortex shedding. For $L_c/\theta > 80$ vortex shedding was observed, in what they called the 'shear layer mode'. Although well established for flat plate cavities, for corrugated pipes this theory has not been verified. However, due to regrowth of the boundary layer over the plateaus separating the corrugations, a similar mechanism is expected in corrugated pipes (Belfroid et al., 2007). The influence of the confinement ratio (i.e. the ratio of pipe diameter to cavity length) is mainly through an alteration of the velocity profile in the pipe (Nakiboğlu et al., 2011). A very strong effect of rounding the upstream cavity edge was observed by several authors (Binnie, 1961; Bruggeman et al., 1991; Dequand et al., 2003; Nakiboğlu et al., 2010; Bolduc et al., 2013). The whistling amplitude strongly increases when switching from a sharp to a rounded upstream edge. This is due to the vortex-acoustic field interaction at the upstream edge. Acoustic absorption mainly occurs at the upstream edge, and its amplitude decreases when the local (potential) acoustic velocity field at the flow separation point is reduced. The effect of the downstream edge geometry is smaller, because the vortex is less localized once it arrives at this edge.

4.1.2 MODELING OF WHISTLING

It is not straightforward to model whistling in corrugated pipes, due to the non-linearity of the phenomenon. Several models are developed to predict the whistling *frequencies* of corrugated systems, for example by Binnie (1961), Elliott (2005) and Tonon et al. (2010). These models are rather successful. The whistling *amplitude*, however, is more difficult to predict. Several semi-emperical models exist (for example the energy balance model by Tonon et al., 2010). These models do require experimental or numerical data on the strength of the acoustic source along the pipe, and obtain the acoustic amplitude by estimating the losses. Rudenko et al. (2013) uses a similar approach to obtain the onset velocity of whistling in corrugated pipes. However, no accurate methods exist that can predict the acoustic amplitude generated by the

flow through a corrugated pipe. Experiments or numerical simulations are required to assess the acoustic source power of a certain geometry. Simulations carried out for corrugated pipe flow are mainly restricted to resolving the flow field, and not the acoustics. The large disparity in typical scales for the acoustics and the hydrodynamics make fully-resolved simulations very expensive. Moreover, reflections of acoustic waves at the boundary conditions complicate the calculations, and high-order methods are required to minimize dispersion and dissipation. These *direct noise computations* (DNC) have been carried out for single cavity flows (Marsden et al., 2003), but they are not feasible in corrugated pipe flow at higher Reynolds numbers. Numerical modeling is usually restricted to a decoupled analysis of the flow and the acoustics, using acoustic analogies in combination with *Reynolds-averaged Navier-Stokes simulations* (RANS), or large eddy simulations (LES, see Martínez-Lera et al., 2009; Nakiboğlu et al., 2012a; Rajavel and Prasad, 2013).

4.1.3 WHISTLING MITIGATION

Different methods to mitigate whistling in corrugated pipes are proposed in literature. The first study concerning whistling mitigation was carried out by Petrie and Huntley (1980). They found that obstructions in the region of flow separation could strongly reduce the acoustic amplitude. Other authors studied the use of active flow control by means of small speakers in a single corrugation (Gharib, 1993), which did not prove to be very effective. Both methods are not applicable in long corrugated pipes. The addition of acoustic damping to the pipe system by means of smooth pipe sections (Rudenko et al., 2013) or acoustics dampers is also difficult to implement in many industrial applications. Especially in existing installations, there is a need for an ad-hoc solution which does not require the expensive replacement of entire piping systems.

Liquid addition to the dry gas flow in corrugated pipes provides such a solution. It is shown that the presence of liquid, even at very low liquid fractions, has the potential to mitigate whistling completely (Belfroid et al., 2013; Golliard et al., 2013a; van Eckeveld et al., 2017). The studies by Belfroid et al. (2013) and Golliard et al. (2013a) focused on horizontal pipes, with a limited number of experiments and field cases in vertical pipes. Very small liquid volume fractions ($O\,(10^{-4})$) were sufficient to remove whistling entirely. The authors proposed several mechanisms causing this whistling mitigation: filling of the cavities with liquid, additional acoustic damping due to the presence of droplets, and a reduction of the acoustic source strength due to shear layer disruption or boundary layer thickening. In Chapter 2 experiments on vertically oriented corrugated pipes in upward and downward flow direction are described (see also van Eckeveld et al. (2017)). They showed that filling of the corrugations with liquid is an important factor determining the reduction of the whistling amplitude in corrugated pipes. Several open questions, however, still remain. The effect of different corrugation geometries on the sound mitigation by liquid addition is unknown, and the contribution of acoustic damping due to the presence of droplets has to be quantified. Furthermore, it is unclear which specific geometrical changes to the cavities cause the whistling mitigation, and what effect changes to the properties (e.g. viscosity and surface tension) of the used liquid have.

4.1.4 OBJECTIVE AND OUTLINE

The work described in this chapter is carried out to increase the understanding of whistling mitigation in corrugated pipes by liquid addition. The mechanisms behind whistling mitigation are further studied. This is done using a combination of experiments and numerical simulations. Experiments are carried to study two-phase whistling behavior and the effect of the corrugation geometry and liquid properties. Numerics are used to verify these results using single phase simulations, and to assess the specific geometrical aspects of the corrugations responsible for sound production. Section 4.2 discusses the theory required for this work. It introduces the energy balance model and the effect of liquid addition on the acoustics. Subsequently, in Section 4.3, the experimental setup and measurement techniques are explained. The dry whistling behavior obtained from the experiments for different corrugated pipes is treated in Section 4.4, followed by the experimental results in two-phase conditions (Section 4.5). The numerical modeling of sound sources in corrugated pipe flow is discussed in Section 4.6, where the method is explained and numerical results are compared to experiments. Finally, in Section 4.7 the experimental and the numerical results are discussed, and conclusions and future perspectives are provided in Section 4.8.

4.2 THEORY

The relevant theory is treated in this section. First the *energy balance model* (EBM) is introduced, which is used to estimate the acoustic losses in a corrugated pipe. Subsequently, acoustic damping by a dispersed liquid phase is described, followed by Howe's theory of vortex sound. This theory is required to obtain the acoustic source strength from simulations.

4.2.1 ACOUSTIC ENERGY BALANCE

An energy balance model is used to estimate the whistling amplitude in corrugated pipes. This approach, previously described by Tonon et al. (2010) and Nakiboğlu et al. (2011), is employed to predict the whistling amplitude when the acoustic source strength is known, either from experiments or simulations. The underlying principle is that, when a corrugated pipe exhibits steady whistling, there exists a balance between production and absorption of acoustic energy, determining the whistling amplitude for a specific frequency. The time-averaged acoustic source power along the pipe (originating from the unstable shear layers) is matched by the time-averaged acoustic losses in the entire flow system. The acoustic losses can be divided into viscothermal losses (P_{vt}, due to friction and heat-transfer), radiation losses (P_{rad}) at the entrance and exit of the pipe, and convection losses (P_{conv}) at the outlet of the pipe. Convection losses can also occur at the pipe inlet, depending on the inlet geometry. When this geometry causes flow separation inside the pipe, the acoustic absorption is increased.

Under whistling conditions, the acoustic losses balance the acoustic energy that is generated by the interaction of the flow with the acoustic field in the pipe, per unit time, resulting in a power balance:

$$\langle P_{source} \rangle = \langle P_{vt} \rangle + \langle P_{conv} \rangle + \langle P_{rad} \rangle. \tag{4.4}$$

As the acoustic losses are frequency dependent, the whistling frequency should be known to estimate the source power using this energy balance. This model predicts whether or not a whistling mode can exist for a given frequency and flow rate. Close to the onset of whistling it is rather inaccurate as a consequence of the different acoustic amplitude dependency of the source power. The model is applicable in whistling conditions, when the individual terms can be estimated. In the following, each of the terms in Equation 4.4 will be derived. First the acoustic sources are treated (the left hand side of the equation), followed by the losses (the right hand side).

Sources

The behavior of the acoustic sources largely depends on the fluctuation amplitude of the acoustic waves that are generated. Three regimes are distinguished, determined by the ratio of the acoustic perturbation amplitude over the bulk gas flow speed $|u'|/U_b$ (Bruggeman et al., 1991). In the low amplitude regime ($|u'|/U_b < 10^{-3}$), linear theory predicts an exponential amplification of disturbances, resulting in a growth rate of $e^{2\pi} \approx 500$ over a single hydrodynamic wavelength (Bruggeman et al., 1986). The exponential growth imposes a limit to the applicability of the linear theory, since the perturbation amplitude should remain small for the theory to hold. Discrete vortices are formed at higher perturbation levels. The vorticity contained in a hydrodynamic wavelength is then concentrated in these vortices. In the high perturbation amplitude regime (where $|u'|/U_b > 10^{-1}$) the acoustic field directly influences the shear layer behavior, but this regime is not attained in the present work. In the intermediate regime, the strength of the shed vortices does not depend on the perturbation amplitude, considering all vorticity is concentrated in the coherent vortices. The acoustic source power then scales linearly with $|u'|/U_b$. The boundaries between the different regimes are expected to depend on the geometry and properties of the studied flow.

The source power is related to the Coriolis force exerted on the acoustic field by the flow (Howe, 1980):

$$\langle P_{source} \rangle = -\rho_0 \left\langle \int_V (\boldsymbol{\omega} \times \boldsymbol{u}) \cdot \boldsymbol{u}'_{ac} dV \right\rangle. \tag{4.5}$$

Assuming that all vorticity ($\boldsymbol{\omega}$) is concentrated in the vortices means that $\boldsymbol{\omega}$ scales with U_b, as does the flow velocity $\boldsymbol{u}$. The source power then scales as $\langle P_{source} \rangle = f(\rho_0 U_b^2 u'_{ac})$. Conversion of the acoustic velocity to a fluctuating pressure (using $p'_{ac}/(\rho_0 c_{eff}) = u'_{ac}$) and summation over all corrugations yields a description for the acoustic source power of a corrugated pipe:

$$\langle P_{source} \rangle = \frac{2}{\pi} n_c K \rho_0 U_b^3 A_p \frac{c_0}{c_{eff}} \left(\frac{|p'_{max}|}{\rho_0 c_0 U_b} \right), \tag{4.6}$$

where K is the acoustic source strength constant, which can be obtained from experiments or simulations, and which is geometry specific. n_c is the number of cavities along the pipe, U_b is the bulk gas flow velocity, A_p the cross-sectional area of the pipe, c_0 and c_{eff} are the normal and the effective speed of sound, respectively (see Equation 4.1), ρ_0 the quiescent fluid density, and $|p'_{max}|$ is the maximum amplitude of the acoustic standing pressure wave in the pipe. The factor $2/\pi$ is related to the average amplitude of the sinusoidal standing wave in

the pipe: $\overline{|p'_{ac}|} = 2/\pi |p'_{max}|$.

Viscothermal losses

Now that an expression for the acoustic sources is obtained, the acoustic losses are estimated. First the viscothermal losses are treated (the first term on the right hand side of Equation 4.4). These losses occur in the viscous and thermal boundary layers at the pipe wall. The viscothermal losses in the pipe are related to the reduction of the acoustic intensity of sound waves over the pipe length:

$$\langle P_{vt} \rangle = A_p \left[\frac{1}{2} \langle I^+_{in} \rangle - \langle I^+_{out} \rangle \right] + A_p \left[\frac{1}{2} \langle I^-_{in} \rangle - \langle I^-_{out} \rangle \right], \tag{4.7}$$

where $\langle I^{\pm}_{in} \rangle$ and $\langle I^{\pm}_{out} \rangle$ are the average acoustic intensities for the upstream (-) and downstream (+) traveling waves at the inlet and outlet, respectively. Using the definition of the average intensity $\langle I \rangle$ for plane waves with amplitudes $p'_{\pm}$, being $\langle I^{\pm} \rangle = \frac{|p'_{\pm}|^2}{2\rho_0 c_0}$, an equation is derived for the viscothermal losses in the main pipe:

$$\langle P_{vt} \rangle = \left[\rho_0 \frac{c_0^2}{c_{eff}} U_b^2 A_p \right] \left(2 - e^{(2\alpha_+ L_p)} - e^{(2\alpha_- L_p)} \right) \left(\frac{|p'_+|}{\rho_0 c_0 U_b} \right)^2, \tag{4.8}$$

where $\alpha_{\pm}$ are the acoustic damping coefficients for sound waves traveling in the downstream (+) and upstream (-) directions in the pipe, and L_p is the pipe length. It is assumed that the upstream and downstream traveling waves are of equal amplitude. For the standing acoustic wave it then holds that $|p'_+| = |p'_-| = |p'_{max}|/2$. Furthermore, $\alpha_+ + \alpha_- \approx 2\alpha_0$, with α_0 being the acoustic damping coefficient at quiescent conditions. The following expression is then obtained:

$$\langle P_{vt} \rangle \cong \left[\frac{1}{4} \rho_0 \frac{c_0^2}{c_{eff}} \left(1 - e^{2\alpha_0 L_p} \right) U_b^2 A_p \right] \left(\frac{|p'_{max}|}{\rho_0 c_0 U_b} \right)^2. \tag{4.9}$$

The acoustic damping coefficient for a smooth pipe (α) is studied extensively in literature (an overview is provided by Weng, 2015). α is related to the imaginary part of the complex wavenumber ($\alpha = -Im(k)$). Here, for the wavenumber, the model developed by Dokumaci (1995) is used. In the high shear number limit ($sh = \frac{1}{2} D_p \sqrt{\omega_{ac}/\nu} \gg 1$, where ω_{ac} is the angular acoustic frequency, D_p the pipe diameter, and ν the kinematic viscosity), it reads as:

$$k_{\pm} = \frac{\omega_{ac}}{c_0} \frac{\pm \Gamma_0}{1 \pm Ma \Gamma_0}, \tag{4.10}$$

where $k_{\pm}$ are the complex valued wavenumbers for up- and downstream traveling waves, and Ma ($= U_b/c_0$) is the Mach number. Γ_0 is a dimensionless wavenumber for sound propagation through a quiescent fluid inside a pipe, taking into account the viscothermal damping only. This model neglects acoustic attenuation by turbulent fluctuations in the bulk of the flow, because the ratio of acoustic boundary layer thickness to thickness of the viscous sublayer of

the turbulent mean flow is in the order of one ($\delta_{ac}^{+} = \delta_{ac}/\delta_l \approx 1$; see Weng, 2015). At high shear numbers, Γ_0 can be approximated by (Ronneberger and Ahrens, 1977):

$$\Gamma_0 = 1 + \frac{1-i}{sh\sqrt{2}}\left(1 + \frac{\gamma-1}{\sqrt{Pr}}\right) - \frac{i}{sh^2}\left(1 + \frac{\gamma-1}{\sqrt{Pr}} - \gamma\frac{\gamma-1}{2Pr}\right), \tag{4.11}$$

where Pr is the Prandtl number, the ratio of momentum over thermal diffusivity ($Pr = c_p\mu/\kappa$, with c_p the specific heat capacity and κ the thermal conductivity), and γ is the Poisson constant. An effective pipe length is used for the corrugated pipe section, where the pipe length is adapted using the arc length of the pipe wall in axial direction. This yields increased viscothermal losses for a corrugated pipe (approximately doubled compared to a smooth pipe), comparable to what was found by Belfroid et al. (2018).

Radiation and convection losses

The convective and radiative acoustic losses (second and third right hand side terms in Equation 4.4) at the pipe inlet (towards the expansion chamber) and outlet (flanged open pipe) can be calculated from the acoustic intensity at the respective pipe terminations (Hirschberg and Rienstra, 2004):

$$\langle P_{rad+conv}\rangle = A_p\left[\langle I_{in}\rangle + \langle I_{out}\rangle\right]. \tag{4.12}$$

In this equation, $\langle I_{in}\rangle$ and $\langle I_{out}\rangle$ are the time-averaged acoustic intensities leaving the pipe at the inlet and the outlet, respectively. To obtain these intensities, the acoustic reflection coefficients at the upstream and downstream pipe terminations are required (R_i and R_o). Measurements are carried out to assess the pressure reflection coefficient in the absence of a mean flow for the upstream expansion vessel. A speaker is connected to a smooth steel pipe section (5 mm wall thickness), ending at the expansion vessel. The reflection of the incoming acoustic waves by the vessel is measured using the multiple microphone method (Jang and Ih, 1998). The results are compared to the reflection coefficients for an unflanged pipe (Levine and Schwinger, 1948) and a flanged pipe (Norris and Sheng, 1989) in Figure 4.1. A good agreement is found between the reflection coefficient of the expansion vessel and the flanged pipe, and this relation is therefore used to obtain R_i and R_o. The convective effect of a mean flow on the reflection coefficient is widely studied (e.g. by Ingard and Singhal, 1975; Davies, 1987; Munt, 1977, 1990 and Peters et al., 1993). For the upstream pipe termination, which is essentially the flow intake, the effect of the mean flow is related to flow separation. Davies (1987) studied this configuration and obtained the following estimation for the effect of a mean flow on the pressure reflection coefficient:

$$R_i = R_0\left((1-\beta Ma)/(1+\beta Ma)\right)^{0.9}, \tag{4.13}$$

where R_0 is the pressure reflection coefficient at quiescent conditions, and β a correction factor to account for additional losses due to flow separation at the sharp-edged inlet. The best fit to experimental data was obtained for $\beta = 1.63$. This expression is combined with the reflection coefficient obtained by Norris and Sheng (1989). For the downstream termination, the effect of the Mach number on the reflection coefficient is taken from Ingard and Singhal (1975). Their result is valid for $kD_p/2 \ll 1$, which does not hold for the present experiments. The reflection coefficient for a flanged pipe in no-flow conditions (by Norris and Sheng, 1989)

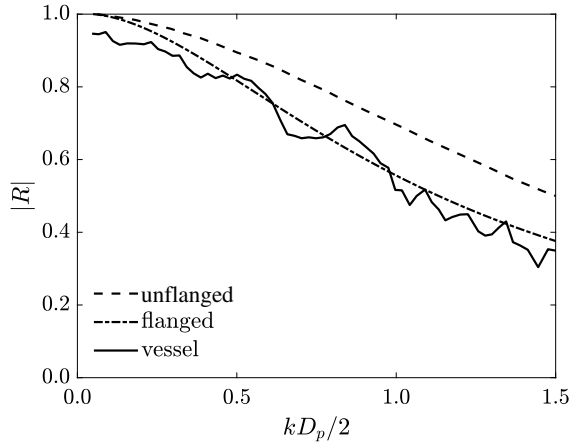

Figure 4.1: Experimentally obtained reflection coefficient for the expansion vessel, compared to the reflection coefficient from an unflanged (Levine and Schwinger, 1948) and flanged pipe (Norris and Sheng, 1989).

is therefore used. Although Munt (1990) showed that the behavior is different for increasing Mach numbers, this difference is rather small for the Mach number range attained in the reported experiments. Moreover, the theory of Munt does not hold for a flanged pipe end, and no literature is available that studies the effect of the Mach number for this case.

$\langle I_{in} \rangle$ and $\langle I_{out} \rangle$ in Equation 4.12 are related to the intensities of the acoustic waves traveling inside the pipe:

$$\begin{aligned} \langle I_{in} \rangle &= \langle I_{in}^- \rangle - \langle I_{in}^+ \rangle = (1 - R_{E,i}) \langle I_{in}^- \rangle, \qquad \text{and} \\ \langle I_{out} \rangle &= \langle I_{out}^+ \rangle - \langle I_{out}^- \rangle = (1 - R_{E,o}) \langle I_{out}^+ \rangle, \end{aligned} \tag{4.14}$$

where $R_{E,i/o}$ are the energy reflection coefficients at the pipe inlet and outlet. These are obtained from the pressure reflection coefficients, according to (Ingard and Singhal, 1975):

$$R_{E,i/o} = R_{i/o}^2 (1 \pm Ma)^2 / (1 \mp Ma)^2. \tag{4.15}$$

Combining Equations 4.13, 4.14 and 4.15 with Equation 4.12, and introducing a loss coefficient at the pipe ends ($\alpha_{r,i/o} = 1 - R_{E,i/o}$), results in the following expression for the radiative and convective losses at the inlet and outlet of the pipe:

$$\langle P_{rad+conv,i/o} \rangle = \left[\frac{1}{2} \alpha_{r,i/o} \rho_0 \frac{c_0^2}{c_{eff}} U_b^2 A_P \right] \left(\frac{|p'_{-,i/+,o}|}{\rho_0 c_0 U_b} \right)^2. \tag{4.16}$$

Since the reflection coefficient for higher whistling frequencies is significantly lower than unity, the assumption that $|p'_{max}| = 2|p^+|$ does not hold at the pipe ends. In crude approxi-

mation it takes the form of $|p'_{max}| = (1 + R_i)|p'_{-,i}|$ at the inlet and $|p'_{max}| = (1 + R_o)|p'_{+,o}|$ at the outlet. This yields:

$$\langle P_{rad+conv,i/o} \rangle = \left[\frac{1}{2} \alpha_{r,i/o} \rho_0 \frac{c_0^2}{c_{eff}} U_b^2 A_P \right] \left(\frac{|p'_{max}|}{\rho_0 c_0 U_b (1 + R_{i/o})} \right)^2. \tag{4.17}$$

Combining Equations 4.6, 4.9 and 4.17 with Equation 4.4, yields a time-averaged power balance, which is used to evaluate whistling in corrugated pipes and to compare it to numerical results. The power balance has the form of

$$A \left(\frac{|p'_{max}|}{\rho_0 c_0 U_b} \right) = B \left(\frac{|p'_{max}|^2}{(\rho_0 c_0 U_b)^2} \right), \tag{4.18}$$

where A and B are parameters related to the flow and fluid properties and the geometry of the system.

4.2.2 ACOUSTICS OF A LIQUID DROPLETS IN A FLUID

Injection of liquid into a gas flow inside a pipe increases the acoustic damping. It was shown previously that in corrugated pipes the majority of the liquid is present as droplets in the core of the flow, in contrast to smooth pipes where the liquid is transported as a film along the pipe wall (van Eckeveld et al., 2018). The presence of this dispersed phase causes additional acoustic damping. It is of a viscothermal nature, originating from the viscous and thermal boundary layers occurring at the gas-liquid interface of the droplets. The viscous and thermal effects are intermingled, but can in practice always be divided into two separate parts (Epstein and Carhart, 1953):

$$\beta_d = \beta_\tau + \beta_\nu. \tag{4.19}$$

Here β_d is the viscothermal damping coefficient, due to the presence of droplets. Epstein and Carhart (1953) derived an explicit formula for the viscous damping coefficient β_ν, which is valid for acoustically small water droplets ($d_p \ll \lambda_{ac}$) suspended in an air flow:

$$\beta_\nu = \frac{6\pi d_p}{2c_0} n_d \nu Y_\nu, \tag{4.20}$$

$$\text{with :} \quad Y_\nu = (1 + z) \frac{16z^4}{16z^4 + 72\delta z^3 + 81\delta^2(1 + 2z + 2z^2)}, \tag{4.21}$$

$$\text{and :} \quad z = \left(\frac{\omega_{ac}}{2\nu} \right)^{1/2} d_p/2. \tag{4.22}$$

For the thermal damping coefficient β_τ, the explicit formula reads:

$$\beta_\tau = \frac{4\pi d_p}{2c_0} n_d(\gamma - 1)\epsilon Y_\tau, \tag{4.23}$$

$$\text{with :} \quad Y_\tau = 1 + \left(\frac{\omega_{ac}}{2\epsilon}\right)^{1/2} d_p/2. \tag{4.24}$$

In these formulations, d_p is the droplet size, n_d the number of droplets per unit pipe length, δ the ratio of the gas and liquid densities, and ϵ the thermal diffusivity. Using the additional viscothermal damping coefficient per unit pipe length (β_d, Equation 4.19), the total acoustic damping due to the presence of droplets is:

$$\langle P_{drop} \rangle \cong \left[\frac{1}{4}\rho_0 \frac{c_0^2}{c_{eff}} \left(1 - e^{2\beta_d L_w}\right) U_b^2 A_p\right] \left(\frac{|p'_{max}|}{\rho_0 c_0 U_b}\right)^2, \tag{4.25}$$

where L_w is the wetted pipe length, taken as the distance from the liquid injection point to the pipe exit. Combining Equation 4.25 with Equation 4.18, the total energy balance for the pipe system is:

$$A\left(\frac{|p'_{max}|}{\rho_0 c_0 U_b}\right) = (B + B_{drop})\left(\frac{|p'_{max}|^2}{(\rho_0 c_0 U_b)^2}\right), \tag{4.26}$$

where B_{drop} represents the additional damping due to the presence of droplets. To evaluate the droplet damping, it is therefore required to have information on the droplet size distribution and the droplet concentration inside the pipe.

4.2.3 HOWE'S THEORY OF VORTEX SOUND

Different acoustic analogies have been developed in the past to relate flow properties to sound production. For the studied case, with a solid and stationary body present in a low Mach number flow, two well-known acoustic analogies have been proposed, by Curle (1955) and by Howe (1980). Curle's theory builds on Lighthill's analogy (Lighthill, 1952) and generalizes Lighthill's results by incorporating the presence of stationary and rigid bodies. The perturbation density ($\rho' = \rho - \rho_0$) is used as the acoustic variable. On the other hand, Howe's theory of vortex sound (Howe, 1980) is a generalization of the acoustic analogy developed by Powell (1964) for stationary and rigid bodies in a flow, and uses the total or stagnation enthalpy ($h_t = h + \boldsymbol{u}^2/2$, with h being the specific enthalpy) as acoustic variable. In cavity flows and corrugated pipe flows, the major contributors to the sound production are large coherent vortices, generated in the shear layer spanning the cavities (see Figure 4.2). They dominate over sound production from three-dimensional free turbulence. It is, therefore, intuitive to proceed with Howe's formulation of vortex sound in the present work, because it provides insight into the role of vorticity on the sound production. This theory is briefly introduced here. For fur-

ther details the reader is refered to Hirschberg and Rienstra (2004). The energy corollary of Howe defines the time-averaged acoustic source power as follows:

$$\langle P_{source} \rangle = -\rho_0 \left\langle \int_V (\boldsymbol{\omega} \times \boldsymbol{u}) \cdot \boldsymbol{u}'_{ac} dV \right\rangle, \tag{4.27}$$

where V is the volume in which the vorticity $\boldsymbol{\omega}$ is non-vanishing, $\boldsymbol{u}$ is the flow velocity, which is composed of the time-averaged velocity $\boldsymbol{u}_0$ and the hydrodynamic and acoustic fluctuating components ($\boldsymbol{u}'_h$ and $\boldsymbol{u}'_{ac}$, respectively). The source of sound is related to the Coriolis force density ($f_c = -\rho_0(\boldsymbol{\omega} \times \boldsymbol{u})$), originating from the interaction of the vortex structures with the acoustic field. This acoustic field is defined as a potential velocity field by Howe (1980), which is accurate for the present case because of the large value of the Womersley number $\left(\sqrt{\frac{\rho_0 \omega_{ac} D_p^2}{4\mu_g}} \gg 1 \right)$. The Womersley number ranges from approximately 300 to 900 for the reported experiments, satisfying this criterion. The acoustic streamlines for a typical cavity geometry are depicted in Figure 4.2, together with a vortex traveling in the cavity mouth. The acoustic source power is obtained numerically using Eq. eq. (4.27) in the numerical modeling described in Section 4.6.

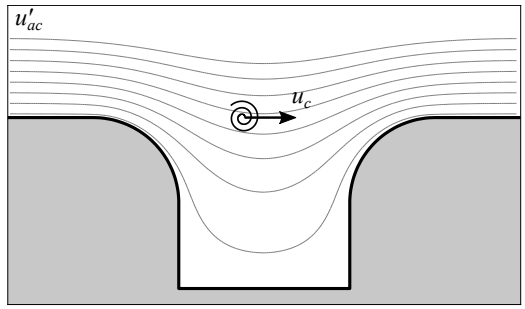

Figure 4.2: Schematic representation of the acoustic streamlines over a cavity structure, with a coherent vortex traveling in the cavity mouth with velocity $\boldsymbol{u}_c$. The interaction of the vortex with the acoustic field is a source of sound.

4.3 EXPERIMENTAL

The experiments are carried out in a dedicated open flow loop, where both acoustic measurements and optical measurements are performed. This setup is previously used by the authors, and documented in literature (van Eckeveld et al., 2017, 2018). The setup and the different measurement techniques are, therefore, only briefly discussed here.

4.3.1 EXPERIMENTAL SETUP

A schematic overview of the setup is provided in Figure 4.3. It consists of a blower to provide the air flow, which is followed by an expansion vessel.The vessel both serves to prevent the blower noise to reach the test section and to provide a high reflection acoustic boundary con-

dition for the measurement section, thereby promoting whistling. After the expansion vessel, an acoustic measurement section is placed. Liquid is injected in the vertical part of the setup using a spray nozzle at the pipe centerline. The liquid flow is provided by a rotary vane pump, and the flow rate is measured with a Coriolis mass flow meter. The liquid injection point is followed by a smooth pipe development section, made of steel with a wall thickness of 5 mm. The flow then enters the corrugated pipe, machined from PVC. Several different corrugation geometries are used. They are depicted in Figure 4.4 and the geometrical details are listed in Table 4.1. Geometry A is considered as the base case. It is a generalized cavity geometry, and its typical sizing is comparable to many industrially used corrugated pipes. The edges are rounded to enhance whistling, and to resemble industrial applications. The geometries B and C are similar, with only a reduction in the cavity depth and length, respectively. Geometry D is an enlarged version of geometry A, and the geometries E and F are triangular ribs with similar cavity volumes as geometry A. The dimensions for all geometries are listed in Table 4.1. The pipe diameter (D_p) is 49.25 *mm* for all pipes. The total pipe length (L_p) is 3 m for geometries A, B and C, and 3.6 m for geometries D, E and F. The number of cavities (n_c) for all geometries is over 350. For two corrugation geometries (geometry A and D in Table 4.1) a transparent section (machined from PMMA) with a length of 0.6 m is used for optical access. This section is located towards the end of the corrugated pipe, at $49 \leq L/D_p \leq 53$ for geometry A and at $65 \leq L/D_p \leq 69$ for geometry D. It is contained in a water-filled optical box, to reduce refraction of light at the curved outer pipe wall. The setup ends with an open outflow, blowing into a large room, with no acoustic treatment to the walls. Apart from the measurements described in the following sections, static pressure and temperature measurements are carried out to correct the gas flow rate with the actual gas density.

For all measurements, air is used as the gas phase. It is taken from the atmosphere and does not undergo any pre-treatment. For the liquid injection, two different liquids are used: water and mono-ethylene glycol (MEG). MEG is used for its significantly higher viscosity compared to water (16 times more viscous). Also the surface tension is different for MEG (48 *mN/m*, compared to 72 *mN/m* for water). The density of MEG is approximately 10% higher than the density of water (Lide, 1994).

4.3.2 ACOUSTIC MEASUREMENTS

Four microphones (PCB 106B acoustic pressure sensors) are placed in the acoustic measurement section. The position of the microphones is based on the acoustic frequency range that is expected from the studied corrugated pipes (maximum 3.5 *kHz*). The spacing between the microphones is based on the work by Jang and Ih (1998), and is chosen to be 0.225 m, 0.315 m and 0.360 m for the second, third and fourth microphone, relative to the first microphone. They are connected to an ICP signal conditioner, and data is recorded with a data acquisition card (National Instruments PCI-4472). The pressure signals are acquired at a rate of 40 *kHz*, to prevent aliasing from influencing the measurements. Acoustic signals are recorded over a period of two seconds, and repeated four times for every measurement point. The traveling acoustic waves are reconstructed using the multi-microphone method (Jang and Ih, 1998). Subsequently the acoustic amplitude of the standing wave in the pipe is obtained from the traveling waves.

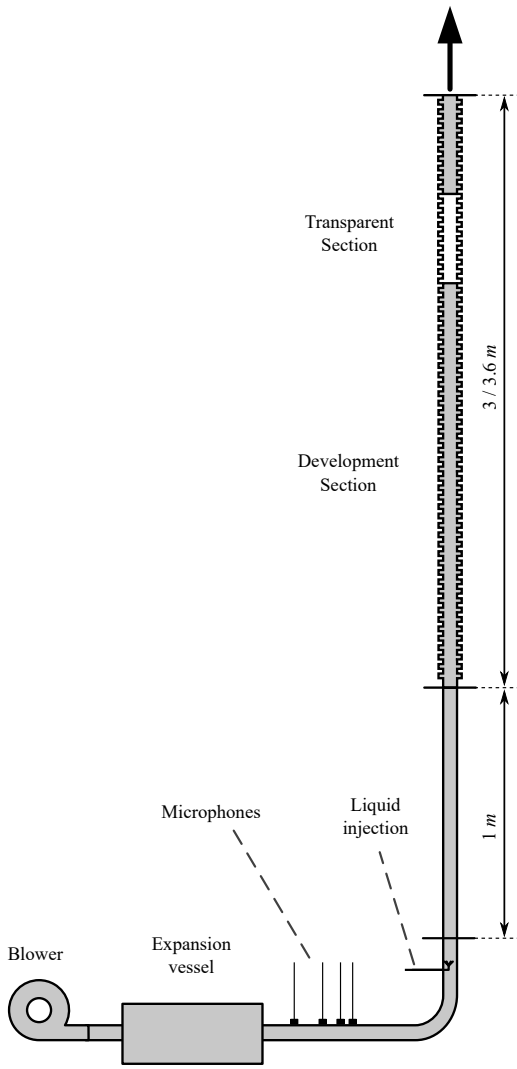

Figure 4.3: Schematic representation of the experimental set-up. The gas flow is created by a blower, followed by an expension vessel to prevent the blower noise to reach the test section and to provide a large reflection coefficient boundary condition at the pipe inlet. The flow subsequently enters the acoustic measurement section. Liquid is injected with a spray nozzle at the pipe centerline. The corrugated section is vertical and flow is in upward direction. The corrugated section is partly transparent for the optical measurements.

Geom	A	B	C	D	E/F	ref
L_c [mm]	4	4	2.46	6	*	40
H_c [mm]	4	2.46	4	6	*	27
r_{ed} [mm]	2	2	2	2	2	5
Pt [mm]	8	8	8	10	10	-
L_p [m]	3.0	3.0	3.0	3.6	3.6	-
n_c [-]	374	374	374	359	359	1
Sr_{pw} [-]	0.36	0.30	0.28	0.41	0.35/-	0.73

Table 4.1: Corrugation geometries used in the present study (see Figure 4.4). The reference geometry (*ref*) is taken from Nakiboğlu et al. (2012a) and used is as a benchmark in Section 4.6. For geometries E and F it is difficult to define the cavity length and depth (indicated with ✳) due to the slanted cavity bottom.

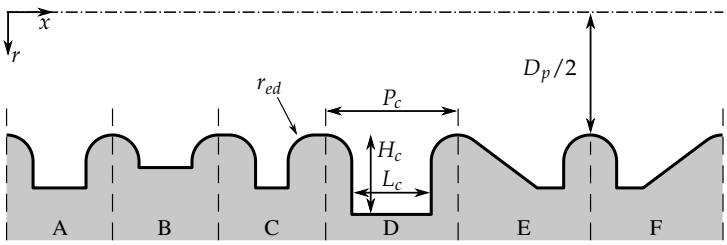

Figure 4.4: Schematic representation of the different cavity geometries used in the present study. The cavity size in the figure is exaggerated with respect to the pipe diameter. Definition of the cavity sizes is given in geometry D, values are found in Table 4.1.

4.3.3 LIQUID CAVITY FILLING MEASUREMENTS

The accumulation of liquid between the individual corrugations is measured in the transparent sections of geometry A and D using a *planar laser-induced fluorescence* (PLIF) technique. The technique is similar to PLIF techniques used for film thickness measurements in two-phase annular pipe flow (Schubring et al., 2010), and is previously used for corrugated pipes (van Eckeveld et al., 2017, 2018). A fluorescent dye is added to the injected liquid (rhodamine WT), which is illuminated using a laser. Images are recorded with a CCD camera (LaVision Imager LX 16M) equipped with a 105-*mm* Nikkor objective and an optical high-pass filter to only capture the fluorescent light emitted by the liquid at the pipe wall. An example of an image obtained from these experiments is depicted in Figure 4.5. The regions where liquid is present are the high intensity regions. The corrugations are indicated in red and the white boundary is obtained after several image processing steps. Note that, due to refraction at the curved pipe wall, liquid cannot be detected accurately on top of the ribs (indicated by the dashed regions in Figure 4.5). Only liquid that is attached to the pipe wall can be accurately reconstructed.

4.3.4 DROPLET SIZING MEASUREMENTS

The droplet size distribution is obtained using a combination of two different measurement techniques: *interferometric particle imaging* (IPI, Glover et al., 1995) and *shadowgraphic particle imaging* (SPI). Droplet sizes are measured at the pipe outlet, after removal of the liquid film at the pipe wall using a slit (Hay et al., 1996; van Eckeveld et al., 2018). The combination of IPI and SPI enables the measurement of a wide range of droplet sizes, up from a few μm in diameter.

For SPI, a diffusive white background is illuminated from the backside with a pulsed laser. The droplets are passing between this illuminated background and the CCD camera, creating shadows on the camera sensor plane, which appear as dark circles in the images. After application of a background correction step and a median filter (3x3 pixels), the droplet edges are detected using a canny filter, combined with a convex hull technique to fill the edges. The

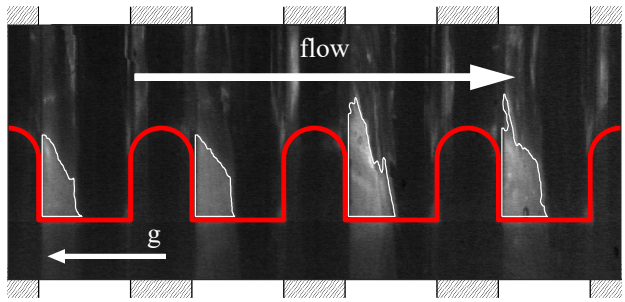

Figure 4.5: A typical image obtained from the cavity filling measurements in geometry D. Flow is from left to right, gravity acts in opposite direction. High intensity areas are regions of liquid accumulation. The corrugations are in red, and the detected gas-liquid interface is traced by the white boundary. Liquid on top of the ribs (indicated by the dashed areas) is not detected accurately, due to the curved edges.

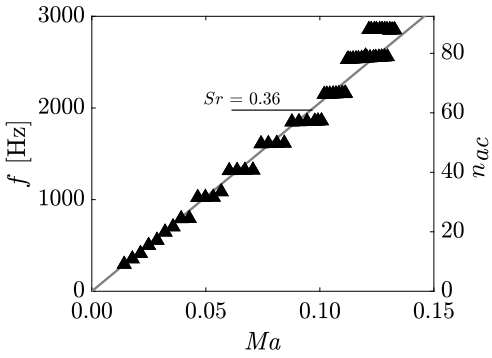

Figure 4.6: Whistling frequency (f) as a function of the Mach number for geometry A, showing the step-wise increase in whistling frequency. The solid line represents $Sr = 0.36$. The right hand side y-axis shows the acoustic resonance mode n_{ac} of the pipe system (see Equation 4.2), associated to the whistling frequency.

resulting images are used to obtain the droplet size distribution. The minimum droplet size that can be detected accurately with the used SPI setup is around 50 μm in diameter. Each measurement series consists of 500 images, and every measurement is repeated twice.

To be able to detect smaller droplets, the SPI technique is combined with IPI measurement (Glover et al., 1995). In these measurements, a laser sheet is used to illuminate the droplets exiting the pipe. When observed from the side, this illumination creates two glare points, one at each side of a droplet. When the image is defocused, the light emitted from the two glare points overlaps and interferes, resulting in a fringe pattern due to the coherent laser light. The droplet diameter is found directly from the fringe spacing of the interference disks.

The droplet size distributions obtained from SPI and IPI overlap in a specific size range. This overlap region is used to match the two distributions into a single droplet size distribution, representing the entire droplet cloud exiting the pipe (van Eckeveld et al., 2018).

4.4 DRY WHISTLING - EXPERIMENTAL

The whistling frequency in single-phase conditions shows a globally linear increase with increasing flow velocity, associated with the increased convection velocity of the vortices in the cavity mouth (see Figure 4.6). The steps are so-called plateaus in the whistling frequency, caused by the finite number of resonance frequencies of the entire pipe system (see Equation 4.2). The characteristic vortex shedding frequency locks with one of the eigen-frequencies of the system. This also causes scatter in the whistling Strouhal number (Sr), as is shown in Figure 4.7a. The whistling Strouhal number ranges from 0.32 to 0.40, which is in accordance with previous work for this geometry (Nakiboğlu et al., 2010). The dimensionless whistling amplitude, which is depicted in Figure 4.7b, increases with increasing flow velocity up to a Mach number of approximately 0.03. The amplitude slightly decreases for higher flow rates, as a consequence of a reduction in the acoustic reflection coefficient at the pipe ends (see Figure 4.1). An increase in whistling frequency results in higher acoustic losses, causing less acoustic energy to remain trapped inside the pipe. Within a single frequency plateau, the amplitude peaks in the middle of the plateau, and decreases towards the edges.

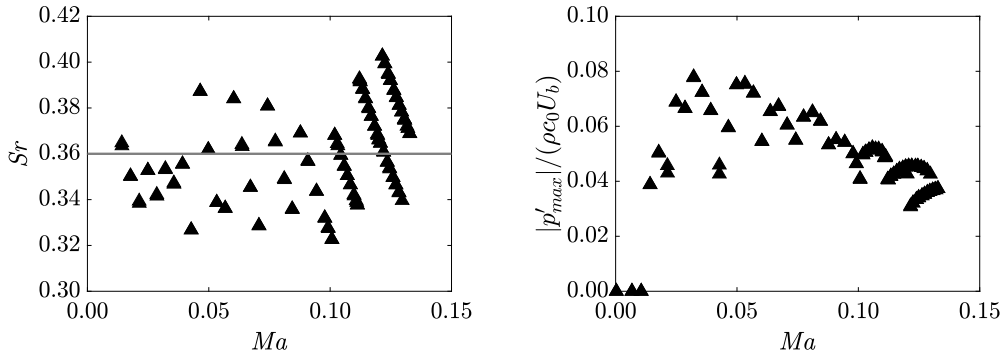

Figure 4.7: (a) Whistling Strouhal number (Sr) as a function of Mach number for geometry A. The scatter in the data is caused by the plateaus in whistling frequency, also observed in Figure 4.6. (b) Dimensionless amplitude of the acoustic standing wave ($|p'_{max}|/(\rho_0 c_0 U_b)$) as a function of the Mach number for geometry A

Whistling is studied in a range of cavity geometries. The geometries are depicted in Figure 4.4. Figures 4.8a, 4.8b and 4.8c summarize the acoustic behavior for the different geometries. When the cavity depth is decreased (from $H_c/L_c = 1$ for geometry A to $H_c/L_c = 0.615$ for geometry B), the peak whistling Strouhal number decreases from 0.36 to 0.30. A similar behavior was previously observed by, for example, Sarohia (1975) for a different cavity geometry. The effect was attributed to a reduced convection velocity of vortices in the cavity mouth, as a result of the vortex-wall interaction (Nakiboğlu et al., 2012a). Nakiboglu et al. qualitatively modeled this frequency change using the method of image vortices (White, 2017). When the cavity bottom is in closer proximity to the shear layer, the interaction with the wall strengthens. The whistling amplitude also slightly decreases, due to the changed shear layer behavior. Whistling still occurs over the entire Mach number range covered by the experiments, and the onset velocity remains unchanged.

The corrugated pipe with narrow cavities (geometry C, $H_c/L_c = 1.626$) shows a different whistling behavior. Onset of whistling occurs at Ma = 0.08, as is shown in Figure 4.8c. The postponed onset is likely caused by the longer plateau between the cavities, and the shorter shear layer region over the cavities. The boundary layer growth over the plateau results in a thicker incoming boundary layer. This boundary layer is more stable, because of the decreased ratio of the cavity length over the incoming boundary layer thickness (Gharib and Roshko, 1987). The spatial extent of the cavity mouth, which is the region of sound productions, is also smaller for geometry C, resulting in a lower whistling amplitude. The longer effective smooth pipe length causes a further reduction of the amplitude, by adding viscothermal damping to the system.

Whistling in a corrugated pipe with geometry D, which is enlarged by 50%, follows the same trend as whistling in geometry A. The whistling amplitude is, however, significantly larger, and the decrease in amplitude at the higher Mach number range is not as strong. This is caused by a relative increase of the source region size per unit pipe length, yielding an increased acoustic amplitude. The relative importance of end effects is also reduced due to the larger pipe length. The increased cavity depth results in a small increase of the whistling Strouhal number, due to the reduced confinement effect for this geometry.

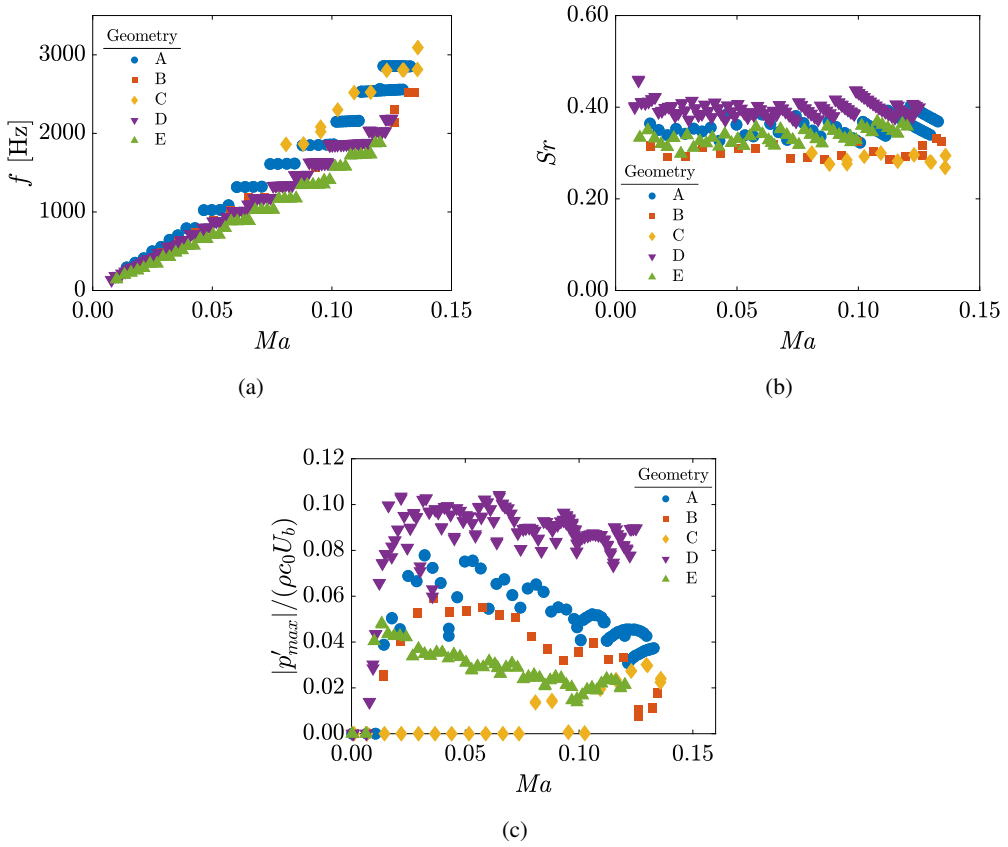

Figure 4.8: Whistling frequency, whistling Strouhal number and amplitude as a function of the Mach number, for the geometries depicted in Figure 4.4. (b) Whistling Strouhal number as a function of the Mach number, for the geometries depicted in Figure 4.4. (c) Dimensionless acoustic amplitude as a function of the Mach number, for the geometries depicted in Figure 4.4.

For the triangular corrugation geometries (geometries E and F) whistling is only observed when the slanted edge is at the upstream side of the cavity. When it is at the downstream side, the corrugated pipe remains silent. The acoustic field is altered, and the acoustic streamlines at the downstream cavity side are more aligned with the convection direction of the vortices. Knowing that the source of sound is related to $(\boldsymbol{\omega} \times \boldsymbol{u}) \cdot \boldsymbol{u}'_{ac}$ (as explained in Section 4.2.3), this causes a decrease of the amplitude of sound production, which is largely located at the downstream cavity edge as will be shown in Section 4.6.3. The geometry of the downstream cavity edge might also cause a change in shear layer behavior for geometry F, where vortices are ejected form the cavity mouth more easily (Heller and Bliss, 1976). Geometry E shows whistling over the entire Mach number range. Absorption at the upstream edge is decreased, compared to geometry F, and the slanted edge is located at the side where vortices are still small. The whistling Strouhal number is in the same range as was obtained for geometry A. The whistling amplitude is rather low, compared to the other geometries. It is expected that the confinement plays a significant role in the upstream half of the cavity. Cavity E seems to behave like a shallow version of cavity geometry D.

4.4.1 ENERGY BALANCE MODEL

Due to differences in the pipe length, the number of corrugations and the whistling frequency, it is difficult to quantitatively compare whistling in the different corrugation geometries using the acoustic pressure only. The acoustic losses for the different pipes are not the same, and also depend on the whistling frequency and amplitude. To be able to compare the whistling amplitude in a more quantitative way, an *energy balance model* (EBM, described in Section 4.2.1) is used. The experimental data are used as input (whistling amplitude and frequency, bulk flow velocity, temperature, pressure, system geometry, etc.), and the acoustic losses are estimated at the operating conditions. The viscothermal, and radiative and convective losses are calculated according to Equations 4.9 and 4.17, respectively. Knowing that under whistling conditions the time-averaged acoustic losses must balance the production of acoustic power, the required acoustic source strength can be obtained. This total source strength is divided by the number of corrugations present in the respective corrugated pipe, and the results are depicted in Figure 4.9 for the different corrugation geometries. The reported values are obtained at a gas flow velocity of 40 *m/s*, for which all geometries, apart from geometry F, exhibit whistling in the experiments. The viscothermal losses make up between 45 and 55% of the total acoustic losses for the different corrugated pipes. The obtained trend underlines the geometrical properties that determine the acoustic source strength of a specific corrugation geometry. The effect of the cavity length on the source strength is evident comparing geometries D, A, and C. Shorter cavities display a reduced source power, due to the reduction of the size of the source region. The difference in source power between geometry A and B is caused by the interaction with the cavity bottom that comes into play for shallower cavities. This is also expected to play an important role for geometry E. The slanted bottom at the upstream side of the cavity limits the growth of vortices in the shear layer, causing a strong reduction in source power for this geometry. The edge rounding, mainly for the upstream edge, is an important parameter for the whistling amplitude. With the experimentally studied geometries, however, it is difficult to quantitatively evaluate the impact of edge rounding on the whistling strength.

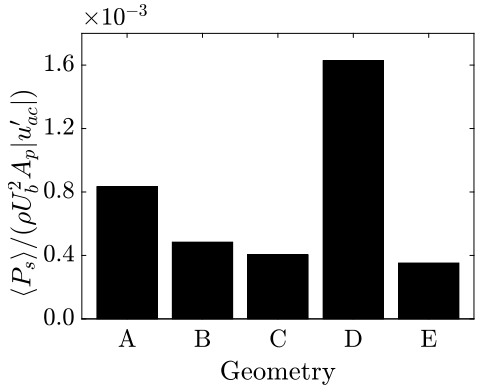

Figure 4.9: Experimentally obtained normalized acoustic source strength P_s for the different corrugation geometries studied, at $U_b = 40$ *m/s*. The energy balance model, described in Section 4.2, is used to estimate the acoustic losses in the system, resulting in the depicted source strength values.

4.5 LIQUID ADDITION - EXPERIMENTAL

When a liquid is added to the pipe flow upstream of the corrugated section (see Figure 4.3), the whistling amplitude is significantly reduced. This is depicted in Figure 4.10a, for water addition to air flow through a pipe with geometry A (see Table 4.1 and Figure 4.4 for geometrical details). A linear reduction of the acoustic amplitude with liquid volume fraction in the pipe is observed. The liquid volume fraction ϕ_l is defined as the ratio of the liquid volume flow rate over the gas volume flow rate. A very limited liquid fraction is sufficient to entirely suppress whistling in this geometry. The critical volume fraction increases with increasing gas flow velocity. Experiments in a corrugated pipe with geometry D show the same linear relation between acoustic amplitude and the amount of liquid added to the pipe flow (Figure 4.10b). The effect of the gas flow rate is, however, less evident. Still, more liquid is required for increasing gas flow velocities, however, especially in the higher gas flow regime, this effect is less pronounced as compared to results obtained for geometry A. The highest flow velocity still requires the largest liquid fraction to mitigate whistling entirely. For lower values of ϕ_l, however, the largest whistling amplitude is not always observed for the largest flow speed. Especially for $U_b = 35$ *m/s* and 42 *m/s*, the whistling amplitude at the lower ϕ_l range is considerably smaller, compared to the other flow velocities. For these cases, the lock-in between the acoustic standing wave and the cavity vortex shedding is less strong, probably caused by the decline of the whistling amplitude toward the edges of a frequency plateau. The effect of the presence of a liquid phase, nonetheless, follows the same trend as observed for geometry A and the other flow velocities. There is a significant difference in the amount of liquid required to mitigate whistling entirely for geometry A and D. As a consequence of the larger cavity size, more liquid is required to cause a considerable reduction in acoustic output. The higher acoustic source power for this geometry in single phase conditions (see Figure 4.9), also causes more acoustic damping or a greater source power reduction required to diminish whistling.

For the other studied geometries that showed whistling in dry conditions (geometries B, C and E), only geometry C and E still produce sound when liquid is added (see Figure 4.11).

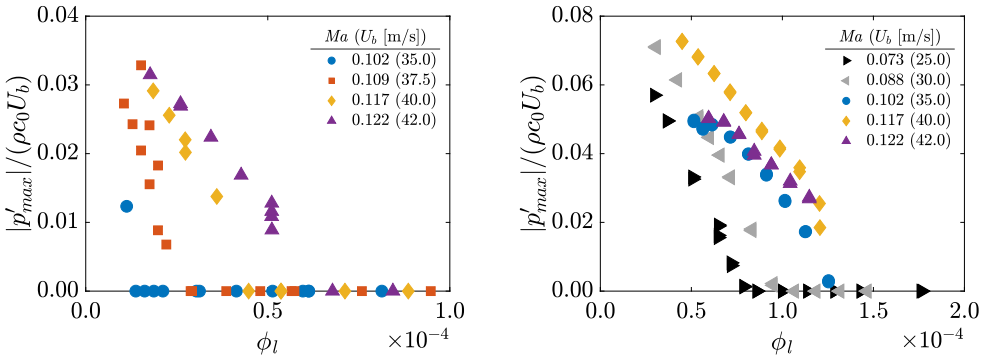

Figure 4.10: Dimensionless acoustic whistling amplitude as a function of the liquid volume fraction ϕ_l for pipes with a reference corrugation geometry A (a) and the enlarged geometry D (b, see Figure 4.4).

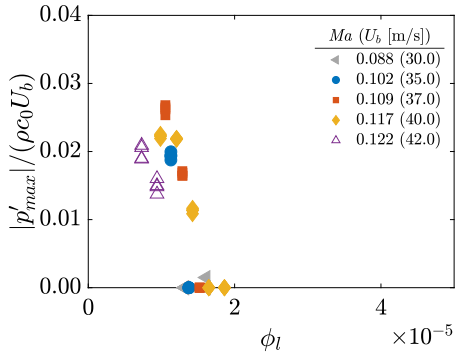

Figure 4.11: Dimensionless acoustic whistling amplitude as a function of the liquid volume fraction ϕ_l for corrugated pipes with geometry C (open markers) and E (closed markers).

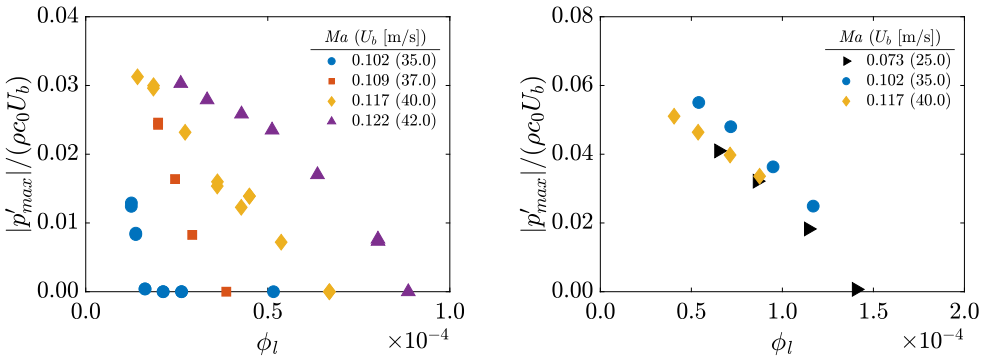

Figure 4.12: Dimensionless acoustic whistling amplitude as a function of the liquid volume fraction ϕ_l for corrugated pipes with geometry A (a) and D (b). Mono-ethylene glycol (MEG) is used in these measurements, instead of water (compare to Figure 4.10)

The pipe with the shallow cavities of geometry B remains silent. The short cavity of geometry C only whistles for the highest gas flow velocity (42 *m/s*), at very low liquid volume fractions. This also holds for the pipe with triangular cavities (geometry E): no whistling is observed for any gas flow velocity for $\phi_l > 1.5 \times 10^{-5}$.

To assess the effect of liquid properties on the whistling behavior, mono-ethylene glycol (MEG) is added to the dry gas flow, instead of water. A drawback of using MEG is that both surface tension and viscosity are changed simultaneously, resulting in a potentially intermingled effect of these two properties. However, using aqueous glycerine[1] might result in the evaporation of water from the solution over the length of the pipe, thereby causing changes in liquid properties which would complicate the measurements. Pure MEG is used instead, which has a surface tension of $\sigma = 48$ *mN/m* and a viscosity of $\mu_l = 16.1$ *mPa.s* at T = 298.15 *K* (Lide, 1994). Results are depicted in Figure 4.12a and 4.12b. When MEG is added to the flow instead of water, the required liquid flow rate for whistling mitigation is slightly increased. Only the result for $Ma = 0.117$ in geometry D deviates from the general trend observed in the experiments with water. Whistling under these conditions occurs at an increased frequency compared to whistling with water injection. The MEG injection causes mode switching to a different acoustic pipe mode, resulting in changes in acoustic boundary conditions and hence, changes in acoustic whistling amplitude. Comparison of Figure 4.12 with Figure 4.10 shows that it is unlikely that the viscosity of the used liquid has a significant effect on the resulting whistling mitigation behavior. MEG, which is 16 times more viscous than water, still shows similar acoustic behavior.

4.5.1 ACOUSTIC DROPLET DAMPING

Droplet sizing is performed using a combination of interferometric particle imaging (IPI) and shadowgraphic particle imaging (SPI), to be able to capture the full droplet size range present in the corrugated pipes (Section 4.3). Measurements are only carried out for geometry A, to assess the droplet size distribution and its effect on the acoustics of the entire pipe system.

To illustrate the potential effect of droplets on the acoustics, the case at a gas flow velocity of 42 *m/s* and with a liquid loading just beyond whistling (liquid flow rate of 305 *mL/min*, $\phi_l = 6.2 \times 10^{-5}$) is used as an example. The droplet size distribution under these conditions is depicted in Figure 4.13a. The displayed distribution is obtained by merging the distributions measured using IPI and SPI, and fitting an *upper limit lognormal* distribution through the result (Azzopardi, 1997; van Eckeveld et al., 2018). The accompanied additional acoustic damping coefficient, calculated according to Equations 4.19 - 4.24, is depicted in Figure 4.13b. It is assumed that all injected liquid is present as a dispersed phase in the bulk of the pipe flow, and that no liquid is present at the walls. From previous work it is known that the actual amount of entrained liquid approaches full entrainment for corrugated pipes. The liquid entrainment ratio at the studied conditions is approximately 0.9 (van Eckeveld et al., 2018). Assuming full entrainment, therefore, results in a slight overestimation of the acoustic damping by the presence of droplets. Figure 4.13b shows the damping coefficient β_d as a function of the droplet diameter, and of the Stokes number. As expected, the largest part of the damping originates from the viscous boundary layers surrounding the droplets (Epstein and

1 The surface tension of aqueous glycerine solutions with the same viscosity as pure MEG is approximately 67 *mN/m*, which is close to the surface tension of water (73 *mN/m*, Lide, 1994)

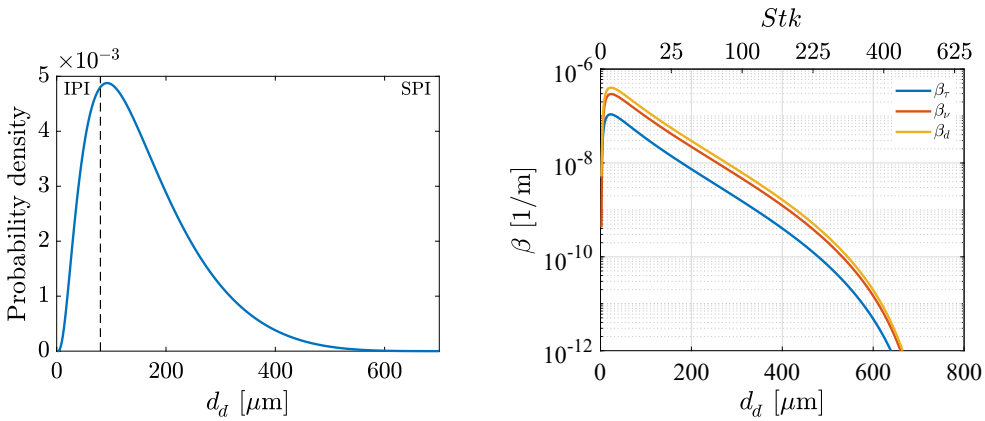

(a) (b)

Figure 4.13: (a) Droplet size distribution obtained for U_b = 42 *m/s* and at a liquid volume fraction of $\phi_l = 6.2 \times 10^{-5}$. The dashed line indicates the merging region of the measurements obtained from SPI and IPI. (b) The resulting additional acoustic damping coefficient β_d as a function of the droplet size for an acoustic wave with a frequency of 2500 *Hz*, obtained using Equations 4.19-4.24. The top x-axis shows the Stokes number for the respective particle diameter ($Stk = d_p^2 \omega_{ac} / \nu_g$).

Carhart, 1953). The total acoustic damping coefficient per unit pipe length due to the presence of droplets for this case amounts $\approx 3.5 \times 10^{-5} m^{-1}$. Assuming that the source power is unaffected by the presence of droplets, these additional acoustic losses cause a reduction of the fluctuation amplitude by approximately 0.01%. In the experiments, however, this volume fraction of liquid already caused total whistling mitigation. The presence of droplets is therefore not likely to play an important role in the reduction of the acoustic output from corrugated pipes. The interaction of droplets with the shear layers spanning the individual corrugations, however, might still be an important factor.

4.5.2 CAVITY FILLING

The filling of cavities with liquid is important for whistling mitigation in corrugated pipes (van Eckeveld et al., 2017). The liquid filling acts as a solid wall for the gas flow, as a consequence of the large difference in typical time-scales in the two phases. Liquid, therefore, changes the geometry of the corrugations. The acoustic amplitude was found to scale with the liquid filling fraction. In the previous work, geometry A was used, and water filling was assessed only. Those experiments are repeated and extended towards a different geometry (geometry D) and to a different working fluid (mono-ethylene glycol). The filling profile is measured using laser-induced fluorescence measurements, as described in Section 4.3. The filling is expressed using a liquid filling fraction (α), representing the fraction of the cavity volume filled with liquid, averaged in time and over several cavities.

Figure 4.14a shows the decreasing acoustic amplitude as a function of α, for two-phase water-air flow through a corrugated pipe with geometry A. A general trend is observed for different gas flow rates, where whistling is fully mitigated if α reaches values between 0.4 and 0.5. Data for the different gas flow velocities collapse onto a single line, indicating a univer-

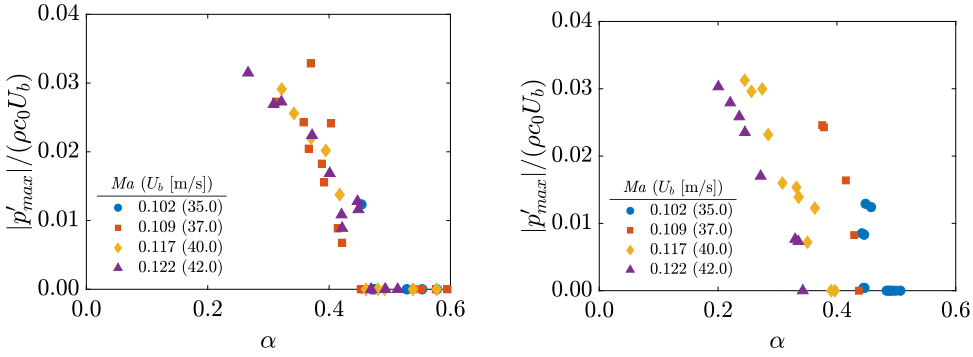

Figure 4.14: Dimensionless whistling amplitude as a function of the liquid filling fraction α, for geometry A with water (a) and MEG (b) injection.

sal behavior, where the filling is mainly responsible for the reduction in acoustic amplitude. The results are in good agreement with previous measurements in the same geometry (van Eckeveld et al., 2017).

Liquid cavity filling measurements are also carried out with a MEG-air two phase flow through the pipe with geometry A. The results are depicted in Figure 4.14b. The general behavior closely resembles that of water-air flow through the same pipe. No acoustic output is observed for a liquid filling fraction above 0.35 to 0.5, depending on the gas flow velocity. Compared to Figure 4.14a a larger spread is observed as a function of the gas flow rate.

For a pipe with corrugation geometry D, consisting of larger cavities, the behavior is very different (Figure 4.15). The whistling amplitude still decreases with an increase in the liquid filling fraction α. There is, however, a strong influence of the gas flow velocity on this trend. The filling fraction required to prevent whistling ranges from 0.2 to 0.5. An increase in gas flow rate results in a lower α required to fully mitigate whistling. It has to be noted that the range of bulk gas flow velocities is considerably larger compared to geometry A. For the highest gas flow rates, full mitigation of sound production is not achieved within the operating range of the experimental setup. The required liquid volume fraction ϕ_l could not be reached in this setup.

The liquid fill fraction does not properly describe the relevant geometrical changes to the cavities that cause reduction of the acoustic output. It is a global parameter, that does not give any insight in the specifics of the filling profile. To gain more insight in the effect of liquid filling, the filling profiles are plotted in Figures 4.16a, 4.16b and 4.16c. The profiles displayed represent different gas flow rates, at the point where whistling has just disappeared. The colors correspond to the colors used in Figures 4.14a, 4.14b and 4.15. A significant difference is observed in the effect of the gas flow rate on the filling profiles for the studied cases. For the base case (geometry A, water addition), the differences between the profiles are limited, and only occur through a change in effective, or empty cavity depth at the upstream side of the cavity. For the larger corrugation geometry (geometry D), there is a more significant change, mainly exhibited through a shortening of the empty cavity length. When switching to MEG,

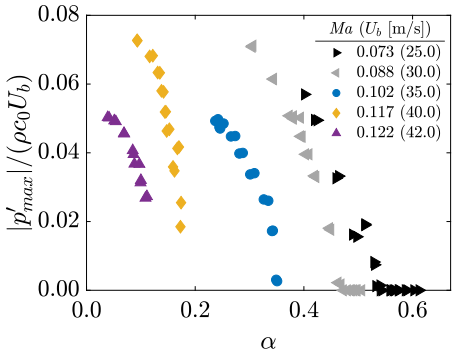

Figure 4.15: Dimensionless whistling amplitude as a function of the liquid filling fraction α, for geometry D, with water injection.

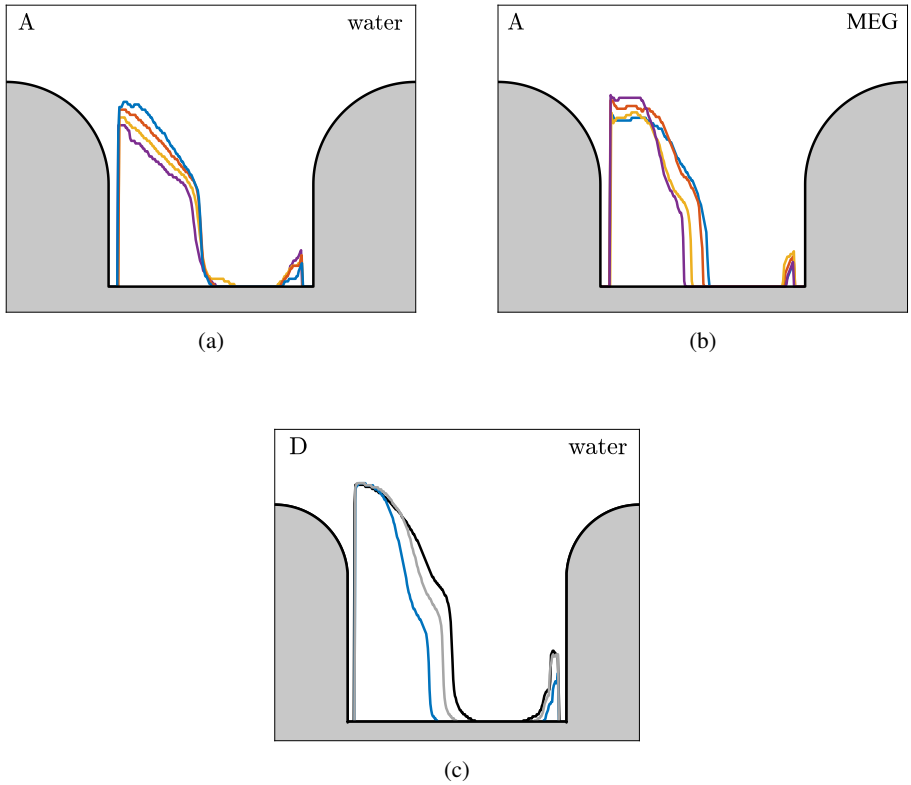

Figure 4.16: Averaged liquid filling profiles for geometry A with water injection (a) and MEG injection (b) and for geometry D with water injection (c). The profiles are for liquid flow rates where whistling has just disappeared. The colors correspond to the colors used in Figures 4.14a, 4.14b, and 4.15, respectively.

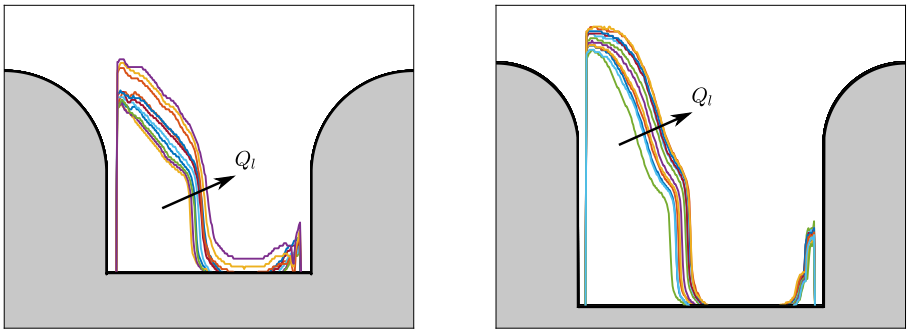

(a) (b)

Figure 4.17: Averaged liquid filling profiles for increasing liquid flow rates, in geometry A at $U_b = 40$ *m/s* (a) and geometry D at $U_b = 30$ *m/s* (b). The direction of increasing liquid flow rate is depicted in the Figures.

a similar behavior is observed, where the empty cavity length is reduced when the gas flow velocity increases.

Figures 4.17a and 4.17b show the filling profiles for different values of the liquid flow rate Q_l. The direction of increasing Q_l is depicted in the figures. For both cases depicted the empty cavity length gets shorter and the empty cavity depth at the upstream side decreases simultaneously, when the liquid flow rate is increased. When the liquid content is further increased, the downstream cavity depth starts to decrease, as is visible in Figure 4.17a. This occurs due to a mutual action of the surface tension and the decreasing recirculation cell strength. In geometry D, this point is not reached (see Figure 4.17b): no liquid accumulates at the downstream side of the cavity. Only in the bottom corner some liquid resides, kept there by surface tensional forces.

Apart from the geometrical alterations to the cavity geometry and the acoustic damping due to droplets, additional acoustic damping due to liquid at the pipe wall and the shear-layer disruption by liquid could also lead to a reduction in acoustic amplitude. To investigate this, a corrugated pipe is produced, with a cavity geometry based on the liquid profiles discussed in this section. The liquid profile that was measured in the pipe with geometry A, at a gas flow velocity of 40 *m/s*, just beyond the point where whistling disappears is used. A pipe is machined with the same length and number of cavities as geometry A, the only difference being the altered cavity geometry. The acoustic output of this pipe is measured over a range of flow settings. No whistling occurred over the entire flow velocity range possible in the experimental setup. This strengthens the conclusion that indeed the alteration of the cavity geometry is the main source of whistling mitigation, as was already anticipated by van Eckeveld et al. (2017).

The cavity filling mechanism also explains the limited amount of liquid required to silence pipes with geometries B, C and E. The reduced dry whistling amplitude and the smaller cavity volume together result in a smaller liquid fraction required to mitigate whistling, compared to geometry A. For geometry E, however, another effect appears concurrently, as will be shown in Section 4.5.3.

Several distinct geometrical alterations are expected to play a role when it comes to the reduction of the acoustic amplitude. The three most important are: (1) a shortening of the cavity shear layer, (2) a change of the upstream cavity edge geometry and (3) an alteration

to the deeper part of the cavity. When the shear layer region becomes shorter, a reduction in the spatial extent of the acoustic source region results in lower acoustic amplitudes. It is also known from literature that rounding of the upstream edge has a strong effect on the acoustic amplitude (Binnie, 1961 and Nakiboğlu et al., 2010). For a sharper upstream edge, the increased wall-normal component of the acoustic velocity field will cause a stronger acoustic absorption at the upstream cavity wall, and hence, a lower acoustic output. Since the liquid acts as a solid wall from the perspective of the gas flow, alterations to the rib rounding by the presence of liquid will lead to different acoustic outputs. Adaptions of the deeper part of the cavities will affect the recirculation zone that is present beneath the shear layer. Because of the interaction between the shear layer dynamics and the recirculation zone (as the recirculation zone introduces disturbances towards the shear layer origin), this might influence the vortex shedding and growth rate, and thereby the acoustics. These effects will be further studied through simulations in the second part of this work (see Section 4.6).

4.5.3 AXISYMMETRY OF FILLING

Another aspect that is important for the acoustic behavior of two-phase flow through corrugated pipes is the axisymmetry of the filling profile. For geometry D, after manufacturing, the pipe wall was covered with oil, resulting in a hydrophobic internal surface. When this pipe is subsequently subjected to an air-water flow, the axisymmetry of the filling is broken. Figure 4.18a shows the resulting filling pattern in a qualitative manner. Small patches of liquid appear at the inner cavity wall, and the liquid accumulation shows a reduced azimuthal regularity, varying significantly in time and space. A similar filling behavior is observed for two-phase flow through a pipe with corrugation geometry E, where the absence of an upstream rectangular inner cavity corner hinders liquid accumulation inside the cavities. Figure 4.18b shows an image taken from the pipe end under these conditions. Small patches of liquid are observed in the cavities. The acoustics generated by a pipe in this flow regime are quite different compared to the axisymmetric regime discussed in the previous sections. Figure 4.19 shows the acoustic amplitude as a function of the liquid volume fraction for the two regimes in geometry D, at a superficial gas velocity of 42 *m/s*. When the filling is non-axisymmetric in nature, whistling disappears at a substantially lower liquid volume fraction. The presence of liquid causes an effective change in the corrugation geometry, encountered by the gas flow. Irregularities in this geometry in azimuthal direction can break the coherent nature of the vortex shedding. This process appears to be more effective in whistling mitigation, than the mere filling of the cavities. It is, however, not feasible to manufacture long corrugated pipes with an irregular spanwise corrugation profile. When liquid is added to corrugated pipes it is possible to break the axisymmetry of the corrugations. Treatment of the pipe walls resulting in a large contact angle with the working liquid would, for example, cause a reduction in the required amount of liquid for whistling to disappear. Cavity geometries preventing the formation of an azimuthally continuous liquid filling (like geometry E) are expected to result in similar reduction in the required liquid volume fraction to suppress whistling.

(a) (b)

Figure 4.18: Qualitative view of the filling pattern for a corrugated pipe with geometry D after hydrophobic wall treatment (a), and geometry E (b). Liquid addition does not result in an axisymmetric filling in these cases, but rather appears as small patches of liquid inside the cavities.

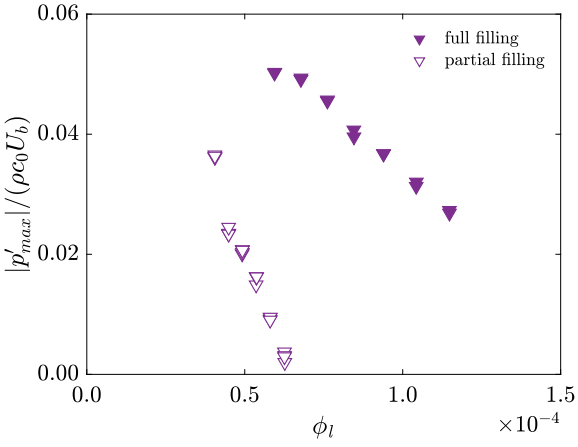

Figure 4.19: Dimensionless whistling amplitude as a function of the liquid volume fraction, for two-phase water-air flow through a pipe with corrugation geometry D. When the axisymmetry of the filling is broken due to a non water-wetting coating of the wall (open markers), the required liquid volume fraction to make whistling disappear is substantially reduced.

4.6 WHISTLING IN CORRUGATED PIPES - NUMERICAL

Although qualitative and quantitative information is obtained from the whistling experiments in different geometries, many factors are still intertwined and remain unclear. Without flow-field information, it is therefore difficult to isolate the generated acoustic power for the different geometries from the acoustic properties of the entire pipe system. Furthermore, the effect of changes to specific parts of the cavity geometry cannot be identified easily from the experiments. To isolate the acoustic source power and to investigate which specific parts of the geometry play an important role, a numerical model solution is used. This method is based on the work by Martínez-Lera et al. (2009), Nakiboğlu et al. (2010) and Golliard et al. (2013b). The validity of the method is first assessed, after which a modification is proposed that provides more insight in the whistling cycle in corrugated pipes.

The numerical method is based on incompressible flow simulations. The main flow structures that are responsible for the sound generation are the vortices shed in the cavity mouth. These large flow features can be captured in a 2D-axisymmetric incompressible simulation. Since acoustics cannot exist in incompressible simulations, an acoustic analogy is applied to obtain the acoustic power generated by the flow through a certain geometry. The shedding of vortices is triggered by superimposing a fluctuating component to the incoming velocity profile. It is applied at the pipe inlet, located 2 *mm* upstream of the leading cavity edge. A uniform perturbation amplitude is used, as the acoustic boundary layers are typically very small (of the order of the viscous sublayer). This fluctuating velocity perturbation mimics the acoustic standing wave that develops in real corrugated pipes, and that synchronizes vortex shedding in the individual shear layers. Hydrodynamic interaction between subsequent cavities is not taken into account. A single cavity in a pipe is modeled, omitting the interference effect between subsequent cavities. Figure 4.20 shows the numerical domain used in the simulations, in this case for geometry A (see Figure 4.4). The cavity zone is densely meshed, especially near the cavity mouth. Grid sizes reduce towards the wall, where a y^+ value around 1 is maintained. The total number of quadrilateral cells ranges from 55000 to 77000 depending on the cavity geometry. A grid dependence study showed little differences for higher numbers of grid cells (up to over 200000). For the URANS simulations the $k-\omega$ turbulence model is applied.

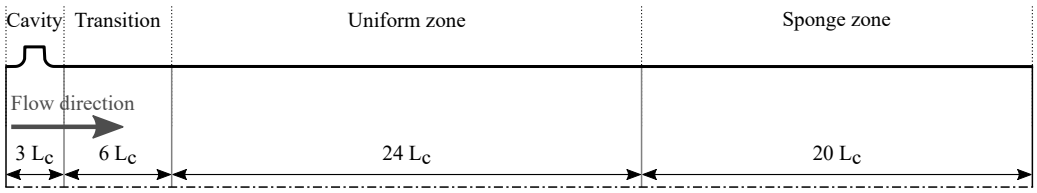

Figure 4.20: Numerical domain used for simulations of the cavity with geometry A. The cavity zone is densely meshed, followed by a transition to a uniform grid size. The sponge zone is applied to reduce reflections from the outlet.

4.6.1 NUMERICAL METHOD

As a starting point for the calculation of the acoustic source power, Howe's theory of vortex sound is used (Howe, 2003). This theory is derived from Crocco's momentum equation. For a homentropic flow, ignoring viscous contributions to the flow (valid for high Reynolds numbers), Crocco's equation is written as:

$$\boldsymbol{\nabla} h_t = -\frac{\partial \boldsymbol{u}}{\partial t} - (\boldsymbol{\omega} \times \boldsymbol{u}), \tag{4.28}$$

where h_t is the stagnation enthalpy and $\boldsymbol{\omega}$ the vorticity. Combining this equation with Howe's energy corollary (see Equation 4.27), yields an equation for the acoustic source power:

$$\langle P_{source} \rangle = -\rho \left\langle \int_V (\boldsymbol{\omega} \times \boldsymbol{u}) \cdot \boldsymbol{u}'_{ac} dV \right\rangle, \tag{4.29}$$

$$= \rho \left\langle \int_V \nabla h'_t \cdot \boldsymbol{u}'_{ac} dV \right\rangle + \rho \left\langle \int_V \frac{\partial \boldsymbol{u}}{\partial t} \boldsymbol{u}'_{ac} dV \right\rangle. \tag{4.30}$$

In this equation, h'_t is the fluctuating part of the total enthalpy. The second right hand side term of Equation 4.30 is neglected. Applying the divergence theorem, knowing that $\nabla \cdot \boldsymbol{u}'_{ac}$ is negligible in a compact source region, results in a formulation of the acoustic source power related to the fluctuating total enthalpy:

$$\langle P_{source} \rangle = \rho \left\langle \int_S (h'_t \boldsymbol{u}'_{ac}) \cdot \vec{n} dS \right\rangle. \tag{4.31}$$

By choosing a large control surface, ensuring that hydrodynamic fluctuations are insignificant at the downstream boundary, the second right hand side term of Equation 4.30 can indeed be neglected (Nakiboğlu et al., 2010). The large control surface, however, also contains a significant smooth pipe length where the effect of the cavity is reduced by viscous dissipation. To isolate the source power, a smooth pipe reference case is subtracted from the obtained result:

$$\langle P_s \rangle = \langle P_{source} \rangle - \langle P_{smooth} \rangle, \tag{4.32}$$

where P_s is the corrected source power. Using this method, it is claimed that the effect of the Reynolds number on the acoustic source power is removed, enabling the use of lower Reynolds number simulations for a higher Reynolds number case (Nakiboğlu et al., 2010). The acoustic source power was overestimated by approximately a factor 2 with this method. Later, Golliard et al. (2013b) carried out a URANS simulation, which extends the applicability of the method to higher Reynolds numbers due to a better representation of the shear layer growth in the cavity region. They claim a significant increase in accuracy of the predicted source power to within 20% of the experimental results.

Instead of using the total enthalpy to obtain the acoustic source power, one can also directly apply Equation 4.29. In that case no smooth pipe reference simulation is required. The only additional demand is that the local distribution of the acoustic velocity field at the location of the cavity is known. Bearing in mind that the acoustic velocity corresponds to the unsteady

potential component of the flow, a separate potential flow simulation is performed to obtain the distribution of $\boldsymbol{u}'_{ac}$. Assuming that the local acoustic field is not significantly altered by the flow, it is subsequently combined with the incompressible URANS simulation of the cavity geometry to obtain the source power. The advantage of this method, apart from omitting the need for a reference simulation, is that it provides insight in the local spatial distribution and temporal evolution of regions of production and absorption of acoustic energy in the cavity. It therefore adds to understanding the effect of specific geometrical cavity alterations to the acoustic output of a certain corrugation geometry. In the following, the two methods will be compared to literature and to each other, after which they are applied to the different corrugation geometries studied in the present work. The two methods are referred to as the *vorticity* (Equation 4.29) and the *enthalpy* (Equation 4.31) method respectively.

4.6.2 COMPARISON OF THE TWO METHODS

To assess the difference between the two methods, the geometry studied by Nakiboğlu et al. (2012a) and Golliard et al. (2013b) is used as a benchmark case. This cavity has a length of 40 *mm* and a depth of 27 *mm*, and is placed inside a pipe with a diameter of 44 *mm*. The cavity edges are rounded and have a radius of 5 *mm*. Gas phase Reynolds numbers based on the pipe diameter of 4×10^3 and 4×10^4 are used. The inlet velocity profile is obtained from Nakiboğlu et al. (2012a) and a moderate perturbation amplitude of $|u'|/U_b = 0.05$ is used.

The results from Nakiboğlu et al. (2012a) are accurately reproduced (as is depicted in Figure 4.21a). Both methods result in comparable values for the peak whistling source power, within 1% of the values reported by Nakiboğlu et al. (2012a). The peak whistling Strouhal number is the same as reported in literature. That the *enthalpy* and *vorticity* methods lead to similar results shows that the second right hand side term in Equation 4.30 is indeed negligible.

For the higher Reynolds number case (Re = 4×10^4) the URANS method (with a $k-\omega$ turbulence model, as was used by Golliard et al., 2013b) is applied, and the results are com-

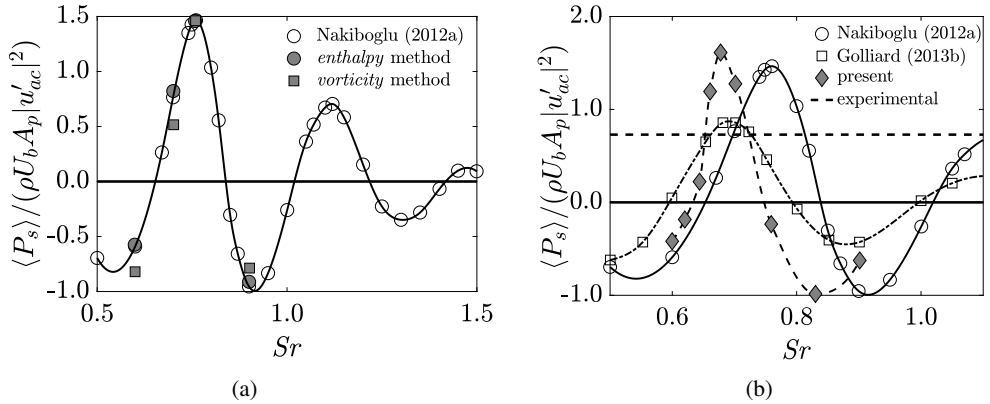

Figure 4.21: (a) Comparison of the dimensionless acoustic source power as a function of the whistling Strouhal number obtained with the *enthalpy* and *vorticity* method, compared to results from literature (Nakiboğlu et al., 2012a; Golliard et al., 2013b) at a Reynolds number of 4×10^3 (a) and 4×10^4 (b). The experimentally obtained source power, depicted in (b), is also taken from Nakiboğlu et al. (2012a).

pared to results obtained by Golliard et al. (2013b) in Figure 4.21b. There is a good agreement with respect to the whistling Strouhal number, however, the obtained source power is almost a factor 2 higher than the value that is reported by Golliard et al. Several differences in the simulations might be causing this discrepancy. First, the incoming velocity profile for the present case is taken from Nakiboğlu et al. (2012a), and there might be slight differences with the velocity profile used by Golliard et al., who do not report the exact profile they used. A significantly different velocity profile would, however, also result in a changed whistling Strouhal number, which is not observed. It is more likely that a difference in perturbation amplitude in the simulations is causing the discrepancy. Golliard et al. (2013b) do not explicitly mention the perturbation amplitude that was used in their study. For the present study a perturbation amplitude of 5% of the bulk velocity is used which is close to the experimental value. For a perturbation amplitude of $|u'|/U_b = 0.10$, a close match between the present method and the results reported by Golliard et al. (2013b) is obtained, suggesting that this is the perturbation amplitude that was used in their study. A grid dependence study (twice the amount of grid points) is carried out and did not result in significant differences.

Both methods are used to assess the source power in geometry A and D (see Figure 4.4). The amplitude of the source power obtained with the *vorticity* method is always within 8% of that of the *enthalpy* method. Differences in the whistling Strouhal number are even smaller. Using Howe's energy corollary directly has several advantages: it gives direct insight in the temporal and spatial evolution of the acoustic source power, and it omits the requirement of a reference flow calculation and hence, reduces computational demands. This method is therefore used in all the cases considered in the following.

4.6.3 REFERENCE CASE GEOMETRY A

The cavity geometry A is used as a reference case, to evaluate the accuracy of the URANS simulation compared to acoustic data from experiments. The gas flow velocity is taken as 40 *m/s*, and the incoming velocity profile for this geometry is obtained from a separate periodic URANS simulation in a corrugated pipe, without a velocity perturbation at the inlet. The resulting velocity profile closely resembles a power law profile, with a power of 4.8 (White, 2017). This profile is subsequently used as the inlet velocity profile for all simulations. The time-averaged acoustic source strength $\langle P_s \rangle$ is obtained over a range of whistling Strouhal numbers by changing the oscillation frequency of the velocity perturbation. The results are depicted in Figure 4.22. When $\langle P_s \rangle$ is positive, sound may be produced. Two peaks are observed, indicating the second and third hydrodynamic modes. The second mode is dominant, while the third mode barely produces any acoustic energy. The amplitude of this sound production depends on the acoustic losses present in the system. Whether a corrugation geometry exhibits whistling in practice will depend on the system that the corrugation is a part of. If the time-average acoustic source power exceeds the acoustic losses of the system, sound will be produced.

Whistling cycle

The acoustic source power generated by a specific corrugation geometry can be evaluated both temporally and spatially using the *vorticity* method. From literature it is anticipated that the main production and absorption regions occur at the trailing and leading edge, respectively. This is due to the synchronization of the vortex shedding cycle with the fluctuating acoustic

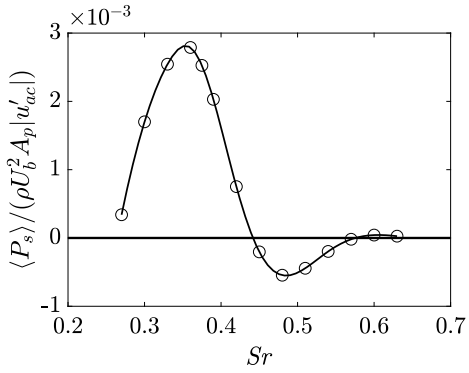

Figure 4.22: Dimensionless acoustic source power as a function of whistling Strouhal number for geometry A, at a perturbation amplitude of $|u'_{ac}|/U_b = 0.1$, and a bulk velocity of 40 *m/s*.

velocity, and a result of the local distribution of the acoustic velocity field. Figure 4.2 shows an impression of the distribution of the acoustic streamlines in this cavity geometry. The temporal variation of the source strength over a single whistling cycle is depicted in Figure 4.23. Two peaks in the source strength occur, related to the minimum and maximum acoustic velocity during an oscillation period. Both peaks are positive due to the sign change of the acoustic field at $t/T = 0.5$. Vortex formation in the shear layer is initiated when the acoustic velocity switches sign, from negative to positive x-direction (Nelson et al., 1983; Bruggeman et al., 1991). This point is indicated by A in Figure 4.23. At this instance, the preceding vortex is present half-way the cavity (as is depicted in Figure 4.24a). The associated source power (Figure 4.24b) is low due to the vicinity of the zero acoustic velocity point ($u'_{ac} \approx 0$). Sound is subsequently produced at the downstream cavity edge when the vortex is convected

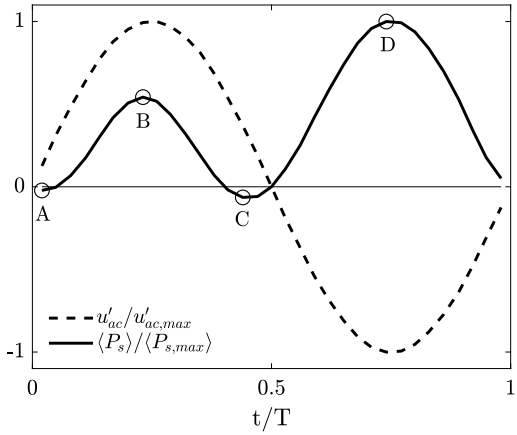

Figure 4.23: Temporal distribution of the source strength (-) and the acoustic perturbation amplitude (–) over a full period of the perturbation cycle at the peak-whistling Strouhal number. The bulk gas velocity is 40 *m/s*, the perturbation amplitude amounts 10% of the bulk velocity. Values are normalized with the maximum values obtained in a whistling period. The points A, B, C and D relate to Figure 4.24.

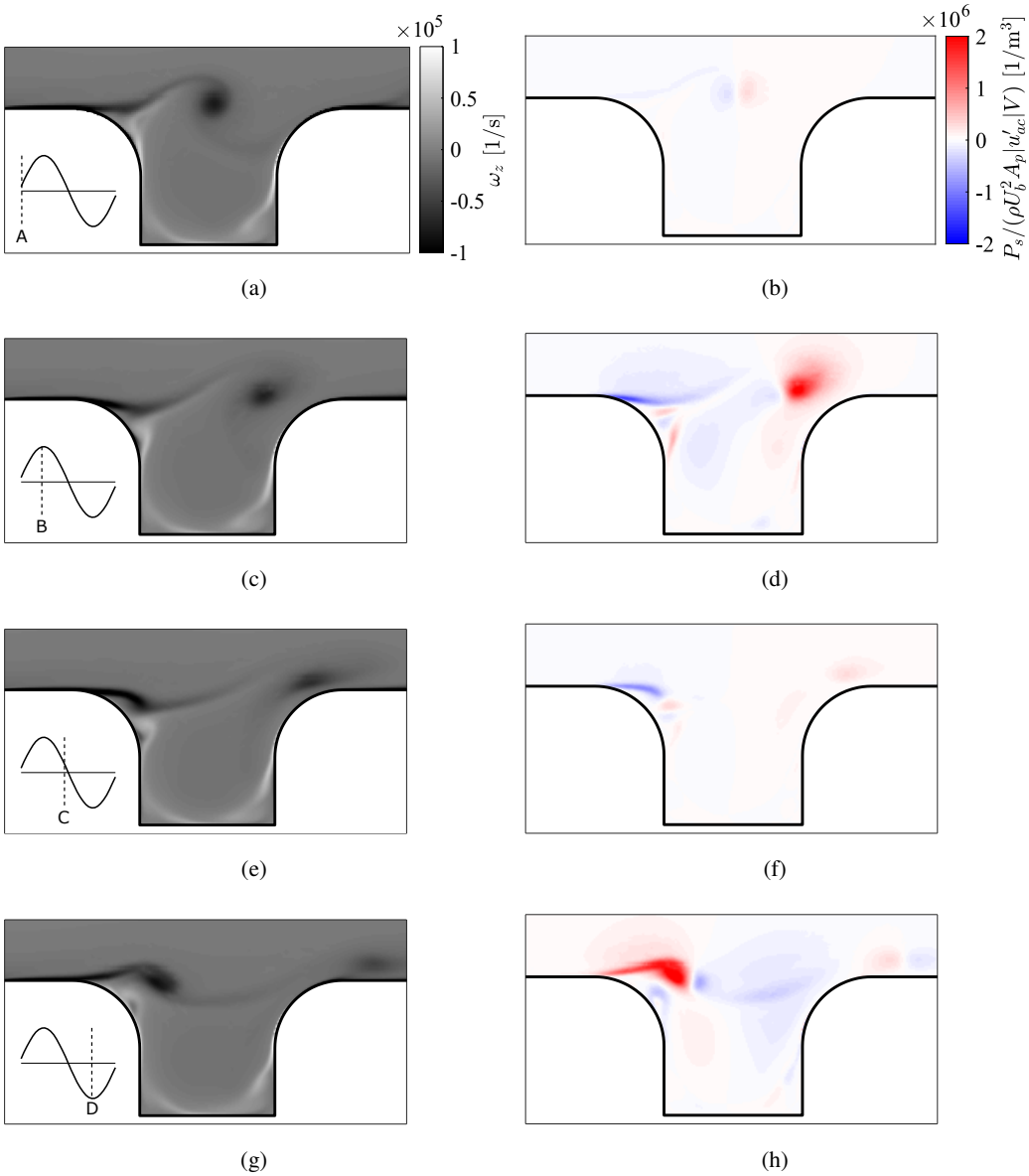

Figure 4.24: Instantaneous vorticity contours (a, c, e, g) and source power contours (b, d, f, h) for the four instances tagged in Figure 4.23 (geometry A). The position in the acoustic perturbation period is depicted in the bottom left of the vorticity contour plots.

further downstream (Figures 4.24c and 4.24d, B in Figure 4.23). Acoustic absorption occurs at the upstream edge simultaneously, caused by the newly generated vortex. When the spatially averaged acoustic source power becomes negative (C in Figure 4.23) the absorption region near the upstream edge is growing, whereas production from the downstream vortex shrinks due to its collision with the wall (Figures 4.24e and 4.24f). The largest instantaneous source power is observed when the acoustic particle velocity is at its negative peak (D in Figure 4.23). Production then occurs in the upstream half of the cavity, as a result of the sign change of the acoustic field (see Figures 4.24g and 4.24h).

The swirling strength criterion (Zhou et al., 1999) can be used to identify individual vortices. Combining the vortex position with the instantaneous source power (as displayed in the right hand side plots of Figure 4.24), the sound production and absorption over the vortex path is obtained. Figure 4.25 shows the instantaneous overall source power, as well as the power generated by the two vortices that are present in the cavity, as a function of time. The perturbation cycle is also depicted. The graph spans 1.5 oscillation period, which is approximately equal to the lifetime of of a vortex in the cavity mouth. The vortex is being generated when the sign of the perturbation velocity switches from negative to positive x-direction. Over the first half fluctuation period, the vortex only absorbs sound. When the sign of the perturbation amplitude switches again, sound is being produced. The vortex travels during this time over the upstream half of the cavity. The source power approaches zero when the perturbation velocity is zero again, after which a second peak in source power is observed when the perturbation velocity is positive again and the vortex is in the downstream half of the cavity. At this point the second vortex is formed at the upstream cavity edge, and the cycle repeats itself.

Averaging of the instantaneous source power over several whistling cycles results in the spatial distribution of absorption and production regions over the cavity. Figure 4.26a shows this spatial distribution for geometry A, at a bulk velocity of 40 *m/s* and a perturbation amplitude of $|u'_{ac}|/U_b = 0.1$. Acoustic power is mainly produced near the downstream edge, and at approximately a quarter of the cavity length. The major absorption region is located at the

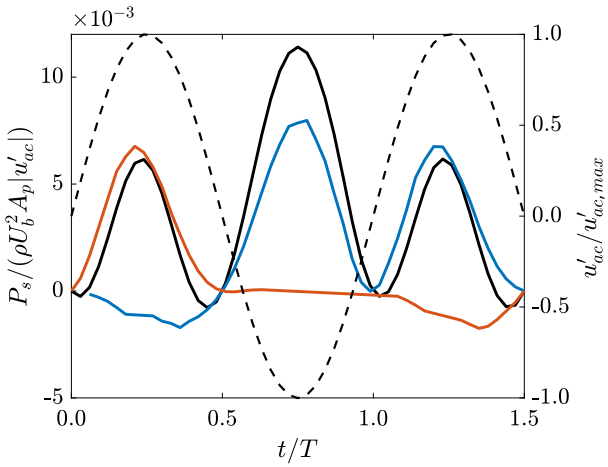

Figure 4.25: Source power of individual vortices (—and —) traveling in the cavity mouth of geometry A as a function of time for a perturbation amplitude of $|u'_{ac}|/U_b = 0.1$. The space-averaged source power is indicated by —. The position in the perturbation cycle is depicted with - - at the right hand side y-axis.

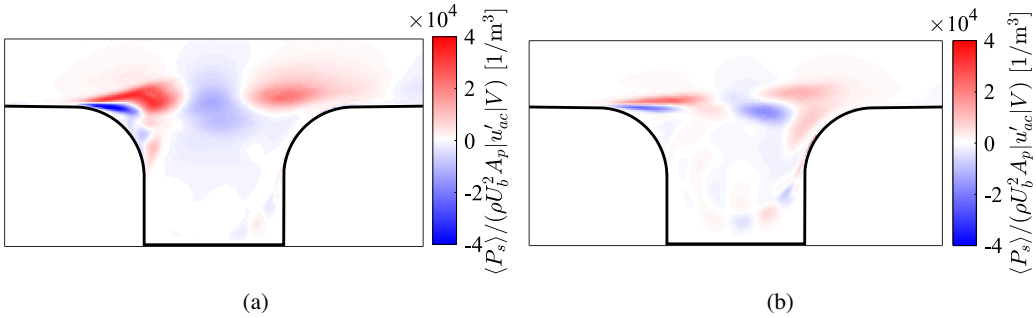

Figure 4.26: Spatial distribution of time-averaged source power for geometry A, at the peak-whistling Strouhal number. The amplitude of the perturbation velocity is $|u'_{ac}|/U_b = 0.1$ (a) and 0.025 (b), for a bulk velocity of 40 *m/s*.

upstream edge, as expected from literature. Halfway the cavity some additional absorption occurs. All significant absorption and production takes place inside the shear layer region. The deeper parts of the cavity do not contribute much to the sound production. It is therefore expected that the internal cavity geometry is not of great direct influence to the acoustic output. Only through a possible change in the shear layer behavior it might affect the sound production, which occurs in shallow cavities. The main geometrical cavity properties that determine the acoustic amplitude (apart from the acoustic properties of the pipe system) are the size of the cavity mouth and the geometry of the cavity edges, particularly of the upstream edge.

Scaling of source power

As discussed in Section 4.2, the source strength behavior strongly depends on the perturbation amplitude $|u'_{ac}|/U_b$. Three regimes are distinguished in literature: the linear regime, the high amplitude regime, and the intermediate regime. From Equation 4.27 it is expected that the net acoustic source power scales with the bulk velocity squared and with the acoustic perturbation velocity, but this only holds when the vorticity in the shear layer is fully concentrated in discrete vortices that convect downstream towards the cavity edge. To evaluate these scaling arguments, simulations are performed at different perturbation amplitudes in geometry A, and at a fixed Strouhal number. The effect of the bulk velocity (or the Reynolds number) is also assessed. Figure 4.27a shows the dimensionless source strength as a function of U_b. The source strength is made dimensionless with U_b^2 and $|u'_{ac}|$. A reduction of the bulk velocity from 40 to 10 *m/s* causes a 30% decrease in acoustic source power, caused by slightly changed vortex dynamics. The perturbation amplitude has a considerably stronger effect (see Figure 4.27b). The relation between $\langle P_s \rangle$ and $|u'_{ac}|/U_b$ seems to be towards a quadratic nature, instead of the linear relation expected in the intermediate amplitude regime. Further study of the vortices occurring at high and low perturbation amplitude reveals that the differences are caused by the effect of the perturbation amplitude on the vortex dynamics. Vortices become less strong and are more diffuse when the acoustic velocity is lowered (compare Figures 4.28a and 4.28b, where vortices are visualized using the swirling strength criterion developed by Zhou et al. (1999)). This effect has also been visualized by for example Peters (1993). Hence, the local vorticity concentrated in the vortex core, is also a function of $|u'_{ac}|$. The main cause for the reduced vortex strength is the postponed onset of vortex formation for lower perturbation velocities. The spatial distribution of the time-averaged source power, depicted in Figure 4.26

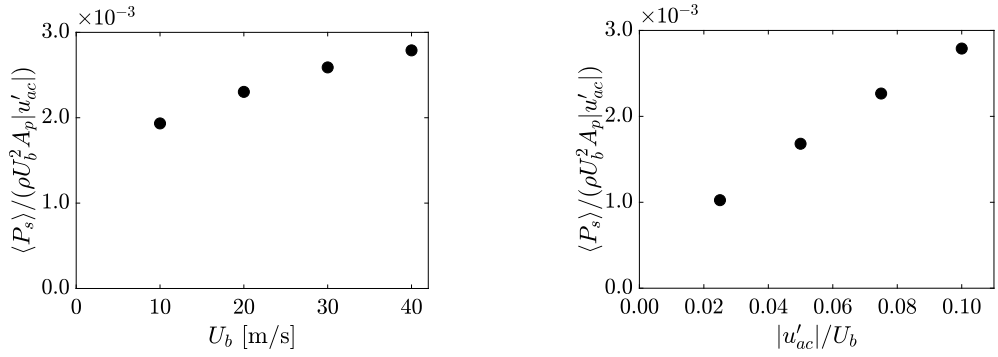

Figure 4.27: Dimensionless acoustic source power as a function of the gas flow velocity (a) and the perturbation amplitude (b).

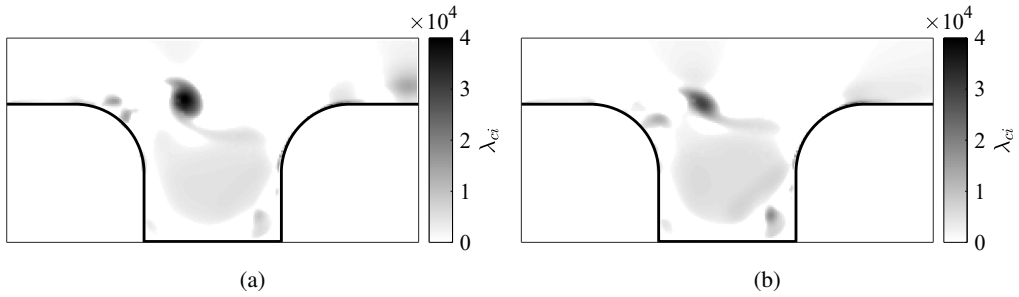

Figure 4.28: Vortices traveling over the cavity mouth, visualized using the swirling strength criterion (Zhou et al., 1999). The amplitude of the perturbation velocity is $|u'_{ac}|/U_b = 0.1$ (a) and 0.025 (b), for a bulk velocity of 40 *m/s*.

reveals this later vortex formation. Whereas for $|u'_{ac}|/U_b = 0.1$ the vortices appear at the end of the rounded upstream edge, for $|u'_{ac}|/U_b = 0.025$ this is postponed to almost halfway the cavity. The regions of absorption and production that co-exist at the upstream cavity edge in Figure 4.26b show that vortex formation is not initiated yet at that position. Smaller disturbances require a longer time to grow and reach the non-linear saturation regime where discrete vortices occur (Ghoniem and Ng, 1987). A steady shear layer with limited disturbances is present in the first part of the cavity mouth. The spatial extent of the production and absorption regions in the downstream half of the cavity is also smaller for lower disturbance amplitudes, as a consequence of this delayed onset of shedding. Not all of the vorticity in the shear layer is, therefore, concentrated in the discrete vortices. This is a requirement for the linear scaling to hold. At the present conditions the scaling is somewhere between the linear and the quadratic regime.

Comparison to experiments

The numerical results can be compared to the measurements reported in Section 4.4. The peak-whistling Strouhal number for geometry A equals 0.36, both for the experiments and simulations. The dimensionless acoustic source power is, however, significantly higher than

expected from the measurements reported in Figure 4.9 (2.8×10^{-3} versus 0.8×10^{-3}). This value is based on an estimation of the acoustic damping in the pipe system, making use of an energy balance model, and is a factor 4 lower than the numerically obtained value. It should be noted that the actual whistling amplitude in the experiments at $U_b = 40$ *m/s* is close to 5% of the bulk gas flow velocity, instead of the 10% used in the simulations. The effect of the perturbation amplitude on the dimensionless acoustic source strength is depicted in Figure 4.27b and is discussed before. When the experimental fluctuation amplitude is used as input to the simulations, the dimensionless acoustic source strength reduces to 1.47×10^{-3}, which is approximately 1.5 times the experimental value. Previous studies found a similar discrepancy between experimental and numerical values for the source power (Nakiboğlu et al., 2012a). Furthermore, in the derivation of the acoustic source strength, it is assumed that the source strength scales linearly with the perturbation amplitude to arrive at Equation 4.6. It is shown in previously that this scaling is close to quadratic. Assuming that $P_s = f(|u'_{ac}|^1.5)$, the resulting source strength would be approximately 13% lower, bringing the experimental and numerical results closer together. Nonetheless, a difference remains, which is caused by both the simplifications in the model, and the assumptions made in the calculation of the acoustic losses in the experimental setup. Important to note is that the close to quadratic scaling of the source power with the acoustic amplitude complicates the comparison of experimental and numerical results using the EBM presented in Section 4.2.1. A slight change in source power or acoustic losses results in a large difference in whistling amplitude. The focus will therefore be on a comparison of the trends obtained form experiments and numerical simulations.

4.6.4 CAVITY GEOMETRY

Simulations are carried out for all geometries depicted in Figure 4.4, at a range of whistling frequencies. The peak whistling Strouhal number for the different geometries shows good agreement with the experimental values, as is shown in Table 4.2. The largest difference occurs for geometry B, and amounts 10%, while the other geometries show results closer to the experimental value. The average error for all geometries is around 5%.

Figure 4.29 shows the acoustic source power at the peak-whistling Strouhal numbers. The source power is overestimated for all geometries, as was also found for geometry A. The absolute values of the source power are a factor 1.5-2 higher in the simulations (Figure 4.9), except for geometry B where the numerical results amount three times the experimental value. Trends with respect to geometry A, however, are rather similar. Geometry D results in the highest source power, related to the increased spatial extent of the source region. Geometries C and E are very comparable, with triangular cavity E resulting in the lowest whistling amplitude. The reference geometry A is somewhere between C and D. Only for the shallow geometry

Geom	A	B	C	D	E
Sr_{pw} experimental [-]	0.36	0.30	0.28	0.41	0.35
Sr_{pw} numerical [-]	0.36	0.33	0.30	0.42	0.32
% change	0%	+10%	+7%	+2%	-8%

Table 4.2: Comparison of the peak whistling Strouhal numbers for the geometries depicted in Figure 4.4.

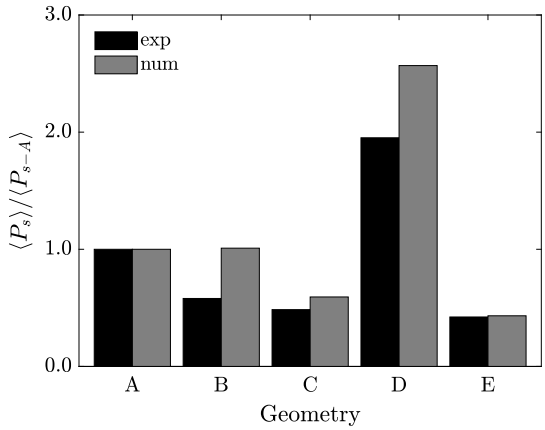

Figure 4.29: Normalized acoustic source power obtained from URANS simulations and experiments, for the different geometries listed in Figure 4.4 and Table 4.1.

B the numerical trend deviates from the experiments. The numerical source power for this geometry matches that of the reference geometry, whereas in the experiments, it whistled at significantly lower amplitudes. Nakiboğlu et al. (2012a) also observed that for shallower cavities the numerical results deviate from the experiments. To capture the shear layer behavior for high length-over-depth ratio cavities URANS simulations are not deemed sufficient.

Literature reports that the geometry of the upstream cavity edge has a strong influence on the acoustic output. In Section 4.5 it is shown that this upstream edge is strongly altered by the presence of liquid. To assess the consequences of changed edge radii, simulations are carried out with the geometries depicted in Figure 4.30. Geometries A_{2-4} are inspired by the reference geometry A, but have sharp upstream or downstream edges. The numerically obtained acoustic source power for these geometries is shown in Figure 4.31. By sharpening the upstream edge (A_2) the acoustic source power is greatly reduced. When this geometry is inverted (A_4), now with the sharp edge at the downstream side, the source power is similar to that of geometry A, and even slightly increased. A sharper edge results in a locally increased acoustic velocity. If this occurs at the upstream edge, the acoustic absorption region is intensified (compare Figure 4.26a). This effect is quite strong, due to the localized vortex at the upstream edge. The opposite happens if the downstream edge is sharp. The production region at this edge increases in strength. It is only slightly increased due to viscous spreading of the vortex over the length of the cavity. Sharpening the upstream edge results in an effectively

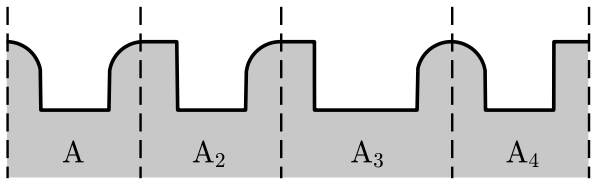

Figure 4.30: Geometries based on geometry A, used to assess the effect of edge rounding on acoustic the source power.

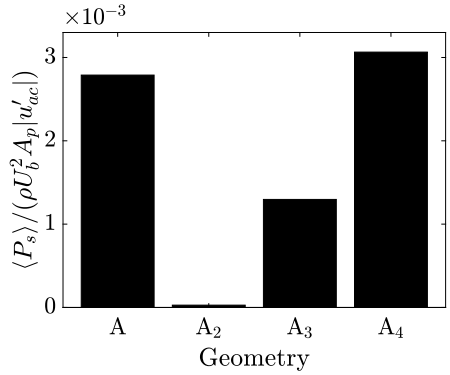

Figure 4.31: Peak whistling acoustic source power obtained for the geometries depicted in Figure 4.30

shortened cavity, as the shear layer separation point in geometry A is located just after the onset of the curvature. The cavity is therefore longer than only L_c, and rather has a length of $L_c + r_{up}$, as is the case in geometry A_3. This cavity is similar to A_2, but its length is added with the upstream edge radius of geometry A. Still a 50% reduction of acoustic source power is observed in Figure 4.31, substantiating the importance of the upstream edge radius.

4.6.5 LIQUID CAVITY FILLING - NUMERICAL

From the PLIF experiments, described in Section 4.3.3 the profile of the liquid filling inside the cavities is obtained. To evaluate the effect of filling on the acoustic source strength, experimental filling profiles for geometry A are used as an input for the numerical simulations. The gas-liquid interface is modeled as a solid wall, which is justified by the large difference in typical time scales for the gas and the liquid phase. The experimental filling profile is averaged in time and space, and is assumed to be axisymmetric. For a gas flow velocity of 40 *m/s*, the filling profile at three different liquid flow rates is used. Figure 4.32a shows the source power obtained from experiments, for different liquid volume fractions ϕ_l. The *energy balance model* is used to obtain those values (see Section 4.2.1) Point C1 in this figure is the dry reference case, and points C2, C3 and C4 are the liquid filling cases that are studied numerically. It should be noted that for case C4, no whistling is observed in the experiments. Figure 4.32b shows the acoustic source strength obtained from simulations, as a function of the perturbation amplitude for the four different filling profiles indicated in Figure 4.32a. The source strength is significantly reduced when the filling increases. Going from an empty cavity to the cavity at $\phi_l = 5.4 \times 10^{-5}$, it is reduced by almost a factor two.

The source strength from the URANS simulations is subsequently evaluated at the respective experimental whistling amplitude. Since the numerical source strength is always significantly higher compared to the experimental values, trends are compared here. Figure 4.33 shows the normalized source power from experiments and numerical simulations, for different liquid volume fractions. A good agreement is found between the experimentally and numerically obtained trends in Figure 4.33. In both the experiments and the simulations the source strength is reduced to around 25% of its reference value for a liquid volume fraction of 3.6×10^{-5}.

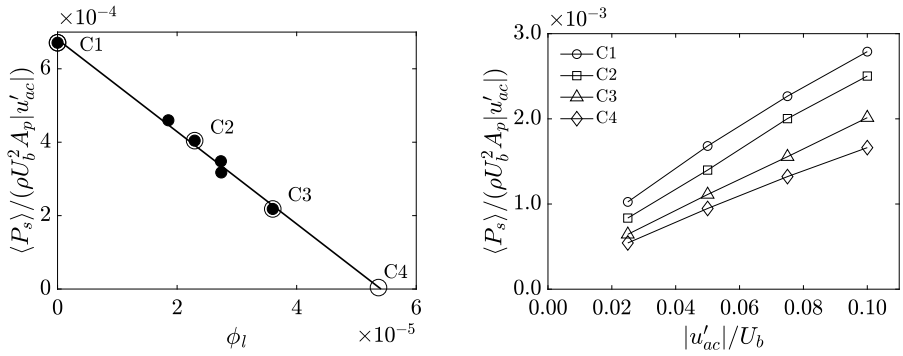

Figure 4.32: (a) Acoustic source strength obtained from experiments with corrugation geometry A, versus the liquid volume fraction ϕ_l. The bulk gas flow velocity U_b is 40 *m/s*. Experimentally obtained filling profiles (as displayed in 4.17a) for four values of the liquid volume fraction are used to numerically obtain the source strength. C1-4 are the fill fractions that are used in the simulations. (b) The numerically obtained source strength as a function of the dimensionless acoustic perturbation amplitude, for the cases C1-4 indicated in (a).

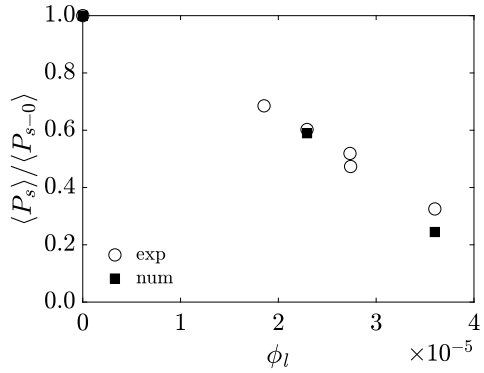

Figure 4.33: Comparison of the normalized source power obtained from experiments and single phase simulations, as a function of liquid volume fraction for geometry A at a gas flow velocity of 40 *m/s*.

Important to note is that the filling profile on top of the ribs separating the cavities is not measured (see Figure 4.17a), and that the profile is extrapolated from the filling inside the cavities. En example of this extrapolation is shown in Figure 4.34. Furthermore, axisymmetry is assumed and a regular filling profile in axial direction. In reality this spatial regularity and temporal stability does not necessarily hold, which might cause differences between experimental and numerical results. Nonetheless, a good agreement of the declining normalized source power is obtained in Figure 4.33.

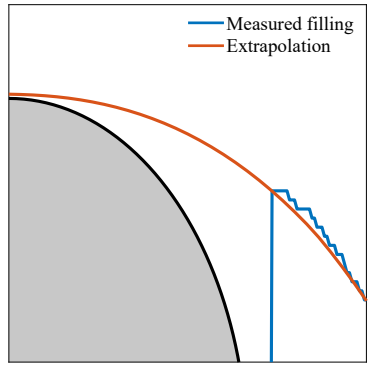

Figure 4.34: Example of the extrapolation used at the upstream cavity edge for case C3 in Figure 4.32a

4.7 DISCUSSION

Several mechanisms are proposed in literature that could cause whistling mitigation in corrugated pipes by means of liquid addition. The most important mechanisms are:

- liquid cavity filling,
- acoustic damping due to the presence of droplets,
- shear layer disruption by liquid fragments.

In previous work, focusing on a single corrugation geometry, it was proposed that liquid cavity filling is the major mechanism for whistling mitigation (van Eckeveld et al., 2017). The liquid filling fraction (α) was used as the critical parameter, identifying to what extent the acoustic amplitude would be reduced. Droplet sizing measurement confirm that the acoustic damping due to the dispersed liquid phase is marginal, despite the very large liquid entrainment ratio in corrugated pipes compared to smooth pipes (van Eckeveld et al., 2018). Furthermore, a corrugated pipe with a geometry similar to a liquid-filled cavity did not exhibit whistling in single phase conditions. Also the numerical results for geometry A with different liquid filling profiles support this. A similar reduction in source power is obtained from single-phase simulations, where only the cavity geometry is copied from the experiments. The presence of liquid in other regions of the pipe is not critical, as the main reduction is caused by the changed cavity geometry. Experiments with different cavity geometries (A and D) and different injected liquids (water and mono-ethylene glycol) show that the liquid filling fraction in itself is not sufficient to fully explain the reduction in whistling amplitude. Especially for

water addition to geometry D and MEG addition to geometry A (Figures 4.15 and 4.14b, respectively) a considerable spread of the critical value for α at which whistling disappears is observed. In general it holds that at higher gas flow speeds a smaller liquid filling of the cavities is sufficient to mitigate whistling. For geometry D (Figures 4.15 and 4.16c) the spread in α at which whistling disappears is considerable: from $\alpha = 0.55$ at $U_b = 25$ *m/s* to $\alpha = 0.35$ at $U_b = 35$ *m/s*. For higher gas flow rates even lower critical filling fractions are expected. Figure 4.16c shows the liquid filling profiles at the point of total whistling mitigation. The main difference is observed in the deeper part of the cavity, where the filling occurs in streamwise direction. In the cavity mouth, which is the actual source region, the profiles are very similar. The behavior of liquid in this region seems to be essential for the sound source amplitude. The deeper cavity part does not contribute significantly to the whistling. The filling fraction α, however, does reflect alterations of this deeper cavity part as well and is therefore not representative for the whistling mitigation. For geometry A, these observations also hold, but are less apparent. At full whistling mitigation the filling inside the cavity mouth decreases in extent when the gas flow rate increases. This is caused by the decreasing whistling amplitude for increasing flow velocity in dry conditions (see Figure 4.7b). At higher gas flow velocities, the point of whistling mitigation is therefore reached more easily. For geometry D this decrease in whistling amplitude at higher frequencies is less apparent, since the acoustic losses at the pipe ends are relatively smaller due to an increased source strength and a lower whistling frequency. For all cases it holds that a liquid filling of 60% of the cavity volume is sufficient to mitigate whistling entirely.

The numerical results underline these findings. The biggest contribution to sound production and absorption occurs in the cavity mouth. The deeper part of the cavity does not contribute significantly to the source power. Apart from the gas flow velocity and the perturbation amplitude, it is mainly determined by the shape of the upstream cavity edge and the spatial extent of the cavity mouth.

The results for the whistling behavior as a function of the cavity geometry can be combined with previous work on the two-phase flow behavior in corrugated pipes (Chapter 3 and van Eckeveld et al., 2018). In that study, a relation between global flow parameters and local filling behavior is obtained for the cavity geometries also used in this study (geometry A and D). The Weber number and film Reynolds number are used in this scaling. These parameters are defined as:

$$We = \frac{\rho_g U_b^2 L}{\sigma} \qquad \text{and} \qquad Re_f = \frac{\rho_l u_{sf}(1-L)}{\mu_l}, \tag{4.33}$$

where L is the empty cavity length, defined as $L = (1-\alpha)L_c$, σ is the interfacial liquid-gas tension, and u_{sf} is the superficial film velocity. The liquid cavity filling then scales as: $(1-\alpha) = f(We^{1.25} Re_f^{-0.25})$. Without prior knowledge of the amount of liquid entrainment, which would require additional measurements, the film Reynolds number cannot be defined. Instead, the liquid Reynolds number Re_l can be used as a rough approximation, which is based on the superficial liquid velocity. Using this parameter results in an increased scatter of the data around the scaling law. This scaling law can be used to predict the liquid flow rate required to mitigate whistling in the corrugated pipe. The larger scatter results in an increased uncertainty of the predicted flow rate. From the previous work it is also known that the liquid viscosity is of minor influence on the filling behavior, which is determined by

a balance between incoming liquid flux and the entrainment rate from the liquid inside the cavity. The shape of the liquid surface for a certain filling ratio is determined by the dynamic balance between surface tension, gravity and inertial forces exerted by the gaseous internal cavity flow.

4.8 CONCLUSIONS

Experiments are carried out to assess the effect of liquid addition to vertical upward corrugated pipe flow. In particular, the consequences for the whistling behavior observed in these flows is studied. Single-phase whistling in pipes with several corrugation geometries is measured, and follows trends generally observed in literature. The corrugated pipe with shorter cavities and a longer plateau length (defined in Figure 4.4) displayes a significantly delayed onset of whistling. The relative increase of acoustic losses due to the longer plateau, the decreased size of the source region, and the higher whistling frequencies cause this augmented onset velocity. The triangular geometry, oriented with the slanted edge at the downstream side does not exhibit whistling in the studied parameter range, whereas in the inverse orientation whistling is observed for this geometry. The interaction of the vortices traveling in the cavity mouth and the slanted bottom at the downstream end results in a reduced acoustic production region, whereas the absorption region at the curved upstream edge is stronger compared to the inverse direction. This results in a net reduction of acoustic source power when the slanted edge is located at the downstream side of the cavity. A decrease in cavity depth-over-length ratio results in a smaller whistling Strouhal number due to the vortex-cavity bottom interaction, which also results in a reduction of the whistling amplitude.

The whistling amplitude is compared between the different geometries using an energy balance model. This model accounts for the altered acoustic losses at various whistling amplitudes and frequencies, and the number of cavities along the pipes. The largest cavity geometry gives the highest source power, due to an increased spatial extent of the source region. The triangular cavity has the lowest source power, mainly caused by the changed acoustic field w.r.t. the rectangular cavity and the vortex wall interaction at the downstream side.

When liquid is injected into the gaseous pipe flow, the whistling amplitude reduces linearly with increasing liquid volume fraction ϕ_l. The liquid volume fraction required to mitigate whistling entirely, increases with increasing gas flow rate for both the reference and the enlarged cavity geometry. The shallow cavity geometry is completely silenced even for the lowest liquid loading. For the short and triangular cavities, no whistling is observed for $\phi_l > 1.5 \times 10^{-5}$, due to the reduced cavity size and different filling properties. Monoethylene glycol (MEG) injection gives comparable results as water injection. MEG injection leads to a slight increase of liquid loading required to reach the same whistling amplitude reduction as is achieved with water injection. The effect of the viscosity is very limited, and the differences are mainly caused by the lower surface tension of MEG.

It is shown that additional acoustic damping due to the presence of a dispersed liquid phase in the bulk flow of the pipe does not contribute significantly to the reduction of whistling amplitude reduction. Measured droplet size distributions are combined with the theory of acoustic damping by a dispersed phase. The resulting increase in acoustic damping only explains 0.01% of the required damping.

Cavity filling is the crucial mechanism determining whistling mitigation in corrugated pipes. The liquid filling fraction α of the cavities was previously used as the critical param-

eter. For different cavity geometries and liquids, however, whistling reduction is not linked directly to the filling fraction α. Rather, it is related to liquid present in the cavity mouth and the associated alteration of the cavity edge geometry. The large differences in the value of α at which whistling disappears mainly occur in the deeper part of the cavity, whereas the filling inside the cavity mouth is very similar. The presence of liquid is not a prerequisite to mitigate sound production. The geometrical change of the corrugations through the presence of liquid is, as is shown in single phase experiments. There are two main parameters that determine the source strength of a cavity geometry filled with liquid: the curvature of the upstream cavity edge, and the length of the cavity mouth.

The axisymmetry of the filling inside the cavities is also of major importance. It is shown that the liquid volume fraction required for whistling to disappear is reduced by a factor three when the filling is not continuous in azimuthal direction. Further research is required to evaluate this effect in more detail.

A numerical method is used to gain more insight in the whistling cycle for different geometries. It consists of a 2D-axisymmetric incompressible URANS simulation, where vortex shedding is triggered by a velocity perturbation at the upstream boundary condition of the numerical domain. A separate potential flow solution for the same cavity geometry is used to calculate the acoustic velocity field. The results of both simulations are used in Howe's energy corollary to obtain an estimated sound source power. Reference results obtained with this method are very similar to values reported in literature using different methods. The advantage of the present method is that it provides more insight in the whistling cycle, and the spatial and temporal evolution of regions of acoustic production and absorption.

The largest contribution to the source power is observed when a vortex travels in the upstream half of the cavity. At this point, where the perturbation amplitude is at its negative maximum, the vortex is strong and compact. At the positive maximum of the acoustic cycle, the vortex is located in the downstream half of the cavity and also produces sound. Since it has already undergone some viscous spreading, it is less localized and therefore produces a lower peak in source power. The effect of a reduction of the perturbation amplitude is mainly displayed through a delayed onset of vortex shedding, resulting in smaller and more compact vortices and, hence, a reduced production of acoustic power in the upstream half of the cavity. The source power shows a near quadratic scaling with both the perturbation amplitude and the bulk gas velocity.

Assessing the different geometries numerically results in similar trends compared to the experiments. Only results for the shallow cavity geometry deviate from the trend. It is reported in literature that comparable numerical methods have difficulties at low depth-over-length ratio cavities, and should not be applied for such geometries. In absolute terms, the source power is over-predicted by approximately a factor two in all cases. This is an acceptable over-prediction, given the simplicity of the method. The whistling Strouhal number is predicted to within 10 % from the experimental values for all geometries.

A negative correlation is found between the filling fraction and the acoustic source power in the simulations. The negative trend closely resembles experimentally obtained trends, underlining the conclusion that filling of the cavities with liquid is the principal mechanism determining whistling amplitude reduction in corrugated pipes with liquid addition. The effect of the axisymmetry of filling and different cavity shapes requires further study, as well as the behavior of the filling profiles as a function of global flow parameters.

5

CONCLUSIONS AND PERSPECTIVES

In this thesis, flow-induced noise in corrugated pipes is studied. Different experimental methods are applied, and provide new insight in the whistling phenomenon in corrugated pipes and the mitigation of whistling by liquid addition. Each chapter is based on a publication and is self-containing. Only general conclusions are provided in this chapter, followed by an outlook to future work and a summary of open questions that still remain.

5.1 CONCLUSIONS

Whistling mitigation in existing corrugated pipes can be achieved using liquid injection. A linear relation is found between the liquid volume fraction inside the pipe and the reduction in whistling amplitude. An increase in the liquid injection rate yields a decrease in whistling amplitude. This behavior is verified for different corrugation geometries and with water and mono-ethylene glycol as injected liquids. An increase in the gas flow speed, or Mach number, yields a higher amount of liquid required to maintain the same reduction in acoustic amplitude.

It is verified that this whistling mitigation is not caused by the presence of droplets in the gaseous core of the pipe flow. Although the liquid entrainment ratio is rather high (80-95%) in corrugated pipes under whistling conditions, the additional acoustic damping is not sufficient to explain the amplitude reduction of the produced acoustics. Droplet size distributions are measured using a combination of *shadowgraphic particle imaging* and *interferometric particle imaging*, and the acoustic damping associated with the droplets present in the pipe flow explains $\ll 1\%$ of the reduction in whistling amplitude (using conservative assumptions). It is, therefore, rather insignificant for whistling mitigation in corrugated pipes.

The filling of the cavities of a corrugated pipe with liquid is identified as the main cause for whistling mitigation. Instead of increasing the acoustic damping in the system, it causes a reduction of the acoustic source strength, by altering the geometry of the corrugations. Due to larger density and viscosity of the liquid inside the cavities, the typical time scales at the liquid side are much lower, compared to the gas side. From the perspective of the gas flow, the liquid acts as a solid wall, effectively changing the geometry of the cavities at the pipe wall.

Since sound originates from the interaction of the unsteady shear layers and the acoustic flow field in the pipe, a geometrical change can lead to amplitude reduction in two different manners. The shear layer dynamics can be influenced directly by a different cavity geometry. This occurs, for example, for shallow cavities, where the interaction between the shear layer and the internal cavity flow is stronger. Also for cavities with inclined downstream edges the shear layer dynamics are affected directly. Vortices are ejected from the cavities, and a lower mass injection at the downstream side of the cavities is expected. Both these cavity geometries are studied in dry conditions and do show a significantly altered acoustic behavior. They are also silenced at very low liquid volume fractions ($\phi_l < 1.5 \times 10^{-5}$). A shorter cavity leads to a reduction of the residence time of vortices, before colliding with the aft cavity wall. This yields a higher whistling frequency, as is observed in the present work. Apart from a modified shear layer behavior, the distribution of the acoustic field also affects the noise levels produced from a corrugated pipe. Following Howe's energy corollary, it is confirmed that the upstream edge geometry is of particular interest when it comes to sound production. The PLIF measurements inside transparent parts of the corrugated pipes reveal that liquid accumulates towards the upstream edge of the cavities, in vertical upward flow. This is not only due to gravity, but also a result of the topology of the internal cavity flow, pushing liquid in that direction. The distribution of the potential acoustic flow field over this altered cavity geometry

is, therefore, mainly affected at the upstream cavity edge, and has a potentially large influence on the resulting whistling amplitude. Larger cavities require higher liquid fractions to achieve the same amplitude reduction, resulting from the larger volume that has to be filled with liquid and the higher acoustic source strength in single phase conditions. A 16-fold increase of the liquid viscosity (going from water injection to mono-ethylene glycol injection) results in a very small change in acoustic behavior of the corrugated pipe, indicating that the viscosity of the injected liquid does not play a cardinal role. A corrugated pipe with a cavity geometry based on the liquid profiles measured in non-whistling conditions does not exhibit whistling in the studied range of operating parameters, underlining the importance of the cavity filling.

Experiments in corrugated pipes with inclined upstream edges and with more hydrophobic walls show a liquid filling profile that is not axisymmetric. The liquid appears as small packets, moving over the inside cavity wall, spatially isolated form each other. This non-axisymmetric filling is more effective in whistling mitigation, requiring a 2-3 times smaller liquid volume fraction to achieve full whistling mitigation compared to an axisymmetric filling.

The cavity filling is strongly related to the two-phase flow regime in the corrugated pipe. Comparison of the two-phase flow behavior in corrugated pipes and smooth pipes reveal that the presence of wall-cavities strongly augments the liquid entrainment ratio. Whereas in smooth pipes the entrainment is close to zero under the studied operating conditions, in corrugated pipes close to 90% of the total liquid flux is entrained in many cases. A strong correlation is found between the liquid entrainment and the amount of liquid accumulation inside the cavities. For fully filled cavities, where over 80% of the cavity volume is filled with liquid, the entrainment ratio drops considerably. It is argued that the internal cavity flow augments the total entrainment rate. As this internal flow is thought to disappear as a consequence of total filling, the entrainment ratio drops. Still, even at full cavity filling, the amount of liquid present in the core of a corrugated pipe is around 50% of the total liquid flow rate. The presence of the corrugations causes locally a very high film thickness (of the order of the cavity depth), and increases the *waviness* of the film at the wall, leading to more entrainment from this film.

The liquid filling of the cavities is shown to scale with the Weber number, in a similar fashion to entrainment in smooth pipes. The effect of the liquid Reynolds number is reversed, compared to smooth pipes. An increase in the liquid film Reynolds number (Re_f) results in an increase of the filling, and consequently a decrease of the entrainment. This is related to the augmented entrainment from within the cavities which is expected to decrease as the liquid Reynolds number increases.

For corrugated pipe flow in downward vertical direction, the liquid accumulation inside the cavities strongly increases, and no whistling is observed within the studied parameter range. The higher liquid accumulation is caused by gravity acting in the opposite direction, preventing the internal cavity flow from emptying the cavities.

A numerical method is used to assess the effect of specifics of the cavity geometry on the acoustic source strength. It is based on a combination of URANS simulations with Howe's energy corollary. The main difference with previous work is that there is no requirement for a smooth pipe reference simulation and that this method provides more insight in the spatial distribution and temporal variation of regions of acoustic absorption and production inside a cavity. The experimentally obtained whistling frequency is predicted accurately for most cavity geometries. The amplitude is over-predicted by a factor 2-3. Given the simplicity of

the method and the complexity of the acoustics involved such a large deviation is acceptable. Only for shallow cavity geometries the numerical results start to deviate from experiments, most likely due to the interaction of the shear layer and the recirculation zone inside the cavities. To accurately capture this interaction, the smaller scales that are modeled in the URANS should also be simulated. The proposed numerical method is applied to cavities with different liquid profiles based on the cavity filling experiments. The resulting trend in the reduction of the acoustic source strength with increasing liquid injection rate is very similar to the experimental results, confirming that the filling of cavities is the main mechanism causing whistling mitigation by means of liquid addition.

In conclusion, liquid addition to corrugated pipe flow reduces the whistling amplitude and eventually mitigates sound production entirely. The main mechanism behind this whistling mitigation is a reduction of the acoustic source strength as a result of the presence of liquid inside the cavities. The liquid acts as a solid wall for the gas flow and changes the cavity shape. This results in a reduced acoustic source strength, and hence a reduced whistling amplitude.

5.2 PERSPECTIVES ON FUTURE RESEARCH

Whistling mitigation through liquid addition to corrugated pipe flow is a promising for existing installations. Several corrugation geometries are studied in the present work, both in dry whistling conditions and when subject to a two-phase gas-liquid flow. Two of those configurations contained a transparent section, enabling measurements of the liquid accumulation in the cavities. In this study generic cavity geometries are chosen based on practical applications, and at the same time resemble corrugations studied in literature. A natural next step is to extend the present work to cavity structures that more closely resemble actual cavity geometries encountered in industrial applications, and to assess the two-phase flow behavior in this wider range of cavity structures. It is shown that direction of gravity with respect to the flow direction is of significant influence on the whistling mitigation attained. The effect of changes in the inclination angle should be studied. An investigation of the effect of liquid properties with respect to the cavity filling is also recommended. The findings in this thesis (the viscosity is of minor relevance and surface tension and contact angle have a larger effect) should be confirmed for a wider range of flow conditions and corrugation geometries.

Some preliminary measurements carried out in the framework of this thesis showed that the regularity of the filling in azimuthal direction can have a significant effect on the cavity filling. The broken axisymmetry that is observed in rectangular cavities induces secondary flows that change the shear layer dynamics and affect the azimuthal coherence of the ring vortices in the shear layers around the pipe circumference. This results in a significantly reduced acoustic output. Several methods to impede an axisymmetric cavity filling are possible, for example designing a cavity geometry that does not have corners where liquid easily accumulates. Also a hydrophobic wall treatment (in case of air-water flow) or a high contact angle of the liquid with the pipe wall results in packets of liquid attached to the wall, and spatially isolated from each other. Both methods will potentially lead to an irregular filling in azimuthal direction. Further research is required to investigate whether this is indeed a general behavior that can be exploited to promote whistling mitigation in corrugated pipes. If that is confirmed, the design and construction of new corrugated pipes with non-regular cavity structures in azimuthal direction would likely reduce the whistling behavior, even in dry conditions.

Since the specific profile of the gas-liquid interface inside the corrugations is of major importance, and determines the acoustic source strength reduction as a consequence of the liquid filling, the behavior of liquid inside the corrugations requires further study. Although a relation is found between global flow parameters and the liquid filling fraction of the cavities, the specific filling profile is of particular interest. Modeling of this profile is required to predict the sound production from a corrugated pipe subject to a two-phase flow a priori.

The numerical method used in the present work does a reasonable job in predicting the acoustic whistling frequency and amplitude, given its simplicity. The still considerable difference between the numerically obtained source strength and the data retrieved from experiments, however, could be brought in closer quantitative correspondence. A better description of the flow through LES or DNS simulations instead of URANS is expected to solve this discrepancy. A *direct noise computation* (DNC, Bailly et al. 2010) is deemed to expensive at the low Mach number range that is of interest for most applications. Also the fact that a single cavity is simulated instead of a row of consecutive cavities might cause differences between the numerical and experimental results, especially for corrugated pipes with a small plateau length.

Experiments to measure the source strength of certain types of corrugations directly would aid in a more detailed evaluation of the numerical method, and omit the requirement of a model (EBM) to account for acoustic losses in the pipe system. This might even be done for corrugated pipes in two-phase conditions, to confirm the present findings that a reduction of the source strength is the main cause for whistling mitigation. Similar experiments are presented in literature (Golliard et al., 2013a). These experiments, however, are carried out in horizontal corrugated pipes, where the source strength reduction and the increased acoustic damping due to the gas-liquid interface of the stratified flow in the bottom of the pipe are intermingled.

Last, when the atmospheric case is well understood, it is advised to extent the present work to higher operating pressures. In several industrial applications, for example vertical risers in off-shore gas exploration, elevated pressures are encountered and the effect of this pressure increase on whistling mitigation by liquid addition is unknown. It is anticipated that the augmented inertial forces as a consequence of the increased gas density would reduce liquid filling inside the cavities. However, the two-phase flow regime in the pipe is expected to change, and has to be part of the investigation.

BIBLIOGRAPHY

R. J. Adrian and J. Westerweel, *Particle image velocimetry*. Cambridge University Press, 2011.

S. K. Agarwal and M. R. Rao, "Heat transfer augmentation for the flow of a viscous liquid in circular tubes using twisted tape inserts," *International Journal of Heat and Mass Transfer*, vol. 39, no. 17, pp. 3547–3557, 1996.

M. R. Ansari and B. Arzandi, "Two-phase gas–liquid flow regimes for smooth and ribbed rectangular ducts," *International Journal of Multiphase Flow*, vol. 38, no. 1, pp. 118–125, 2012.

C. Arnold and G. F. Hewitt, "Further developments in the photography of two-phase gas-liquid flow," *The Journal of Photographic Science*, vol. 15, no. 3, pp. 97–114, 1967.

B. Azzopardi, "Drops in annular two-phase flow," *International Journal of Multiphase Flow*, vol. 23, pp. 1–53, 1997.

B. Azzopardi and P. Whalley, "Artificial waves in annular two-phase flow," in *ASME Winter Annual Meeting, Chicago, Published in Basic Mechanisms in Two-Phase Flow and Heat-Transfer (ASME)*, 1980, pp. 1–8.

Y. Bai and Q. Bai, *Subsea engineering handbook*. Gulf Professional Publishing, 2012.

C. Bailly, C. Bogey, and O. Marsden, "Progress in direct noise computation," *International Journal of Aeroacoustics*, vol. 9, no. 1-2, pp. 123–143, 2010.

S. Belfroid, J. Golliard, and O. Vijlbrief, "Singing mitigation in corrugated tubes with liquid injection," in *ASME 2013 Pressure Vessels and Piping Conference*. American Society of Mechanical Engineers, 2013.

S. Belfroid, H. Korst, P. van Beek, K. Lunde, I. Eidsvik, F. Hansen, and B. Olsen, "Singing mitigation in an export riser via liquid injection: a field case study," in *ASME 2014 Pressure Vessels and Piping Conference*. American Society of Mechanical Engineers, 2014.

S. Belfroid, N. González Díez, J. Golliard, K. Lunde, and S. Naess, "Damping and source strength characteristics of corrugated pipes: influence gap width," in *Proceedings of the 9th International Symposium on Fluid-Structure Interactions, Flow-Sound Interactions, Flow-Induced Vibration & Noise*, 2018.

S. P. C. Belfroid, D. P. Shatto, and M. C. A. M. Peters, "Flow induced pulsations caused by corrugated tubes," in *ASME 2007 Pressure Vessels and Piping Conference*. American Society of Mechanical Engineers, 2007, pp. 439–447.

R. J. Belt, J. M. C. van `t Westende, H. M. Prasser, and L. M. Portela, "Time and spatially resolved measurements of interfacial waves in vertical annular flow," *International Journal of Multiphase Flow*, vol. 36, no. 7, pp. 570–587, 2010.

R. J. Belt, "On the liquid film in inclined annular flow," Ph.D. dissertation, 2007.

A. M. Binnie, "Self-induced waves in a conduit with corrugated walls ii. experiments with air in corrugated and finned tubes," in *Proceedings of the Royal Society of London A: Mathematical, Physical and Engineering Sciences*, vol. 262, no. 1309. The Royal Society, 1961, pp. 179–191.

M. Bolduc, M. Elsayed, and S. Ziada, "Effect of upstream edge geometry on the trapped mode resonance of ducted cavities," in *ASME 2013 Pressure Vessels and Piping Conference*. American Society of Mechanical Engineers, 2013, pp. V004T04A028–V004T04A028.

J. C. Bruggeman, A. P. J. Wijnands, and J. Gorter, "Self sustained low frequency resonance in low-mach-number gas flow through pipe-lines with side-branch cavities: a semi-empirical model," in *10th Aeroacoustics Conference*, 1986, pp. 86–1924.

J. Bruggeman, A. Hirschberg, M. Van Dongen, A. Wijnands, and J. Gorter, "Self-sustained aero-acoustic pulsations in gas transport systems: experimental study of the influence of closed side branches," *Journal of Sound and Vibration*, vol. 150, no. 3, pp. 371–393, 1991.

W. Burstyn, "Eine neue pfeife (a new pipe)," *Z. Tech. Phys.(Leipzig)*, vol. 3, pp. 179–180, 1922.

L. H. Cadwell, "Singing corrugated pipes revisited," *American Journal of Physics*, vol. 62, no. 3, pp. 224–226, 1994.

L. N. Cattafesta, D. R. Williams, R. C. W, and F. S. Alvi, "Review of active control of flow-induced cavity oscillations," in *33rd AIAA Fluid Dynamics Conference and Exhibit*, 2003, p. 3567.

P. Cermak, "Über die tonbildung bei metallschläuchen mit eingedrücktem spiralgang (on the sound generation in flexible metal hoses with spiraling grooves)," *Phys. Z*, vol. 23, pp. 394–397, 1922.

A. Charogiannis, J. S. An, and C. N. Markides, "A novel optical technique for accurate planar measurements of film-thickness and velocity in annular flows," 2017.

L. Cousins and G. Hewitt, *Liquid phase mass transfer in annular two-phase flow: droplet deposition and liquid entrainment*. AERE, 1968, vol. 5657.

F. S. Crawford, "Singing corrugated pipes," *Am. J. Phys*, vol. 42, no. 4, pp. 278–288, 1974.

N. Curle, "The influence of solid boundaries upon aerodynamic sound," in *Proceedings of the Royal Society of London A: Mathematical, Physical and Engineering Sciences*, vol. 231, no. 1187. The Royal Society, 1955, pp. 505–514.

N. Damaschke, H. Nobach, T. I. Nonn, N. Semidetnov, and C. Tropea, "Multi-dimensional particle sizing techniques," *Experiments in fluids*, vol. 39, no. 2, pp. 336–350, 2005.

P. O. A. L. Davies, "Plane wave reflection at flow intakes," *Journal of sound and vibration*, vol. 115, no. 3, pp. 560–564, 1987.

S. Dequand, S. J. Hulshoff, and A. Hirschberg, "Self-sustained oscillations in a closed side branch system," *Journal of Sound and Vibration*, vol. 265, no. 2, pp. 359–386, 2003.

E. Dokumaci, "Sound transmission in narrow pipes with superimposed uniform mean flow and acoustic modelling of automobile catalytic converters," *Journal of Sound and vibration*, vol. 182, no. 5, pp. 799–808, 1995.

J. W. Elliott, "Corrugated pipe flow," in *Lecture Notes on the Mathematics of acoustics*, M. C. M. Wright, Ed. Imperial College Press, 2005, pp. 207–222.

P. S. Epstein and R. R. Carhart, "The absorption of sound in suspensions and emulsions. i. water fog in air," *The Journal of the Acoustical Society of America*, vol. 25, no. 3, pp. 553–565, 1953.

J. E. Ffowcs Williams and D. L. Hawkings, "Sound generation by turbulence and surfaces in arbitrary motion," *Phil. Trans. R. Soc. Lond. A*, vol. 264, no. 1151, pp. 321–342, 1969.

N. H. Fletcher, "Air flow and sound generation in musical wind instruments," *Annual Review of Fluid Mechanics*, vol. 11, no. 1, pp. 123–146, 1979.

P. Freymuth, "On transition in a separated laminar boundary layer," *Journal of Fluid Mechanics*, vol. 25, no. 4, pp. 683–704, 1966.

N. Froessling, "Über die verdunstung fallender tropfen," *Gerlands Beiträge zur Geophysik*, vol. 52, pp. 170–215, 1938.

M. Gharib and A. Roshko, "The effect of flow oscillations on cavity drag," *Journal of Fluid Mechanics*, vol. 177, pp. 501–530, 1987.

M. Gharib, "Active control of flow induced resonance in continuous corrugated tubes," DTIC Document, Tech. Rep., 1993.

A. F. Ghoniem and K. K. Ng, "Numerical study of the dynamics of a forced shear layer," *The Physics of fluids*, vol. 30, no. 3, pp. 706–721, 1987.

E. R. Gilliland and T. K. Sherwood, "Diffusion of vapors into air streams," *Industrial & Engineering Chemistry*, vol. 26, no. 5, pp. 516–523, 1934.

X. Gloerfelt, "Cavity noise," in *von Karman Lect. Notes Aerodyn. Noise from Wall-Bounded Flows*, 2009.

A. Glover, S. Skippon, and R. Boyle, "Interferometric laser imaging for droplet sizing: a method for droplet-size measurement in sparse spray systems," *Applied Optics*, vol. 34, no. 36, pp. 8409–8421, 1995.

J. Golliard, S. Belfroid, and O. Vijlbrief, "Acoustic damping in smooth and corrugated pipes with and without liquid injection," in *ASME 2013 Pressure Vessels and Piping Conference*. American Society of Mechanical Engineers, 2013.

J. Golliard, N. González-Díez, S. Belfroid, G. Nakiboğlu, and A. Hirschberg, "U-rans model for the prediction of the acoustic sound power generated in a whistling corrugated pipe," in *ASME 2013 Pressure Vessels and Piping Conference*. American Society of Mechanical Engineers, 2013, pp. V004T04A040–V004T04A040.

R. C. Gonzalez and R. E. Woods, *Digital image processing*. Prentice Hall, 2012.

H. Goyder, "On the modelling of noise generation in corrugated pipes," *Journal of pressure vessel technology*, vol. 132, no. 4, 2010.

T. Häber, M. Gebretsadik, H. Bockhorn, and N. Zarzalis, "The effect of total reflection in plif imaging of annular thin films," *International Journal of Multiphase Flow*, vol. 76, pp. 64–72, 2015.

K. J. Hay, Z.-C. Liu, and T. J. Hanratty, "Relation of deposition to drop size when the rate law is nonlinear," *International journal of multiphase flow*, vol. 22, no. 5, pp. 829–848, 1996.

H. H. Heller and D. B. Bliss, "Flow-induced pressure fluctuations in cavities and concepts for their suppression," *Aeroacoustics: STOL Noise; Airframe and Airfoil Noise*, vol. 45, pp. 281–296, 1976.

G. F. Hewitt, "The breakdown of the liquid film in annular two-phase flow," *International Journal of Heat and Mass Transfer*, vol. 8, no. 5, pp. 781–791, 1965.

A. Hirschberg and S. W. Rienstra, *An introduction to aeroacoustics*. Eindhoven University of Technology, 2004.

M. S. Howe, "Edge, cavity and aperture tones at very low Mach numbers," *J. Fluid Mech.*, vol. 330, pp. 61–84, 1997.

M. S. Howe, *Theory of vortex sound*. Cambridge University Press, 2003.

M. Howe, "The influence of vortex shedding on the diffraction of sound by a perforated screen," *Journal of Fluid Mechanics*, vol. 97, no. 4, pp. 641–653, 1980.

U. Ingard and V. K. Singhal, "Effect of flow on the acoustic resonances of an open-ended duct," *The Journal of the Acoustical Society of America*, vol. 58, no. 4, pp. 788–793, 1975.

U. Ingard and V. K. Singhal, "Flow excitation and coupling of acoustic modes of a side-branch gravity in a duct," *The Journal of the Acoustical Society of America*, vol. 60, no. 5, pp. 1213–1215, 1976.

International Energy Agency, *Gas 2018, Analysis and forecasts to 2023*. OECD, 2018.

M. Ishii and M. A. Grolmes, "Inception criteria for droplet entrainment in two-phase concurrent film flow," *AIChE Journal*, vol. 21, no. 2, pp. 308–318, 1975.

M. Ishii and K. Mishima, "Droplet entrainment correlation in annular two-phase flow," *International Journal of Heat and Mass Transfer*, vol. 32, no. 10, pp. 1835–1846, 1989.

S.-H. Jang and J.-G. Ih, "On the multiple microphone method for measuring in-duct acoustic properties in the presence of mean flow," *The journal of the acoustical society of America*, vol. 103, no. 3, pp. 1520–1526, 1998.

S. W. Kieffer, "Sound speed in liquid-gas mixtures: Water-air and water-steam," *Journal of Geophysical research*, vol. 82, no. 20, pp. 2895–2904, 1977.

H. Y. Kim, S. Koyama, and W. Matsumoto, "Flow pattern and flow characteristics for counter-current two-phase flow in a vertical round tube with wire-coil inserts," *International Journal of Multiphase Flow*, vol. 27, no. 12, pp. 2063–2081, 2001.

V. Koschatzky, J. Westerweel, B. J. Boersma, F. Scarano, and P. D. Moore, "High speed PIV applied to aerodynamic noise investigation," *Experiments in Fluids*, vol. 50, no. 4, pp. 863–876, Jul. 2011.

R. T. Kukreja, S. C. Lau, and R. D. McMillin, "Local heat/mass transfer distribution in a square channel with full and v-shaped ribs," *International journal of heat and mass transfer*, vol. 36, no. 8, pp. 2013–2020, 1993.

R. Kumar, M. Gottmann, and K. R. Sridhar, "Film thickness and wave velocity measurements in a vertical duct," *Journal of fluids engineering*, vol. 124, no. 3, pp. 634–642, 2002.

H. J. Leutheusser, "Flow nozzles with zero beta ratio," *Journal of Basic Engineering*, vol. 86, no. 3, pp. 538–540, 1964.

H. Levine and J. Schwinger, "On the radiation of sound from an unflanged circular pipe," *Physical review*, vol. 73, no. 4, pp. 383–406, 1948.

D. R. Lide, *CRC Handbook of Chemistry and Physics*, 75th ed. CRC press, 1994.

M. J. Lighthill, "On sound generated aerodynamically i. general theory," in *Proceedings of the Royal Society of London A: Mathematical, Physical and Engineering Sciences*, vol. 211, no. 1107. The Royal Society, 1952, pp. 564–587.

A. Lyckegaard, J. Golliard, R. Hansen, E. Bendiksen, C. D. Cappeln, P. Hylland, K. Lunde, N. Sødahl, D. McGeorge, G. Skeie *et al.*, "A new flexible pipe for dynamic gas riser applications featuring flip resistant carcass," in *Offshore Technology Conference Asia*. Offshore Technology Conference, 2016.

O. Marsden, X. Gloerfelt, and C. Bailly, "Direct noise computation of adaptive control applied to a cavity flow," *Comptes Rendus Mecanique*, vol. 331, no. 6, pp. 423–429, 2003.

P. Martínez-Lera, C. Schram, S. Föller, R. Kaess, and W. Polifke, "Identification of the aeroacoustic response of a low mach number flow through a t-joint," *The Journal of the Acoustical Society of America*, vol. 126, no. 2, pp. 582–586, 2009.

A. Michalke, "On spatially growing disturbances in an inviscid shear layer," *Journal of Fluid Mechanics*, vol. 23, no. 3, pp. 521–544, 1965.

R. W. Miksad, "Experiments on nonlinear interactions in the transition of a free shear layer," *Journal of Fluid Mechanics*, vol. 59, no. 1, pp. 1–21, 1973.

R. M. Munt, "The interaction of sound with a subsonic jet issuing from a semi-infinite cylindrical pipe," *Journal of Fluid Mechanics*, vol. 83, no. 4, pp. 609–640, 1977.

R. M. Munt, "Acoustic transmission properties of a jet pipe with subsonic jet flow: I. the cold jet reflection coefficient," *Journal of Sound and Vibration*, vol. 142, no. 3, pp. 413–436, 1990.

G. Nakiboğlu and A. Hirschberg, "Aeroacoustic power generated by multiple compact axisymmetric cavities: Effect of hydrodynamic interference on the sound production," *Physics of fluids*, vol. 24, no. 6, p. 067101, 2012.

G. Nakiboğlu, S. Belfroid, J. Golliard, and A. Hirschberg, "On the whistling of corrugated pipes: effect of pipe length and flow profile," *Journal of Fluid Mechanics*, vol. 672, pp. 78–108, 2011.

G. Nakiboğlu, O. Rudenko, A. Hirschberg, J. Golliard, and S. P. C. Belfroid, "On the effect of a swirl on the self-sustained oscillations in compact axisymmetric cavities," in *Proc. 10th Int. Conf. Flow Induc. Vib. Flow Induc. Noise*, Dublin, Ireland, 2012, pp. 49–53.

G. Nakiboğlu, H. Manders, and A. Hirschberg, "Aeroacoustic power generated by a compact axisymmetric cavity: prediction of self-sustained oscillation and influence of the depth," *Journal of fluid mechanics*, vol. 703, pp. 163–191, 2012a.

G. Nakiboğlu, S. P. C. Belfroid, J. F. H. Willems, and A. Hirschberg, "Whistling behavior of periodic systems: Corrugated pipes and multiple side branch system," *Int. J. Mech. Sci.*, vol. 52, no. 11, pp. 1458–1470, Nov. 2010.

G. Nakiboğlu, O. Rudenko, and A. Hirschberg, "Aeroacoustics of the swinging corrugated tube: voice of the dragon," *The Journal of the Acoustical Society of America*, vol. 131, no. 1, pp. 749–765, 2012b.

P. Nelson, N. Halliwell, and P. Doak, "Fluid dynamics of a flow excited resonance, part ii: Flow acoustic interaction," *Journal of sound and vibration*, vol. 91, no. 3, pp. 375–402, 1983.

A. N. Norris and I. C. Sheng, "Acoustic radiation from a circular pipe with an infinite flange," *Journal of Sound and Vibration*, vol. 135, no. 1, pp. 85–93, 1989.

L. Pan and T. J. Hanratty, "Correlation of entrainment for annular flow in vertical pipes," *International Journal of Multiphase Flow*, vol. 28, no. 3, pp. 363–384, 2002.

L. Peerlings, "Methods and techniques for precise and accurate in-duct aero-acoustic measurements: Application to the area expansion," Ph.D. dissertation, KTH Royal Institute of Technology, 2015.

S. W. Perng and D. S. Dolling, "Suppression of pressure oscillations in high-mach-number, turbulent, cavity flow," *Journal of Aircraft*, vol. 38, no. 2, pp. 248–256, 2001.

M. C. A. M. Peters, A. Hirschberg, A. J. Reijnen, and A. P. J. Wijnands, "Damping and reflection coefficient measurements for an open pipe at low mach and low helmholtz numbers," *Journal of Fluid Mechanics*, vol. 256, pp. 499–534, 1993.

M. C. A. M. Peters, "Aeroacoustic sources in internal flows," Ph.D. dissertation, Eindhoven University of Technology, 1993.

A. Petrie and I. Huntley, "The acoustic output produced by a steady airflow through a corrugated duct," *Journal of Sound and Vibration*, vol. 70, no. 1, pp. 1–9, 1980.

M. Popescu and S. T. Johansen, "Acoustic wave propagation in low mach flow pipe," in *46th AIAA Aerospace Sciences Meeting and Exhibit*, 2008, p. 63.

A. Powell, "Theory of vortex sound," *The journal of the acoustical society of America*, vol. 36, no. 1, pp. 177–195, 1964.

B. Rajavel and M. Prasad, "Acoustics of corrugated pipes: a review," *Applied Mechanics Reviews*, vol. 65, no. 5, 2013.

L. Rayleigh, "On the stability, or instability, of certain fluid motions," *Proc. London Math. Soc.*, vol. 9, pp. 57–70, 1880.

L. Rayleigh, "Xlviii. æolian tones," *The London, Edinburgh, and Dublin Philosophical Magazine and Journal of Science*, vol. 29, no. 172, pp. 433–444, 1915.

S. W. Rienstra, *Fundamentals of duct acoustics*. Eindhoven University of Technology, 2015.

D. Rockwell and E. Naudascher, "Self-sustaining oscillations of flow past cavities," *Journal of Fluids Engineering*, vol. 100, no. 2, pp. 152–165, 1978.

D. Rockwell and E. Naudascher, "Self-sustained oscillations of impinging free shear layers," *Annual Review of Fluid Mechanics*, vol. 11, no. 1, pp. 67–94, 1979.

D. Rockwell and A. Schachenmann, "Self-generation of organized waves in an impinging turbulent jet at low mach number," *Journal of Fluid Mechanics*, vol. 117, pp. 425–441, 1982.

D. Ronneberger and C. Ahrens, "Wall shear stress caused by small amplitude perturbations of turbulent boundary-layer flow: an experimental investigation," *Journal of Fluid Mechanics*, vol. 83, no. 03, pp. 433–464, 1977.

C. W. Rowley and D. R. Williams, "Dynamics and control of high-reynolds-number flow over open cavities," *Annu. Rev. Fluid Mech.*, vol. 38, pp. 251–276, 2006.

O. Rudenko, G. Nakiboğlu, A. Holten, and A. Hirschberg, "On whistling of pipes with a corrugated segment: Experiment and theory," *Journal of Sound and Vibration*, vol. 332, no. 26, pp. 7226–7242, 2013.

D. A. Russell, J. P. Titlow, and Y.-J. Bemmen, "Acoustic monopoles, dipoles, and quadrupoles: An experiment revisited," *American Journal of Physics*, vol. 67, no. 8, pp. 660–664, 1999.

F. Sanna, J. Golliard, and S. Belfroid, "On the effect of water film on flow-induced pulsations in closed side branches in tandem configuration," in *ASME 2015 Pressure Vessels and Piping Conference*. American Society of Mechanical Engineers, 2015.

R. Sarno and M. Franke, "Suppression of flow-induced pressure oscillations in cavities," *Journal of Aircraft*, vol. 31, no. 1, pp. 90–96, 1994.

V. Sarohia, "Experimental and analytical investigation of oscillations in flows over cavities," Ph.D. dissertation, California Institute of Technology, 1975.

P. Sawant, M. Ishii, T. Hazuku, T. Takamasa, and M. Mori, "Properties of disturbance waves in vertical annular two-phase flow," *Nuclear Engineering and Design*, vol. 238, no. 12, pp. 3528–3541, 2008.

P. Sawant, M. Ishii, and M. Mori, "Prediction of amount of entrained droplets in vertical annular two-phase flow," *International Journal of Heat and Fluid Flow*, vol. 30, no. 4, pp. 715–728, 2009.

R. F. Schmit and G. Raman, "High and low frequency actuation comparison for a weapons bay cavity," *International Journal of Aeroacoustics*, vol. 5, no. 4, pp. 395–414, 2006.

D. Schubring, A. C. Ashwood, T. A. Shedd, and E. T. Hurlburt, "Planar laser-induced fluorescence (PLIF) measurements of liquid film thickness in annular flow. Part I: Methods and data," *International Journal of Multiphase Flow*, vol. 36, no. 10, pp. 815–824, 2010.

Y. Taitel, D. Bornea, and A. Dukler, "Modelling flow pattern transitions for steady upward gas-liquid flow in vertical tubes," *AIChE Journal*, vol. 26, no. 3, pp. 345–354, 1980.

D. Tonon, B. J. T. Landry, S. P. C. Belfroid, J. F. H. Willems, G. C. J. Hofmans, and A. Hirschberg, "Whistling of a pipe system with multiple side branches: Comparison with corrugated pipes," *Journal of Sound and Vibration*, vol. 329, no. 8, pp. 1007–1024, 2010.

R. G. Turner, M. G. Hubbard, and A. E. Dukler, "Analysis and prediction of minimum flow rate for the continuous removal of liquids from gas wells," *Journal of Petroleum Technology*, vol. 21, no. 11, pp. 1–475, 1969.

L. S. Ukeiley, M. K. Ponton, J. M. Seiner, and B. Jansen, "Suppression of pressure loads in cavity flows," *AIAA journal*, vol. 42, no. 1, pp. 70–79, 2004.

A. C. van Eckeveld, J. Westerweel, and C. Poelma, "Mitigation of whistling in vertical corrugated pipes by liquid addition," *Experiments in Fluids*, vol. 58, no. 9, p. 107, 2017.

A. C. van Eckeveld, E. Gotfredsen, J. Westerweel, and C. Poelma, "Annular two-phase flow in vertical smooth and corrugated pipes," *International Journal of Multiphase Flow*, vol. 109, pp. 150–163, 2018.

J. M. C. van 't Westende, H. K. Kemp, R. J. Belt, L. M. Portela, R. F. Mudde, and R. V. A. Oliemans, "On the role of droplets in cocurrent annular and churn-annular pipe flow," *International journal of multiphase flow*, vol. 33, no. 6, pp. 595–615, 2007.

G. B. Wallis, "Phenomena of liquid transfer in two-phase dispersed annular flow," *International Journal of Heat and Mass Transfer*, vol. 11, no. 4, pp. 783–785, 1968.

C. Weng, "Theoretical and numerical studies of sound propagation in low-mach-number duct flows," Ph.D. dissertation, KTH Royal Institute of Technology, 2015.

F. M. White, "Fluid mechanics fourth edition," 2017.

G. Zabaras, A. E. Dukler, and D. Moalem-Maron, "Vertical upward cocurrent gas-liquid annular flow," *AIChE journal*, vol. 32, no. 5, pp. 829–843, 1986.

J. Zhou, R. J. Adrian, S. Balachandar, and T. M. Kendall, "Mechanisms for generating coherent packets of hairpin vortices in channel flow," *Journal of Fluid Mechanics*, vol. 387, pp. 353–396, 1999.

S. Ziada and E. Bühlmann, "Flow induced vibration in long corrugated pipes," in *Proceedings of the International Conference on Flow Induced Vibrations*, 1991.

ACKNOWLEDGEMENTS

Many people have contributed in different ways to the work presented in this thesis. Without their support and contribution to this work, it would have been impossible to complete the booklet in your hands. I want to express my gratitude to all of them.

First of all I would like to thank my daily supervisor Christian Poelma who, over the course of this PhD project changed from co-promotor to promotor of my work. Your very broad experimental expertise, combined with a broad knowledge of multiphase fluid dynamics guided me through the process. I also appreciate the freedom you gave me to complete this work the way I thought was best. You even allowed me to leave the lab and my PhD for half a year, just after starting, which I think is quite extraordinary.

I also want to express my gratitude to my second promotor, Jerry Westerweel, for giving me the opportunity to do my PhD research in the well-equipped Aero- & Hydro Lab. If one thing is sure, it is that our many meetings always provided me with a wide variety of new possibilities and ideas, of which many were never seriously assessed, I'm afraid.

I am very thankful to Shell, for providing funds for the research project and for the very practical applications that this work contributes to. I very much needed this applied side of the research to keep me motivated throughout the past years. Especially Peter Veenstra and Dick ten Bosch proved to be not only valuable in funding this work, but also great sparring partners throughout the process. Even moving to India didn't stop Dick from being involved in this project.

Since the field of aeroacoustics was largely new to me at the start of this journey in 2013, the discussions I had with Mico Hirschberg have surely pushed the level of this thesis. Several times I took the train to Eindhoven, or he took the train to Delft, to discuss the contents of this work, as well as some other aspects of life. I very much appreciated not only your knowledge and experience in the field, but also your positive and friendly attitude. You were by far the fastest of anyone involved in this project in replying to my many e-mails with questions and comments.

Also the discussions with Stefan Belfroid (TNO) and Joachim Golliard (CTTM, former TNO) on various aspects of this work, especially the practical difficulties involved in performing acoustic measurements helped me a lot.

Thank you Erik Gotfredsen (DTU) for helping me out with part of the experiments reported in Chapter 3 of this thesis, and for showing us around in Kopenhagen.

Maybe the most important people when it comes to the experimental work were Jan, Edwin and Jasper. Finding and eliminating electrical noise in the experimental signals (Jan), setting up the camera system with optics and troubleshooting LaVision (Edwin) and essentially building the experimental setup and manufacturing countless numbers of other objects (Jasper) proved to be crucial in obtaining proper measurement results.

As being a PhD candidate involves spending many (sometimes boring) hours alone behind your PC or in the lab, it is surely crucial to spend those hours surrounded by a very diverse palette of truly awesome colleagues. Thank you Jerke, Greta, Henk, Ankur, Sedat,

Pepijn, Mike, Melika, Arati, Daniele, Maurice, Tariq, Özge, Arnoud, Pedro, Ernst Jan, Mark, Gerrit, Mathieu, René Delfos, Caroline, Marieke, Manu, Florian, Jasper Tomas, Sita, Koen, Guillermo, John, Dries, Parviz, Daniel, Wim-Paul, Ruud, Ema, Wout, Willian, Saad, Amitosh, Sören, Gem, Göktürk, Aris, René van Hout, Jasper Ruijgrok, Edwin and Jan. During my PhD I had the privilege to share the office with Daniele, Maurice, Özge, Tariq and Melika, which was a great deal of fun. Especially the Friday afternoon gatherings in our office are memorable. Special thanks to the *GoT* group for the many (extended) lunch breaks and lots of everyday amusement in the lab. Many thanks also to Flo, for the countless hours spend together at the cavitation tunnel. My (noisy) experiments made your life difficult there, but you never complained about wearing those beautiful earmuffs (again), and listening to Dutch radio. I also want to thank the (Bsc. and Msc.) graduate students that I supervised during my PhD; especially Avinash, Mike (ending up as a colleague), Ankit and Boy. Thanks for the numerous discussions that we had. I hope you enjoyed it as much as I did.

I am very thankful to the many friends and family that have supported me the past years. Bedankt pap en mam voor het altijd achter me staan, welke keuzes ik ook maak. Jullie vertrouwen in mij en de zelfstandigheid die ik altijd heb meegekregen hebben me erg geholpen tijdens mijn promotie, en ik prijs me gelukkig met ouders zoals jullie.

Annet, ik ben bang dat ik niet sentimenteel genoeg ben om hier te schrijven dat ik deze promotie zonder jou niet had kunnen afronden. Zonder jou was het wellicht zelfs sneller gegaan. Echter, zonder jou was het vooral aanzienlijk minder leuk geweest. Dank je voor de schwung die je aan mijn leven geeft, dat maakt het de moeite waard. Wanneer gaan we weer kamperen? En hoewel hij nog vrij weinig heeft bijgedragen aan dit boekje, kan ik niet afsluiten zonder Mathies te noemen. Het puntje op de i van een proefschrift zet je toch een stuk makkelijker met een knorrend babylachje op de achtergrond.

Andries van Eckeveld
Delft, May 2019

LIST OF PUBLICATIONS

JOURNAL PUBLICATIONS

A. C. van Eckeveld, L. V. van der Ham, L. F. G. Geers, L. J. P. van den Broeke, B. J. Boersma, and E. L. V. Goetheer, "Online monitoring of the solvent and absorbed acid gas concentration in a CO_2 capture process using monoethanolamine," *Industrial & Engineering Chemistry Research*, vol. 53, no. 13, pp. 5515–5523, 2014.

L. V. van der Ham, A. C. van Eckeveld, and E. L. V. Goetheer, "Online monitoring of dissolved CO_2 and MEA concentrations: effect of solvent degradation on predictive accuracy," *Energy Procedia*, vol. 63, pp. 1223–1228, 2014.

A. C. van Eckeveld, J. Westerweel, and C. Poelma, "Mitigation of whistling in vertical corrugated pipes by liquid addition," *Experiments in Fluids*, vol. 58, no. 9, p. 107, 2017.

A. C. van Eckeveld, E. Gotfredsen, J. Westerweel, and C. Poelma, "Annular two-phase flow in vertical smooth and corrugated pipes," *International Journal of Multiphase Flow*, vol. 109, pp. 150–163, 2018.

A. C. van Eckeveld, J. Westerweel, and C. Poelma, "Silencing corrugated pipes with liquid addition - identification of the mechanisms behind whistling mitigation," (*submitted to Journal of Sound and Vibration*).

CONFERENCE PUBLICATIONS AND CONTRIBUTIONS

L. V. van der Ham, A. C. van Eckeveld, A. Benamor, and E. L. V. Goetheer, "Real-time monitoring of solvent composition for acid gas absorption processes," in *Proceedings of the 4th international gas processing symposium, Doha, Qatar*, 2014.

A. C. van Eckeveld, A. K. Pancham, J. Westerweel, and C. Poelma, "Flow over partially liquid filled cavity," in *15th European Turbulence Conference, Delft, The Netherlands*, 2015.

A. C. van Eckeveld, J. Westerweel, and C. Poelma, "Attenuation of whistling in vertical corrugated pipes by liquid addition," in *11th Int. Conference on Flow-Induced Vibration, Den Haag, The Netherlands*, 2016.

A. C. van Eckeveld, J. Westerweel, and C. Poelma, "Attenuation of whistling in vertical corrugated pipes by liquid addition," in *Burgers Symposium, Lunteren, The Netherlands*, 2016.

A. C. van Eckeveld, J. Westerweel, and C. Poelma, "The effect of liquid filling on shear layer behavior over a rectangular cavity," in *European Fluid Mechanics Conference, Seville, Spain*, 2016.

A. C. van Eckeveld, J. Westerweel, and C. Poelma, "Whistling in corrugated pipes, subject to two-phase flow," in *Physics at FOM, Veldhoven, The Netherlands*, 2017.

A. C. van Eckeveld, J. Westerweel, and C. Poelma, "Flow-induced noise in corrugated pipes - why does liquid reduce whistling?" in *23rd AIAA/CEAS Aeroacoustics Conference, Denver, USA*, 2017.